INFORMATION TO USERS

This manuscript has been reproduced from the microfilm master. UMI films the text directly from the original or copy submitted. Thus, some thesis and dissertation copies are in typewriter face, while others may be from any type of computer printer.

The quality of this reproduction is dependent upon the quality of the copy submitted. Broken or indistinct print, colored or poor quality illustrations and photographs, print bleedthrough, substandard margins, and improper alignment can adversely affect reproduction.

In the unlikely event that the author did not send UMI a complete manuscript and there are missing pages, these will be noted. Also, if unauthorized copyright material had to be removed, a note will indicate the deletion.

Oversize materials (e.g., maps, drawings, charts) are reproduced by sectioning the original, beginning at the upper left-hand corner and continuing from left to right in equal sections with small overlaps. Each original is also photographed in one exposure and is included in reduced form at the back of the book.

Photographs included in the original manuscript have been reproduced xerographically in this copy. Higher quality 6" x 9" black and white photographic prints are available for any photographs or illustrations appearing in this copy for an additional charge. Contact UMI directly to order.

UMI

A Bell & Howell Information Company
300 North Zeeb Road, Ann Arbor MI 48106-1346 USA
313/761-4700 800/521-0600

Geometry Effect on Post-Dryout Heat Transfer

by

Ji Zhang

A dissertation submitted to the School of Graduate Studies and Research of the Ottawa-Carleton Institute for Mechanical and Aeronautical Engineering at the University of Ottawa in partial fulfilment of the requirements for the degree of Master of Applied Science in Mechanical Engineering

Ottawa-Carleton Institute for Mechanical and Aeronautical Engineering
University of Ottawa, Ottawa, Ontario, Canada K1N 6N5
December, 1997

National Library
of Canada

Acquisitions and
Bibliographic Services

395 Wellington Street
Ottawa ON K1A 0N4
Canada

Bibliothèque nationale
du Canada

Acquisitions et
services bibliographiques

395, rue Wellington
Ottawa ON K1A 0N4
Canada

Your file Votre référence

Our file Notre référence

0-612-28469-7

Canada

ABSTRACT

A thorough literature review of the effects of channel shape and spacing devices on post-dryout heat transfer has been performed. Overall, very few information are available for these effects, several experiments were carried out covering only limited flow conditions and geometries. To extend the present review, studies with air flow through heated channels have also been included.

The effect of channel shape is small for channels with rounded corners, but is rather significant for those with sharp corners (especially those of small apex angle). As a result, the heat transfer rate is much lower in a triangular than a rectangular channel at the same flow conditions (the heat transfer rate in tubes is often the highest). In addition, the circumferential heat flux distribution affects the overall heat transfer rate considerably (e.g., comparing triangular channels with either one-side or all-side heated).

A strong effect of spacing devices on heat transfer has been observed in both single-phase and post-dryout studies. It enhances significantly the heat transfer rate at locations downstream of the spacer. Most studies showed an exponentially decaying trend of heat transfer enhancement with increasing distance away from the spacer. Correlations have been proposed to represent this trend, they can only be applied to specific range of flow conditions due to the limited database.

In view of the deficiency among existing prediction methods, correlations for the effects of channel shape and spacing devices on post-dryout heat transfer have been developed to improve the prediction accuracy and range of applications. These correlations provide good agreement with experimental data obtained in other studies. Furthermore, they exhibit correct asymptotic and parametric trends and hence can be extrapolated to conditions beyond the present database. However, it is difficult to quantify the uncertainty of the extrapolation due to a lack of data.

Geometry Effect on Post-Dryout Heat Transfer

Dr. S. C. Cheng, Supervisor

Ji Zhang, Candidate

VALUE AND IMPACT OF THIS STUDY

An accurate prediction of post-dryout heat transfer rate is important for containing potential damages to heat transfer equipment under postulated accident conditions. In particular, it has a significant impact on the safe operation of heat-generating systems (such as the primary cooling loop of a nuclear reactor). Although a large amount of information is available for post-dryout heat transfer in tubes, this study has shown that tube-based information may not be appropriate for some analyses and other effects on post-dryout heat transfer have to be considered and included. The proposed correlations were developed with the goals of improving the prediction accuracy and widening the applications. The conclusions of this study have clearly shown that these goals have been achieved.

The findings of the literature review showed the deficiency of present state-of-the-art information on post-dryout heat transfer. They can assist in defining future direction of experimental and analytical studies to improve the understanding of the phenomena. The proposed correlations extend the tube-based correlations to other channel shape and spacing devices. This can improve the prediction accuracy and reduce the uncertainty of flow-boiling analysis.

ACKNOWLEDGEMENTS

I would like to give my sincere thank to my supervisor, Dr. S. C. Cheng, for his support, encouragement and discussion during my study at University of Ottawa.

I am very grateful to Dr. D. C. Groeneveld of AECL, for his helpful guidance and suggestion throughout this study.

I also deeply thank to Dr. L. K. H. Leung of AECL, without his patient step by step guidance and cheerful encouragement, this thesis would never complete.

I also thank everyone who has ever helped me during my study and work on my thesis.

TABLE OF CONTENTS

LIST OF TABLES

LIST OF FIGURES

NOMENCLATURE

Symbol	Definition	Unit
a_I	experiment determined constant	-
A	geometry-dependent correlating constants	-
A_f	flow channel cross-section area	m^2
A_{ob}	obstcale cross-section area	m^2
b_I	experiment determined constant	-
B	geometry-dependent correlating constants	-
C	desuperheating factor	-
Cp	specific heat under constant pressure	KJ/kgK
D	diameter	m
e	absolute eccentricity	m
G	mass flux	kg/m^{2}s
h	heat transfer coefficient	W/m^{2}K
h_{bundle}	heat transfer coefficient in bundle	W/m^{2}K
$\bar{h}_{des}$	heat transfer coefficient for design geometry	W/m^{2}K
h_{tube}	heat transfer coefficient in tube	W/m^{2}K
H	enthalpy	KJ/kg
H_{fg}	latent heat of vaporization	KJ/kg
I	bundle distortion factor defined in eq. (3-1)	-
J	minimum-gap factor defined in eq. (3-2)	-
k	thermal conductivity	W/mK
K_{AFD}	axial heat flux distribution factor	-
$K_{channel}$	channel effect factor defined in eq. (4-3)	-
$K_{dev.}$	flow development factor	-
K_e	heat transfer enhancement factor defined in eq. (3-6)	-
K_{gap}	gap effect factor defined in eq. (4-2)	-

K_{ob}	single-phase loss coefficient	-
K_{shape}	cross-section shape factor	-
K_{spacer}	modification factor of spacer effect	-
L_1	minimum distance from the centroid to any side	m
L_2	maximum distance from the centroid to any side	m
L_3	maximum distance from the centroid to any apex	m
L_H	heated length	m
Ls	distance between two spacers	m
n	droplet number density	-
N	total number of experiment data	-
Nu	Nusselt number = hD/k	-
$Nu_{non\text{-}tube}$	Nusselt number of non-tube	-
$Nu_{no\ spacer}$	Nusselt number with no spacer	-
Nu_{spacer}	Nusselt number with spacer	-
Nu_{tube}	Nusselt number of tube	-
Nu^*	Nusselt number ratio = Nu/Nu_0	-
P	pitch	m
P	pressure	MPa
q	heat flux	W/m^2
r	radius	-
Re	Reynolds number = GD/μ	-
S	heat sink= $n\pi D^2 h r_i^2 / k_g$	-
S_0	nominal gap between rods	m
S/S_0	dimensionless gap width	-
t	grid spacer height	m
T	temperature	°C
U	velocity	m/s
w	grid spacer width	m
W	width	m
W	mass flow rate	kg/s

We	Weber number = $\rho U^2 D / \sigma$	-
x	quality	-
x_{thr}	flow dependent function defined in eq. (3-7)	-
Z	axial distance downstream of the spacer	m

Greek	Definition	Unit
α	aspect ratio = height/width	-
δ	rod-wall gap width, gap width	m
ε	eccentricity ratio = $e/(r_0 - r_i)$	-
ϵ	blockage-area ratio = A_{ob}/A_f	-
γ	radius ratio = r_0/r_i	-
μ	viscosity	kg/ms
Φ	peripheral coordinate	-
ψ	function defined in eq. (3-8)	-
ρ	density	kg/m^3
σ	surface tension	N/m

Subscript	Definition
0	no blockage
CHF	critical heat flux
dev	developing-flow
do	dryout
D	droplet, diameter
e	equilibrium condition
f	liquid phase
g	vapor phase
he	heated
hy	hydraulic

i	inner
in	inlet condition
min	minimum
o	outer
pre	pre-dryout
pdo	post-dryout
sat	saturated condition
sp	spacer
th	thermodynamic
va	actual vapor value
ve	equilibrium vapor value
w	wall

Abbreviation	Definition
AECL	Atomic Energy of Canada Limited
CANDU	CANada Deuterium Uranium, a registered trademark
CHF	Critical Heat Flux
DFFB	Dispersed Flow Film Boiling
DNB	Departure from Nucleat Boiling
IAFB	Incerted Annular Film Boiling
ID	inner diameter
LOCA	Loss of Coolant Accident
MFB	Minimum Film-Boiling
OD	outer diameter
PDO	Post-Dryout
RMS	Root-Mean-Square
UO	University of Ottawa

1. INTRODUCTION

Post-dryout heat transfer is encountered at conditions where critical heat flux (CHF) or CHF temperature has been exceeded, and includes heat transfer modes of both transition boiling and film boiling. Since transition boiling is encountered only in a temperature-controlled system, post-dryout heat transfer often refers loosely to film boiling in a heat-flux-controlled system. The present study focuses mainly on the heat-flux-controlled system.

Post-dryout conditions can occur in many applications (e.g., steam generators, nuclear reactors, metallurgical processing and cryogenic systems). In most cases, the flow passes through a bundle of rods and extracts heat from the outside surface of the rods. Spacing devices have been installed to maintain the gap size between rods and reduce vibration. At post-dryout conditions, heat on the surface is primarily transferred by convection to vapor, which has a low thermal conductivity and capacity. This often results in a sharp temperature rise that can cause damage to the heat transfer surface. At some situations, the equipment failure may lead to severe consequence and endanger environment and life. Therefore, it is crucial to predict accurately the surface temperature at the post-dryout conditions to prevent any occurrence of accidents.

There are generally two types of heat transfer analysis: cross-sectional average analysis based on average flow conditions over the bundle and subchannel analysis based on local flow conditions in various subchannels. Both analyses employ tube-based prediction methods for post-dryout heat transfer, which were extended to bundle geometry using the hydraulic-equivalent diameter approach. Although this approach was shown valid for geometries of channel shape close to a tube, it does not provide a good estimation of heat transfer in other geometries (e.g., triangular shape or channels with narrow gaps). Figure 1.1 illustrates schematically the subdivision of a bundle into various subchannels. The cross-sectional flow area of the subchannels is often characterized as either square or triangular shape. Therefore, the effect of cross-sectional channel shape must be included to improve the prediction accuracy of post-dryout heat transfer.

The effect of spacing devices on post-dryout heat transfer is often ignored in the analysis because (i) there is no appropriate prediction method for this effect (the available methodologies are valid mainly for single-phase flow) and (ii) ignoring the effect provides generally a conservative prediction of surface temperature. This results in an unrealistic prediction of surface temperature and penalizes the efficiency of the heat transfer equipment. Therefore, the effect of spacing devices must be included in the analysis to improve the prediction accuracy of post-dryout heat transfer.

The objective of this study is to develop generalized methodologies for predicting the effects of cross-sectional flow-area shape and spacing devices on post-dryout heat transfer. To achieve this goal, a thorough literature review on these effects has been carried out. It provides the up-to-date information on experimental and analytical studies and shows the deficiency of existing prediction methods. New methodologies for these effects have been developed to improve the prediction accuracy using the available experimental data. An experiment has been completed to obtain data to validate the prediction method for the effect of spacing device on post-dryout heat transfer.

The following chapters document the findings of this study. Chapter 2 describes the mechanisms of various flow-boiling regimes focussing on those of the film boiling. The literature review of the effects of cross-sectional channel shape, spacing devices and gap size on single-phase and post-dryout heat transfer is presented in Chapter 3. Chapter 4 describes the development process of two correlations for predicting the effects of channel shape and spacing device on post-dryout heat transfer. Chapter 5 describes the experiment performed at the University of Ottawa to obtain post-dryout heat transfer data in a channel with three different types of flow obstruction. The analysis of the experimental data and the validation of the correlation for the effect of spacing device are presented in Chapter 6. Chapter 7 provides the conclusions of this study and a few recommendations for future work.

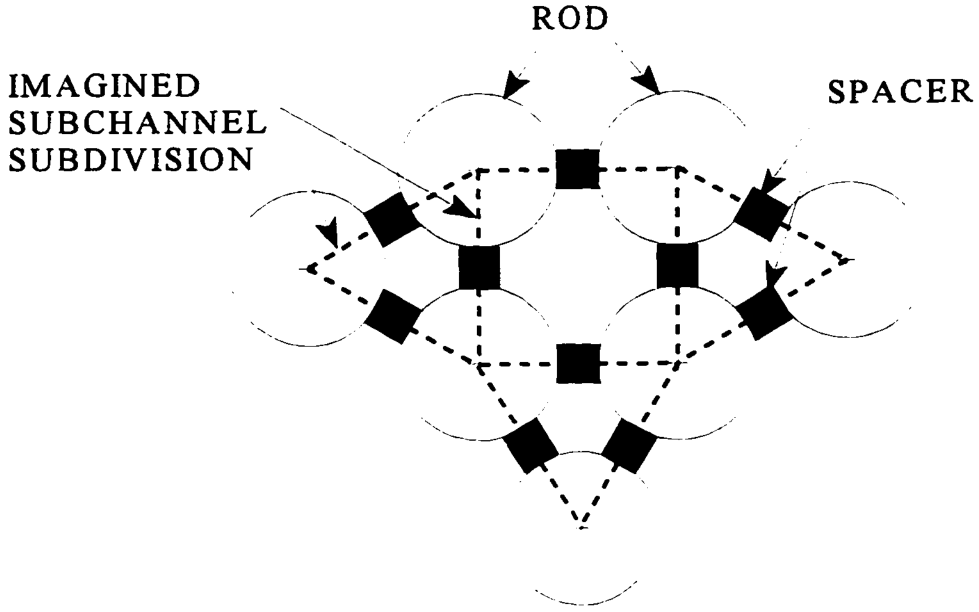

SECTION OF A ROD BUNDLE

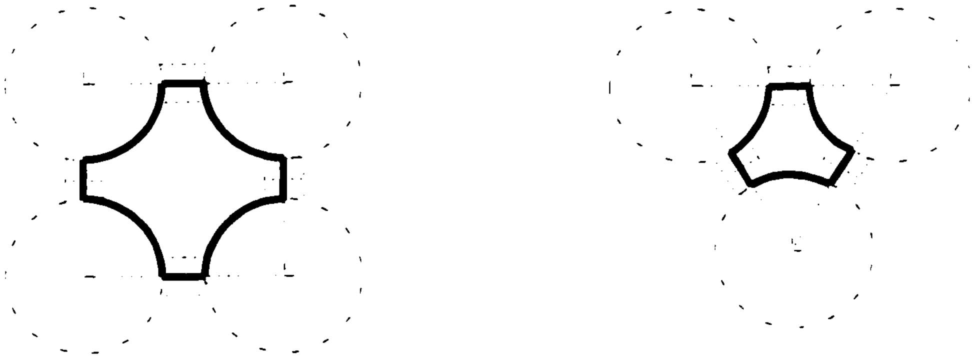

SIMULATED SQUARE SUBCHANNEL

SIMULATED TRIANGULAR SUBCHANNEL

Figure 1.1. Subchannel subdivision and shapes in a rod bundle

2. FLOW-BOILING MECHANISMS

Flow boiling refers to heat transfer modes where evaporation takes place in the process. This includes nucleate boiling, transition boiling and film boiling, and excludes the single-phase heat transfer to either liquid and vapor. A boiling curve provides the simplest way to illustrate the relation between various heat transfer modes. Figure 2.1 shows schematically the boiling curve for flow boiling. The transition between nucleate boiling and transition boiling is often referred to as the critical heat flux (CHF) or dryout point. It has been widely studied because the CHF point separates the low- and high-temperature regions and is often used as the criteria for determining the operating power of heat transfer equipment. Conditions encountered before the CHF point are referred to as the pre-dryout conditions and those after the CHF point are the post-dryout conditions. The transition between transition boiling and film boiling is referred to as the minimum film-boiling (MFB) point. It has not been examined extensively, as compared to the CHF point, because the MFB point is relatively unstable and experimental data are difficult to obtain.

The shape of the boiling curve varies with flow conditions (i.e., pressure, mass flux and quality) and heating characteristics (i.e., surface-temperature controlled or heat-flux controlled systems). Figure 2.2 illustrates the variation of boiling curve with increasing qualities (Groeneveld et al. 1989). The variation of heat transfer modes of a temperature-controlled system is shown in a dashed line of the boiling curve in Figure 2.1, while that of a heat-flux controlled system is shown in a solid line. It can be observed that transition boiling is not encountered in the heat-flux controlled system, and post-dryout heat transfer often refers to film boiling in the channel.

2.1 Heat Transfer in Tubes

The heat transfer mode varies along a heated tube in flow boiling; the variation depends strongly on the flow conditions. Figure 2.3 illustrates schematically the variations for low-quality and high-quality conditions.

With a subcooled liquid flow at the inlet end, bubbles initiate at the onset of nucleate boiling. Nucleate boiling is observed at the region between the onset of nucleate boiling and the saturation point. At locations beyond the saturation point, a transition to forced-convective evaporation is observed for high-quality conditions while the nucleate boiling is maintained for low-quality conditions. With further increases of flow quality, the point of critical heat flux is encountered. Downstream of this point, film boiling is encountered and the heated surface is cooled by the vapor flow.

Different mechanisms are observed at the point of critical heat flux depending on the flow quality, and lead to different film-boiling modes. At high-quality conditions (with void fractions higher than ~80%), the vapor is mixed with a high concentration of liquid droplets and is referred to as the dispersed-flow film boiling (DFFB). The amount of droplets depletes with increasing quality and the flow becomes a single-phase vapor at the downstream end of the channel. At low-quality conditions (with void fractions lower than ~50%), a thin vapor film is formed between the heated surface and the liquid core, and is often referred to as the inverted annular-flow film boiling (IAFB). With increasing quality, the liquid core breaks up and a dispersed flow is encountered (DFFB). As described above, a transition from DFFB to single-phase vapor flow occurs at high quality.

The present study focuses mainly on DFFB which is encountered more often than IAFB in flow-boiling equipment. IAFB relates to the rewetting process of the nuclear fuel elements after the injection of emergency core coolant in a postulated accident. Detailed discussions on other heat transfer modes and transition points have been presented by Collier (1981), Hsu (1982), Hewitt (1982), etc.

2.2 Film Boiling

Film boiling refers to the heat transfer mode where the vapor phase is in contact with the heated surface. Heat is transferred from the surface by (i) conduction through the vapor, (ii) convection by the vapor, (iii) radiation to the vapor, (iv) radiation to the liquid droplets, (v) convection from the surface to the droplet (through vaporization), and (vi) direct contact with impinged droplets. Depending on the flow conditions, some of these processes may not be dominant and can be neglected. Nevertheless, film-boiling heat transfer is complicated and still has not been clearly understood. This is primarily caused by the high surface temperature associated with this heat transfer mode making it difficult to obtain experimental data for most thermalhydraulic parameters (e.g., actual vapor temperature, droplet sizes and distributions, etc.).

2.2.1 Experimental Studies on Film Boiling

A large number of experiments were performed to study film boiling; the majority of them used tubes as the test section and focused mainly on the upward flow of water. Bennett et al. (1967) and Becker et al. (1983) obtained data at DFFB conditions, while Stewart (1981) and Laperrière (1983) measured the temperatures at IAFB conditions. Despite of the vast amount of data, only a limited range of flow conditions have previously been covered (Leung et al., 1997). Furthermore, a large scatter was observed among data of various studies even at similar flow conditions. This results in a much higher uncertainty in both the database and the prediction methods.

Figure 2.4 shows the surface-temperature distributions along the test section obtained at DFFB conditions (Bennett et al. 1967). At the inlet end, the surface-temperature measurements are generally low. This region corresponds to the pre-dryout conditions (either nucleate boiling or forced convective evaporation) with the surface temperatures slightly higher than the saturation values. A sharp rise of surface temperature is observed at the dryout point, where the transition from pre-dryout to PDO (film boiling) conditions occurs. Beyond this point, the surface temperature decreases with axial distance (or quality). This is caused by the increase in vapor velocity, which leads to an increase in convective heat transfer rate.

The surface-temperature data of Becker et al. (1983) is shown in figure 2.5. Similar to the data of

Bennett et al. (1967), both the pre-dryout and PDO regions are clearly shown and the surface temperature increases at the dryout point. However, unlike the trend in Figure 2.4, the temperature rise is less rapid in the data of Becker et al. (1983) than those of Bennett et al. (1967). The relatively smooth temperature rise is caused by an increase in heat transfer rate due to the droplet impingement to the surface. This is referred to as the developing flow effect and is observed mainly at the mid-quality conditions. Once the flow becomes fully developed, the decreasing surface-temperature trend with increasing axial distance is also shown.

The present study focuses mainly on the effects of channel shape (other than tubes) and spacing devices on PDO heat transfer. Therefore, a detailed review of the present state-of-the-art in experimental study of PDO heat transfer in tubes is beyond the scope of this work.

2.2.2 Prediction Methods for Film-Boiling Heat Transfer

Prediction methods for film-boiling heat transfer can be subdivided into three categories: correlations, phenomenological models, and semi-analytical models. Theoretical models are valid only for limited flow conditions (e.g., laminar flow) and hence are not included. Several reviews of the state-of-the-art in prediction methods for PDO heat transfer were presented by Groeneveld (1982) for DFFB, Groeneveld (1984) for IAFB, Collier (1981, 1982), Tong and Weisman (1996), etc.

Correlations are often expressed in the modified form of a reference equation: the Dittus-Boelter equation (1930) for single-phase vapor heat transfer is often used in DFFB and the Bromley pool-boiling equation (1950) is employed in IAFB. They are based on the assumption that both the vapor and the liquid are under the thermal-equilibrium state (i.e., the vapor temperature is close to the saturation). For example: Dougall and Rohsenow correlation (1963) and Groeneveld correlation (1972) for DFFB and Anderson correlation (1976) for IAFB. While the application of correlations is limited, the prediction accuracy is usually good at conditions within the range of the database.

These correlations are not recommended for extrapolation to conditions outside the database because they often exhibited incorrect asymptotic and parametric trends and can result in erroneous predictions.

Phenomenological equations can be considered as a type of correlation. It employs the correlation for single-phase heat transfer, and includes modifications to satisfy the phenomena of PDO heat transfer (Groeneveld and Delorme 1976). The main component of this correlation is the ability of predicting the vapor superheat allowing non-equilibrium between the two phases. Despite many attempts (e.g., Chen et al. (1984)), there remains to be a lack of experimental data on vapor superheat at PDO conditions. This hampers the validation of the vapor-superheat predictions from these correlations. Nevertheless, this type of correlation is the most common because of its wide range of applications. Furthermore, it can be extrapolated to conditions beyond the data base because the formulation of these correlations provides correct parametric and asymptotic trends.

Semi-analytical models were developed with the conservative equations (i.e., mass, momentum and energy) (e.g., Saha model (1980) for DFFB and Johannsen and Mosaad model (1989) for IAFB). Due to the lack of knowledge for most thermalhydraulic parameters, all closure relationships employed in these models were empirically based. They affect significantly the accuracy of the model because most of these empirical relationships were derived with low-pressure data and applied directly to high-pressure conditions. For the same reasons, these models cannot be extrapolated to conditions outside of their validation database. This further limits the range of applications of the models.

Recently, a look-up table for PDO heat transfer coefficients was developed by Leung et al. (1997). It is a normalized database that presents the heat transfer coefficients at various discrete values of flow conditions (i.e., pressure, mass flux, thermodynamic quality and heat flux). The tabulated heat transfer coefficients were weighted-average values of all data within the neighboring conditions. Hence, the PDO look-up table provides the closest representation of the data base (within the data uncertainty). At conditions outside of the data base, the tabulated values were calculated with the

Groeneveld and Delorme correlation (1976) at the DFFB region and the Hammouda model (1996) at the IAFB region (both of them were shown to give reasonable prediction accuracy and cover the widest range of flow conditions by Leung et al. (1997)). An assessment with the available database showed that the PDO look-up table provides the best prediction accuracy for fully developed PDO conditions, but underestimates the heat transfer coefficients for developing flow.

2.2.3 Applications of Prediction Methods for Film-Boiling Heat Transfer in Rod-Bundle Analyses

Most prediction methods were developed for fully developed flow in vertical tubes, which are generally the simplest test configurations. However, they are often applied to other geometries (such as rod bundles) and developing conditions. The most common approach is to employ the tube-based prediction method for providing the reference heat transfer coefficient and using modification factors to account for various separate effects. The Nusselt number for any geometry at a location and flow conditions of interest is expressed as

$$Nu = Nu_{tube}\, K_{shape}\, K_{spacer}\, K_{dev.}\, K_{AFD} \;\cdots\cdots \qquad \textbf{(2-1)}$$

where Nu_{tube} is the Nusselt number of tubes at the same flow conditions, K_{shape}, K_{spacer}, $K_{dev.}$ and K_{AFD} are the modification factors for the effects of channel cross-section shape, spacer , flow development and axial heat-flux distribution, respectively. There are other separate effects influencing the Nusselt number; those mentioned above are anticipated to have the most significant impact. This equation implies that these effects are mutually independent from each other, which represents a simplified assumption. In some cases, these effects may inter-relate with each other and is more difficult to quantify them separately. As described in the introduction, the present study focuses on the effects of cross-sectional shape and spacing devices on PDO heat transfer. Both effects can be generally categorized as part of the geometry effect since both shape (which also includes the gap-size effect) and spacing devices are part of the channel configurations.

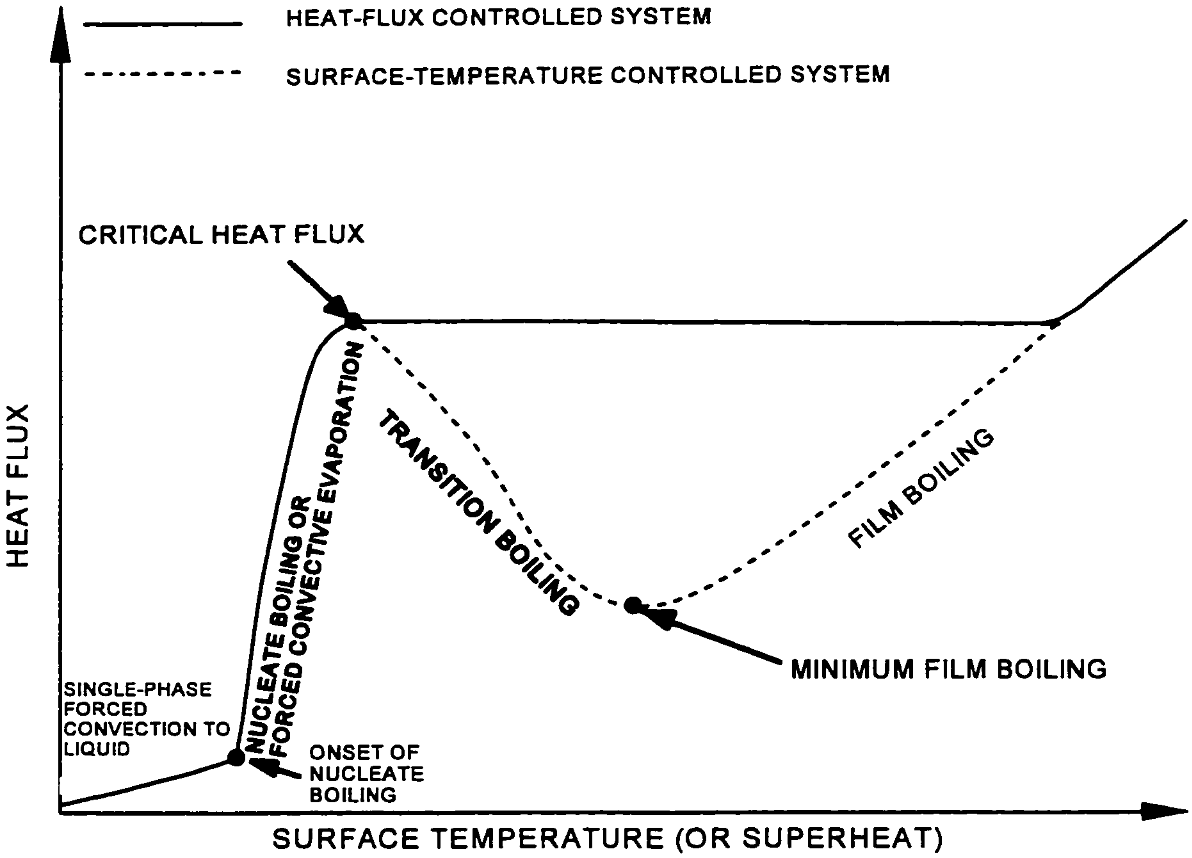

Figure 2.1. Boiling curve (Collier and Thome, 1994)

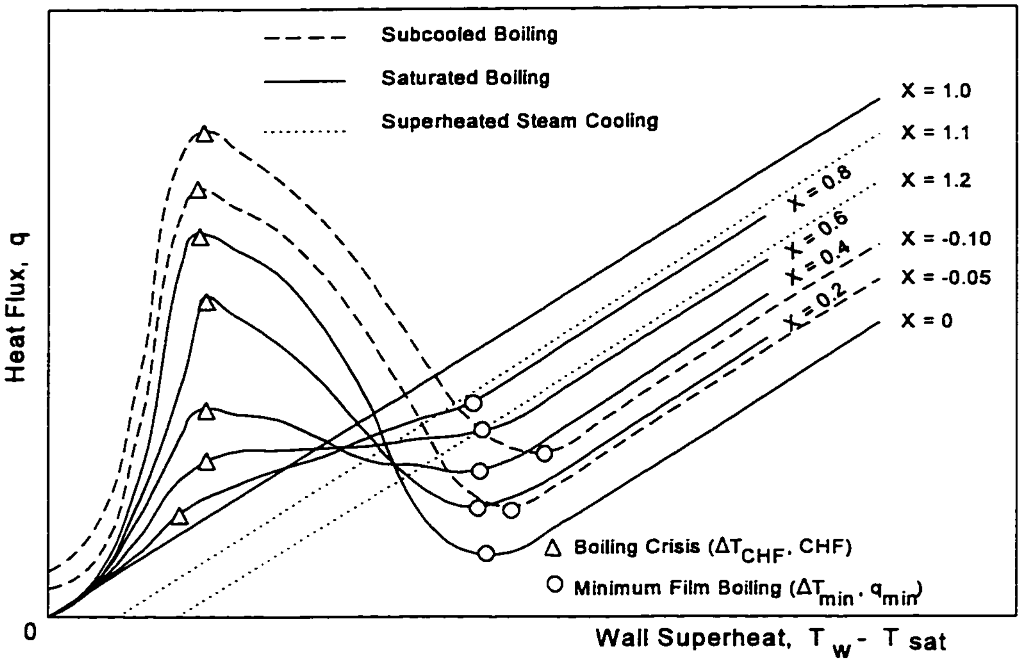

Figure 2.2. Effect of a change in thermodynamic quality on the flow-boiling curve (Groeneveld et al., 1989)

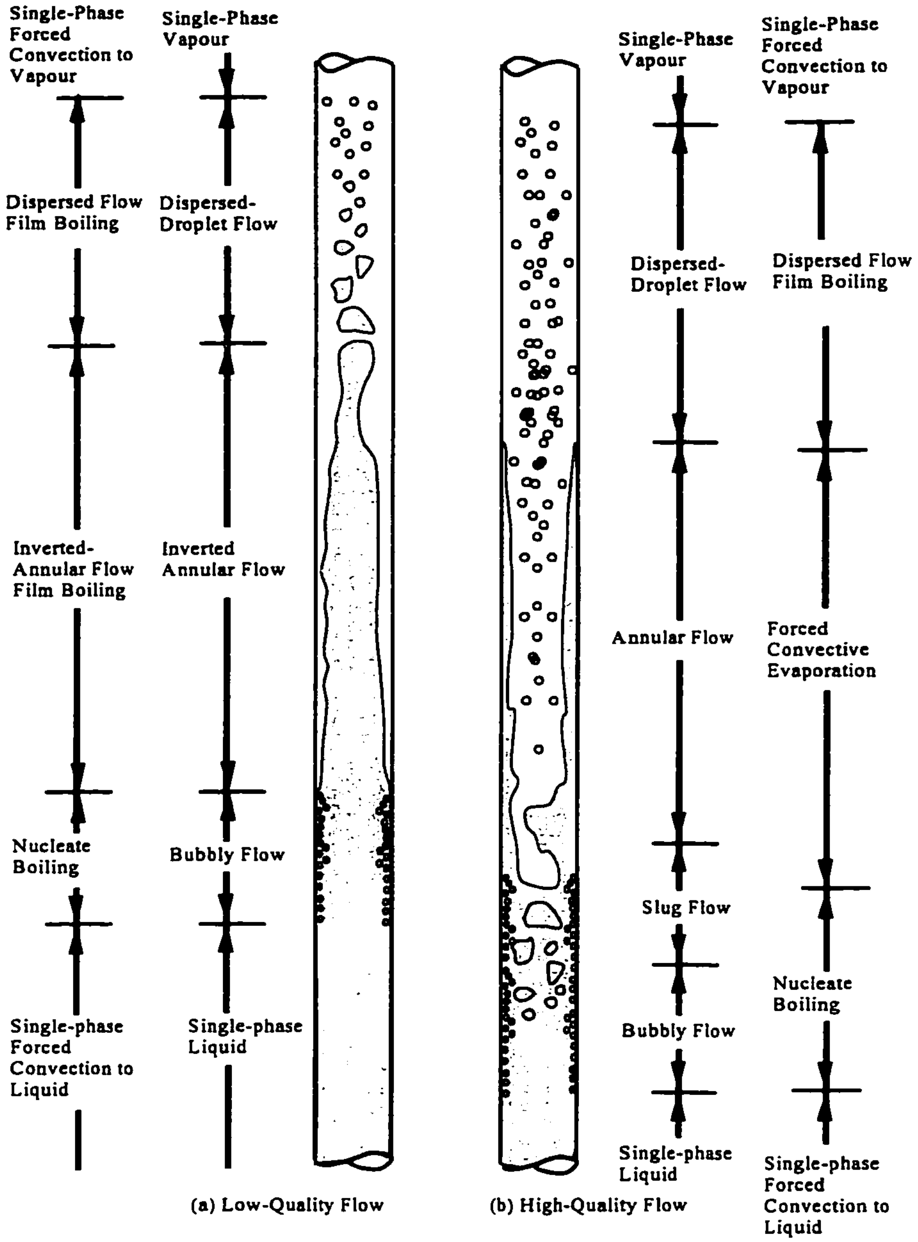

Figure 2.3. Heat transfer mode and flow pattern variations in heated channels (Collier and Thome, 1994)

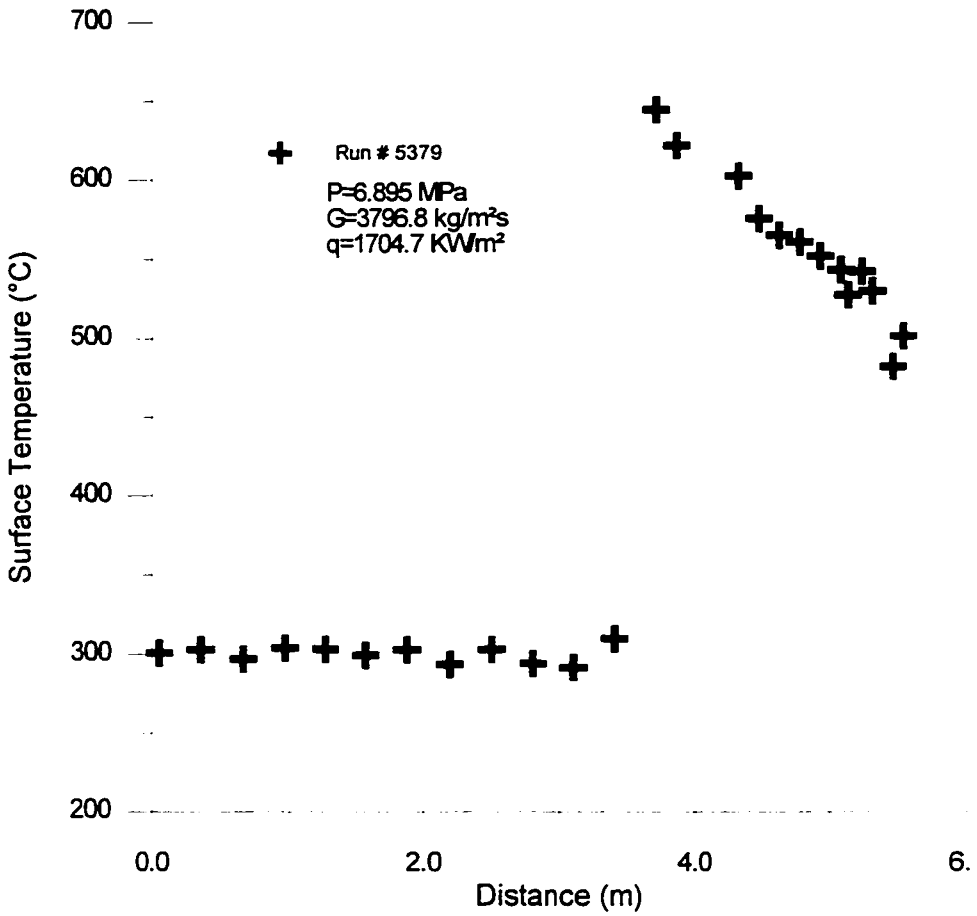

Figure 2.4. Surface temperature distributions obtained by Bennett et al. (1967)

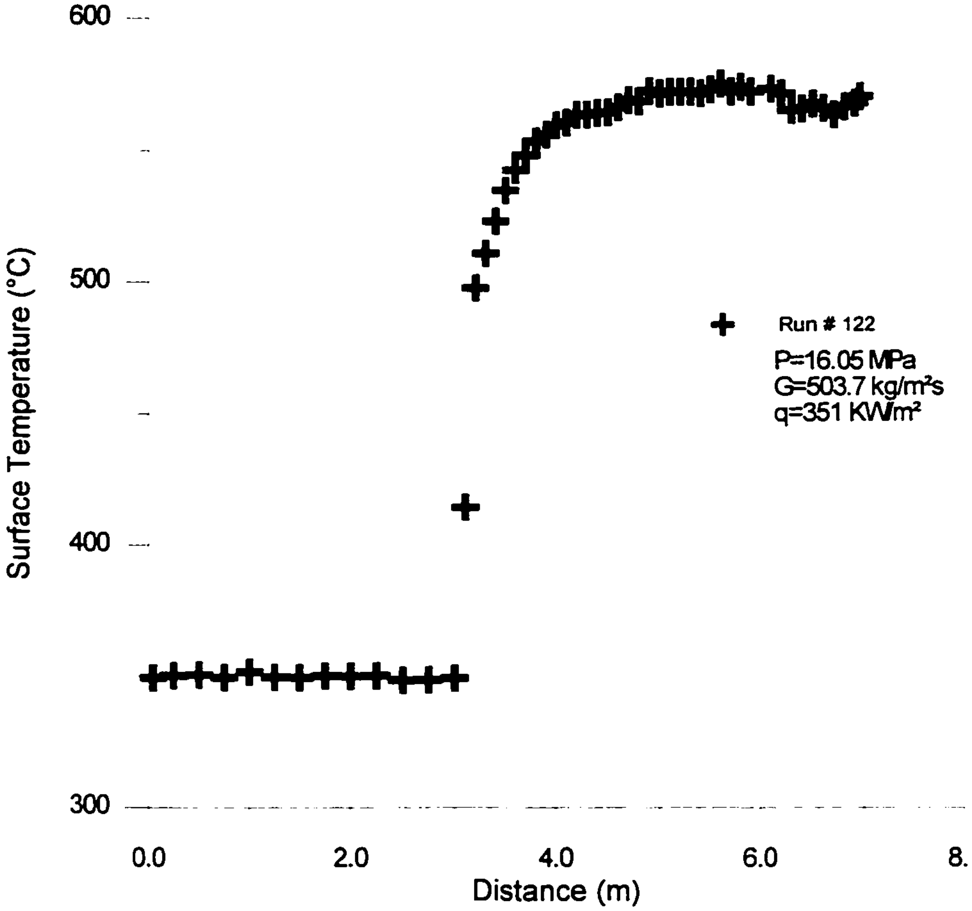

Figure 2.5. Surface temperature distributions obtained by Becker et al. (1983)

3. A REVIEW OF LITERATURE ON EFFECTS OF CROSS-SECTIONAL SHAPE AND SPACING DEVICES ON PDO HEAT TRANSFER

A literature review was carried out to examine the available information on the effects of cross-sectional shape and spacing devices on PDO heat transfer. The effect of cross-sectional shape can be subdivided into several sub-effects: corner, gap and heating conditions of neighboring surfaces. Other sub-effects (e.g., surface curvature) are anticipated to be small at PDO conditions. Overall, the available information (both prediction methods and experimental data) on these effects is scarce at PDO conditions. The single-phase heat transfer studies related to these effects have also been included to expand the review. They can be used to provide information on high-quality PDO conditions, which resemble closely to the single-phase vapor flow.

The effect of shape is generally less significant than the effect of spacing devices, but can be a dominant factor in channels with a narrow gap. Prediction methods recommended for these effects are generally applicable for a limited range of flow conditions and cannot be extended to other conditions and/or geometries. Therefore, a more generalized approach is needed for predicting these effects.

3.1 Cross-Sectional Shape Effect

The effect of cross-sectional shape on single-phase and PDO heat transfer is examined by comparing the heat transfer data of non-circular channels against those of tubes. Non-circular channels include triangular-shaped channels, rectangular-shaped channels, annuli, bundles, etc. The effect of shape for either the triangular- or rectangular-shaped channels lies primarily on the apex-angle size of corners, while that for annuli and bundles depends on the gaps between heated surfaces. Table 3.1 summarized various studies on the geometry effect and Table 3.2 provided those on the gap-size effect.

3.1.1 Triangular-Shaped Channels

Study of Eckert and Irvine (1960). Eckert and Irvine (1960) measured the surface temperature of a channel having a cross-sectional shape of an isosceles triangular with the apex angle of 11.5°. The two sides were 12.7 cm and the bottom one was 2.54 cm. The hydraulic diameter of the channel was 2.296 cm. All three sides of the channel were heated and were cooled by air. Their measurements showed that the average heat transfer coefficient over the circumference of the channel was lower than that of a tube (based on the equivalent hydraulic diameter approach). Figure 3.1 shows the comparison between data and calculated values of the Dittus-Boelter equation over the Reynolds number range from 4300 to 24000. A smaller increases in Nusselt number is also shown for the triangular-shaped channel than tubes with increasing Reynolds number. Eckert and Irvine (1960) stated that the reduction in Nusselt number is caused by the decrease in turbulent diffusivity, which affects strongly the heat transport, in a triangular duct than a tube.

Study of Altemani and Sparrow (1980). Altemani and Sparrow (1980) also studied the heat transfer in an air-cooled channel with the cross-section shaped like an equilateral triangle. Only two of three surfaces were heated. The side of triangular was 3.97 cm and the hydraulic diameter was 2.29 cm. A comparison between their data and the calculated values of the Dittus-Boelter equation showed that the use of equivalent-hydraulic diameter approach is inappropriate for this configuration. The corner effect was also studied by comparing the Nusselt numbers of channels with either sharp or rounded corners. Altemani and Sparrow (1980) showed that the Nusselt number is the lowest for a channel with sharp corners and is the highest for a tube (Figure 3.2). The Nusselt number for the channel with rounded corners is slightly lower than that of a tube.

Study of Usui et al. (1982). Usui et al. (1982) used a similar test section to that of Eckert and Irvine (1960); an isosceles triangular duct with the apex angle of 11.4°. The hydraulic diameter of their test section was 1.797 cm. The two sides were 10 cm and the bottom side was 2 cm. As previously observed by Eckert and Irvine (1960), the data of the triangular-shaped channel were much lower than the calculated values of Dittus-Boelter equation. Usui et al. (1982) concluded that the coexistence of laminar and turbulent flows in the corner region led to the reduction of heat transfer coefficient at the narrow-angle corner.

3.1.2 Rectangular-Shaped Channels

Study of Novotny et al. (1964). Novotny et al. (1964) measured the surface temperatures of several rectangular channels having aspect ratios (height/width) of 0.1, 0.2 and 1. The two long-side surfaces were heated uniformly while the two short-side surfaces were insulated. A turbulent flow of air was circulated through the heated channel at a Reynolds number range between 10^4 and 10^5. Their results showed that the Nusselt numbers of rectangular-shaped channels are slightly lower than the calculated values of the Dittus-Boelter equation (based on the equivalent-hydraulic diameter approach). The difference increases with increasing Reynolds number.

Study of Sparrow et al. (1966). Sparrow et al. (1966) studied the effect of asymmetrical heating with a rectangular duct of an aspect ratio of 0.2. The test section was cooled with a turbulent flow of air. One of the two long sides was heated with a uniform heat flux, while the other three sides were insulated. As shown in Figure 3.3, the experimental data agree, in general, with the calculated values of the Dittus-Boelter equation. A slight overprediction was observed at low Reynolds numbers.

3.1.3 Annuli

Studies of Koizumi et al. (1984, 1987). Koizumi et al. (1984, 1987) obtained heat transfer measurements with steam-water flow inside a heated annulus. Their test section consisted of a heated inner rod and an insulated outer shroud. The spacing between inner and outer tube was maintained with spacers along the test section. A strong effect of spacing devices was observed in their data. Nevertheless, Koizumi et al. (1984, 1987) concluded that the post-dryout heat transfer depends strongly on the wall superheat; a low heat transfer coefficient was observed for high wall superheat.

Study of Hwang and Jensen (1991). Hwang and Jensen (1991) analyzed the heat transfer for a fully developed laminar PDO flow in an eccentric annulus. The inner rod of the annulus was maintained at a constant temperature while the outer surface was insulated (Figure 3.4). The liquid droplets in the superheated vapor steam was considered as distributed heat sinks. A higher vapor temperatures were found at the narrow gap than the wide subchannel of the eccentric annulus. For a given heat sink parameter S, the average Nusselt number decreases with increasing eccentricity ratio, $\varepsilon=e/(r_o-r_i)$, at a constant radius ratios, γ, and increases with decreasing radius ratio at a constant eccentricity ratio. This increase in heat transfer was due primarily to the presence of well-dispersed saturated droplets in the superheated vapor stream. A large value of S means a strong heat-sink effect and a high heat transfer rate from the heated wall (Figure 3.5).

3.1.4 Bundles

Study of Kumamaru et al. (1987). Kumamaru et al. (1987) measured the surface temperatures of a 5×5 rod bundle under high pressure and low mass-flux conditions. Several spacing devices were used to maintain the gap size between rods. The closest thermocouples to a spacer was located at a downstream location of about 21.2 hydraulic diameter, D_{hy}. These data were not affected by the presence of the spacing devices; there was no downstream or upstream effects. The measured surface-temperature distributions along the elements were smooth but were mostly under the developing-flow effect. A comparison between data and predictions of several correlations showed that the Varone and Rohsenow correlation (1984) provided the best predictions over the whole region of the present experimental conditions.

The Hassan Study (1987). Hassan (1987) measured the PDO vapor temperature in a 3×3 rod bundle. The vapor temperature was shown to be functions of both the wall-vapor and vapor-droplet heat transfer. Under a high evaporation rate, the droplet evaporation reduces the vapor-droplet convective heat transfer and the Nusselt number cannot be adequately correlated with Reynolds and Prandtl numbers only. Hassan (1987) introduced a mass-transfer number in the calculation of the interfacial heat transfer between droplets and steam.

Studies of Yoder et al. (1981, 1982a, 1982b, 1983). Yoder et al. (1983) measured the PDO surface temperatures along a 8×8 rod bundle. The surface temperature was found to affect by the degree of non-equilibrium and the vapor temperature. A lower effective heat transfer was observed for high degree of non-equilibrium and vapor temperature. This resulted in an increase in the heated surface temperature.

A strong effect of spacer grids on PDO surface-temperature distributions has also been observed. The surface temperature decreases sharply across the spacer grids (Figure 3.6) with a corresponding increase of 214% in heat transfer coefficient. This signifies the transition of heat transfer mode from the less efficient film boiling to the more efficient transition boiling or nucleate boiling at the heated surface. It is anticipated that the boundary layer downstream of the spacer grids is destroyed and a new layer is established. The establishment of a new steady boundary layer spreads over a distance of 20 to 30 hydraulic diameters downstream of the spacer. Yoder et al. (1981, 1982b) observed both the local and global effects of spacers on the surface-temperature distribution. A decrease of 70 to 150 K in surface temperature was measured across the spacer grids.

Yoder et al. (1982a, 1982b) assessed several correlations of PDO heat transfer in the DFFB region. Both Chen et al. (1978) and Yoder-Rohsenow (1980) correlations were shown to underpredict the heat transfer coefficient. The Jones-Zuber (1977) correlation overpredicted the heat transfer coefficient at conditions near the dryout point but underpredicted the coefficient at conditions far away from dryout.

Studies of Morris et al. (1982, 1985). Morris et al. (1982, 1985) obtained additional PDO data with the 8 × 8 test bundles of Yoder et al. (1982b). Their data exhibited similar trends to those previously observed by Yoder et al. (1982b). The heat transfer coefficient in bundles is generally higher than those of tubes and annuli. Morris et al. (1985) compared their data against the predictions of several correlations. They concluded that most correlations, derived with the assumption of thermal-equilibrium between phases (e.g., Dougall-Rohsenow correlation (1963)), overpredict the heat transfer coefficient. The correlations, based on the thermal non-equilibrium assumption (e.g., Groeneveld-Delorme correlation (1976)), provide a better agreement with the data at fully developed PDO conditions. They tend to underpredict the heat transfer coefficient at conditions near the dryout point, where developing flow is encountered.

Study of Sugimoto and Murao (1984). Sugimoto and Murao (1984) obtained surface temperature measurements along a 6×6 rod bundle. The rod diameter of the bundle was 10.7 mm and the heated length was 3.6 m. A strong effect of spacer grids was observed; the heat transfer coefficients at locations downstream of the spacer increase by 20 to 50% as compared to those at the upstream locations. Sugimoto and Murao (1984) stated that the heat transfer enhancement is caused by the breakup of droplets over the spacers. The reduction in droplet diameter increases the interfacial area and hence the heat transfer.

Analysis of Groeneveld (1973). Groeneveld (1973) compiled a large data base of single-phase heat transfer in bundle geometries, and observed a strong effect of rod spacing on heat transfer. A bundle distortion factor, I, was introduced to characterize the differences in heat transfer between tubes and bundles. It is expressed as

$$I = \frac{h_{bundle}}{h_{tube}} \tag{3-1}$$

where h_{bundle} and h_{tube} are heat transfer coefficients in bundles and tubes at the same cross-sectional average flow conditions. For bundles having a localized narrow gap, the local heat transfer rate is further reduced. Groeneveld (1973) proposed also a gap-effect factor for predicting the minimum local heat transfer coefficient at the narrow gap between rods. The gap-effect factor is expressed as

$$J = \frac{h_{\min}}{h_{bundle}} \tag{3-2}$$

where $h_{\min}$ is the minimum local heat transfer coefficient in the gap region based on the cross-sectional average flow conditions.

Study of Möller and Tschöke (1980). Möller and Tschöke (1980) studied the effect of element bowing on heat transfer using a 19-rod bundle, which was cooled with a sodium flow. A strong effect of gap size was observed with the highest surface temperature measured at the minimum gap region. Figure 3.7 presents the azimuthal temperature distributions of the adjacent rods as the bowed rod moved towards them. The surface temperature increases significantly as the gap size is reduced.

Study of Guellouz and Tavoularis (1992). Guellouz and Tavoularis (1992) studied the heat transfer in rod bundle subchannels with varying rod-wall proximity. Figure 3.8 shows the set up of the test section. A constant air flow is circulated through the test section. The instrumented rod was moved from the reference location (W/D = 1.149) upward to the boundary. A strong effect of gap size on heat transfer was observed. Figure 3.9 presents the ratios of circumference heat transfer coefficient with respect to the reference location at various gap sizes. The minimum heat transfer coefficient was shown at the narrow-gap regions. A large decrease of the heat transfer ratio was observed when W/D approaches to 1. For large gap sizes (W/D ~ 1.149), the variation of heat transfer coefficient becomes less sensitive to the gap size.

Analysis of Guellouz and Tavoularis (1995). Guellouz and Tavoularis (1995) expanded the analysis of Groeneveld (1973) by including more recent experimental data for single-phase heat transfer in rod bundles. Figures 3.10 and 3.11 present, respectively, the bundle distortion factor, I, and the minimum-gap factor, J, as a function of the pitch-to-rod-diameter (P/D) ratio. As observed previously by Groeneveld (1973), the heat transfer coefficient decreases with decreasing gap size (small P/D ratios). It approaches the heat transfer coefficient for tubes for large gap sizes.

3.1.5 Irregular Shape

Study of Burdunin et al. (1987). Burdunin et al. (1987) measured the PDO surface temperatures along a channel simulating the subchannel between four rods (outer diameter of 13 mm). Figure 3.12 shows the schematic diagram of the test section. Measurements of surface temperature over the channel perimeter showed that dryout initiated at the narrow-gap region. The PDO heat transfer coefficient increases with increasing mass flux and quality. However, the measurements covered primarily the developing-flow region; the transition from developing to fully developed conditions increases with increasing heat flux but decreases with increasing mass flux (Figure 3.13). Burdunin et al. (1987) compared their data against the predictions of a bundle-based correlation proposed by Mattson et al. (1974). Most data were underpredicted by the correlation with differences up to 50%.

3.2 Effect of Spacing Devices

Spacing devices are primarily introduced to rod bundles to maintain the gap size between elements and minimize flow-induced vibration to each element. Their presence promotes turbulence; this results in an increase in pressure loss and heat transfer enhancement. However, the enhancement of turbulence is relatively short-lived and decays with increasing distance downstream from the device. Table 3.3 summarizes the studies of the spacer effect on PDO heat transfer in channels other than rod bundles, while Table 3.4 provides those in rod bundles.

Survey of Groeneveld and Yousef (1980). Groeneveld and Yousef (1980) examined the effect of spacing devices on critical heat flux and PDO heat transfer. They concluded that spacing devices enhance significantly the PDO heat transfer by improving subchannel mixing and enhancing turbulence in the region just downstream of the spacers. Groeneveld and Yousef (1980) presented a summary of correlations for the spacer effect. Most of the correlations are expressed in terms of a Nusselt-number ratio between spacer-equipped and no-spacer channels:

$$\frac{Nu}{Nu_0} = 1 + A\exp\left(-B\frac{Z}{D_{hy}}\right) \tag{3-3}$$

where A and B are geometry-dependent correlating constants, Z is the axial distance downstream from the spacer and D_{hy} is the hydraulic-equivalent diameter.

Study of Hassan and Rehme (1981). Hassan and Rehme (1981) investigated the spacer-grid and surface-roughness effects on single-phase heat transfer with a 3-rod bundle. The tests covered the Reynolds-number range from 600 to 2×10^5. Various sizes of spacer grid, with blockage-area ratio, ϵ, varied between 25% to 35%, were tested in both smooth and rough bundles. The enhancement of heat transfer was observed at locations both upstream and downstream of the spacer. The affected region at the upstream locations covers the distance approximately equal to one hydraulic diameter. This enhancement is caused by the gradual increase in velocity as the flow adjusts for the flow-area contraction at the spacer. At or just downstream of the spacer, the heat transfer coefficient (or Nusselt number) approaches the maximum value, beyond which the heat transfer coefficient decreases exponentially with increasing distance away from the spacer.

Figure 3.14 shows axial distribution of Nusselt-number ratio, Nu^*, on a rough surface for three different blockage ratios. The enhancement effect is strong (i.e., large Nu^*) at low Reynolds numbers, but appears to be diminished with increasing Reynolds number. This reduction in the enhancement effect is caused by the fact that the flow is approaching the complete turbulent region at high Reynolds number and additional effects (spacers or surface roughness) can no longer raise the level of turbulence further. A strong enhancement of heat transfer was shown for large blockages as compared to small blockages at the same Reynolds number. It is caused by the increase in velocity as the flow passes the blockage, which promotes further the turbulence level at the downstream locations. This results in an increase in heat transfer coefficient.

Study of Yao et al. (1982). Yao et al. (1982) examined the spacer-grids effect on single-phase heat transfer. They compiled several data sets of single-phase heat transfer and observed a strong enhancement effect at locations downstream of the spacer (Figure 3.15). The boundary layer phenomenon was found to be similar to the entry-length effect in turbulent tube flow. At locations downstream of the spacer, the heat transfer augmentation decays exponentially with increasing distance from the spacer. Yao et al. (1982) introduced a correlation for the enhancement effect of spacer on single-phase heat transfer. Their correlation is expressed as

$$\frac{Nu}{Nu_0} = 1 + 5.55\,\epsilon^2 \exp\left(-0.13\,\frac{Z}{D_{hy}}\right) \tag{3-4}$$

where Nu and Nu_0 are Nusselt numbers for spacer-equipped and no-spacer channels, respectively.

Study of Unal et al. (1988). Unal et al. (1988) measured the PDO surface temperature along a nine-rod bundle. The spacings between rods were maintained with one grid-type spacer located at 76 cm from the inlet. The measurements showed a large temperature drop across the spacer. This heat transfer enhancement was significant at high mass flux conditions, but less apparent at low mass fluxes. Figure 3.16 shows the surface-temperature distribution along the heated rod.

Study of Kim and Korol'Kov (1991). Kim and Korol'Kov (1991) obtained PDO surface-temperature measurements along an annulus. They concluded that the strong enhancement effect of spacer on PDO heat transfer was caused by the increases in (i) coolant velocity from the reduction in flow area at the spacer location, (ii) heat transfer from the heated surface to the coolant by conduction through the spacer, (iii) radiant heat transfer directly from the heated surface to the spacer, and (iv) interfacial heat transfer area from the breakup of the droplets by the spacer. Based on the correlation of Yao et al. (1982), Kim and Korol'Kov (1991) introduced a correlation for the enhancement effect:

$$\frac{Nu}{Nu_0} = 1 + K_e\,\epsilon^2 \exp\left(-0.13\,\frac{Z}{D_{hy}}\right) \tag{3-5}$$

where K_e is the heat transfer enhancement factor, defined as

$$K_e = A(x_e - x_{thr})(1 - x_e) \tag{3-6}$$

x_e is the equilibrium quality, x_{thr} is a flow dependent function defined as

$$x_{thr} = 1 - 0.86 e^{-19/\psi} \tag{3-7}$$

and ψ is expressed as

$$\psi = G \sqrt{\frac{D_{hy}}{\sigma \rho_f}} \tag{3-8}$$

G, σ and ρ_f are the mass flux, surface tension and saturated liquid density, respectively. The constant, A, is a correlated parameter, and was found to be 21700 for a box-typed spacer (Kim and Korol'Kov (1991)).

Study of Sergeev et al. (1990). Sergeev et al. (1990) measured the surface temperature distributions along a tube equipped with several spacers at high quality PDO conditions. Two configurations of spacer were tested: one with an axial length of 2 mm and blockage-area ratio of 0.154 while the other with length of 5 mm and blockage-area ratio of 0.326. The spacers were separated over a distance of 0.1 m and 0.5 m in two different tests. Sergeev et al. (1990) observed both local and global effects of spacer on PDO heat transfer. Other than the exponential-decay trend of heat transfer at locations downstream of the spacer, a consistent overall increase in heat transfer was observed when comparing data of different blockage-area ratios (Figure 3.17).

Study of Sugimoto and Murao (1984). Sugimoto and Murao (1984) derived a grid spacer model for dispersed flow film boiling. The equation of Yao et al. (1982) was used to calculate the heat transfer enhancement between surface and vapor at locations downstream of the spacer. In dispersed flow, the heat transfer enhancement is realized by the increase of interfacial surface area resulting in the increase of vapor to droplet heat transfer. Figure 3.18 shows the comparison between model predictions and experiment data. The temperature predictions follow closely the trend displayed by the data, and the agreement between predictions and data is generally good.

Study of Shiina et al. (1991). Shiina et al. (1991) measured the surface temperature distribution along the rectangular channel equipped with a spacer. Fourteen different types of spacers were used in their experiment; the spacer having a rectangular cross-sectional area in the flow direction is considered as the reference shape. Heat transfer enhancement was observed at locations downstream of the spacers. Based on their analysis, Shiina et al. (1991) suggested that the shape of the leading edge of a spacer influences primarily the pressure drop while the shape of the trailing edge has a large impact on the heat transfer. They showed that the cylindrical-rod-type spacer, spacers with front edge cutting, and those with both edges cutting provide the best overall heat transfer enhancement.

Table 3.1 Experimental studies on the effect of cross-sectional shape on PDO heat transfer

REFERENCE	GEOMETRY	FLOW CONDITIONS	OBSERVED EFFECT
Abraham (1966)	Annulus OD = 19.3 mm ID =15.2 mm	$G = 1356\text{–}4068\ \mathrm{kg \cdot m^{-2} \cdot s^{-1}}$, $P = 4, 6.9, 8.3$ MPa, $q_w = 21\text{-}1893\ \mathrm{KW \cdot m^{-2}}$	No comparison was made with tube data.
Koizumi et al. (1984, 1987)	Annulus	$G = 100\text{-}310\ \mathrm{kg \cdot m^{-2} \cdot s^{-1}}$, $P = 3.1$ MPa	Data showed localized spacer effects. The data exhibited similar trends to tube post-dryout heat transfer data. Also, these data could be compared to tube correlations or data.
Burdunin et al. (1987)	"Dumbbell" shape subchannel	$G = 30\text{–}455\ \mathrm{kg \cdot m^{-2} \cdot s^{-1}}$, $P = 3.1\text{-}7.3$ MPa, $q_w = 71\text{-}960\ \mathrm{KW \cdot m^{-2}}$	The transition region length depends on both the heat flux and mass flux. The heat transfer coefficient decreased with increasing x_{eq}, and increased with increasing mass flux. At low mass fluxes, the measured vapor superheat increased sharply with increasing channel total power. At higher mass fluxes, the rate of increase of vapor superheat reduced considerably. In general, the vapor superheat increased with increasing heat flux.

Table 3.2 Experimental studies on the effect of gap size on single-phase and PDO heat transfer

REFERENCE	GEOMETRY	FLOW CONDITIONS	OBSERVED EFFECT
Möller and Tschöke (1980)	19-rod bundle cooled with sodium flow, element diameter is 9 mm, hydraulic diameter is 6.75 mm, pitch-to-diameter ratio is 1.3, element-to-flow-tube gap is 2.19 mm, bowed-element-to-element gap size from 0.54 to 5 mm	$P \leq 0.4$ MPa, Flow rate ≤ 60 $\mathrm{m^3.h^{-1}}$, Coolant temp. ≤ 650 °C	Azimuthal temperature distributions provided for various elements neighboring to the bowed element at different bowing positions. A sharp rise in surface temperature is observed for gap sizes less than ~2 mm.
Johnston et al. (1983, 1986)	Single tube above a flat surface, tube diameter is 18.9 mm, gap sizes from 0 to 0.125 mm	$P = 0.69$ MPa, $G = 0.6\text{-}1.62\ \mathrm{Mg \cdot m^{-2} \cdot s^{-1}}$	Vertical upward flow at low pressures. Covered both CHF and heat transfer.
Fahmy et al. (1986)	Annulus, outer-tube diameter is 26 mm, inner tube diameter is 14 mm, gap sizes from 3 to 6 mm	$P = 0.1$ MPa	Vertical upward flow. Local Nusselt number along the heating element decreases with increasing eccentricity.
Guellouz and Tavoularis (1992)	5-rod bundle sub-section, flow tube diameter = 1332.4 mm, element OD = 168.27 mm, element-to-outer tube gap = 0 to 23.56 mm	$P = 0.1$ MPa	Air cooled horizontal test section; 13 times the size of a CANDU bundle. Measurements of flow velocity, turbulence and heat transfer for various gap sizes.
Ouma and Tavoularis (1991)	5-rod bundle sub-section, flow tube diameter = 1015.7 mm, element OD = 128.27 mm, element-to-outer tube gap = 0 to 23.56 mm	$P = 0.1$ MPa	Air cooled horizontal test section; 13 times the size of a CANDU bundle. Measurements of flow velocity, turbulence and heat transfer for various gap sizes.

Table 3.3 Experimental studies on the effect of spacers on PDO heat transfer in non-rod-bundle geometries (see nomenclature for symbols)

REFERENCE	GEOMETRY	SPACER DETAILS	FLOW CONDITIONS	OBSERVED EFFECT
Era (1967)	Two annuli: (I) OD = 17 mm, ID = 15 mm (ii) OD = 15.2 mm, ID = 10.2 mm	Three ceramic cylindrical spacers D = 1.5 mm	$G = 800\text{-}3800\ kg{\cdot}m^{-2}{\cdot}s^{-1}$, P = 0.1 MPa	The PDO temperatures were reduced by 30% for spacers with L_s=40 cm
Cluss (1978)	Tube D = 12.5 mm	$\epsilon = 0.36$; cross-shaped t = 38 mm	$G = 25\ kg{\cdot}m^{-2}{\cdot}s^{-1}$, P = 0.1 MPa, T_w = 540-700 °C Bottom flooding	200% increase in heat transfer coefficient at spacer. Increase was due to (i) increased local velocity (ii) radiation to liquid deposited on spacer
Chen and Lee (1979)	Tube D = 13.8 mm Horizontal and vertical	Orifice type $\epsilon = 0.25\text{-}0.5$; L_s = 50 cm.	$G = 100\text{-}400\ kg{\cdot}m^{-2}{\cdot}s^{-1}$, P = 0.1 MPa, T_w = 270-800 °C Rewetting study	Rewetting velocity increased up to 60%. The maximum increase was for $\epsilon = 0.25$.
Sergeev et al. (1990)	Tube	Two spacers inserted at 0.1 and 0.5 m along the tube length $\epsilon = 0.154$ and 0.326	$G = 500\text{-}1500\ kg{\cdot}m^{-2}{\cdot}s^{-1}$, P = 9.8-17.8 MPa, $q_w = 170\text{-}1500\ KW{\cdot}m^{-2}$	A large and steep temperature drop just downstream of the spacers, and a global reduction of the overall temperature along the tube compared to the smooth tube data. Local and global temperature reduction increased with increasing ϵ, decreasing quality, and increasing G.
Shiina et al. (1991)	Rectangular channel	14 types of spacers. The standard spacer is with rectangular cross-sectional area in the flow direction: w = 20 mm, t = 4 mm, $\epsilon = 0.5$. Spacers were set away from the heated surface by a gap of 2 mm.	Single phase flow (air). Flow was hydrodynamically and thermally fully developed	Spacer effects on the heat transfer coefficient were observed up to 20 D_{hy}. All types of spacers showed similar trends. The standard spacer (with rectangular cross-sectional area) showed higher heat transfer enhancement than other types of spacers (semi-cylindrical, blunt, and streamlined spacers). Since the spacers were located away from the heated surface, the improvement in the heat transfer at the wall was attributed to the thinner temperature boundary layer caused by the main flow turbulence adjacent to the boundary layer.
Kim and Korol'Kov (1991)	Annulus	"Box-shaped" spacers L_s = 50 cm $\epsilon = 0.1$	$G = 847\text{-}1200\ kg{\cdot}m^{-2}{\cdot}s^{-1}$, P = 3.3-6.4 MPa	Enhanced heat transfer due to (i) increased coolant velocity caused by flow area reduction, (ii) conduction through the spacer grid, (iii) radiation to liquid deposited on the grid spacer, and (iv) large droplet breakup by the grid spacers.

Table 3.4 Experimental studies on the effect of spacers on PDO heat transfer in rod bundles

REFERENCE	GEOMETRY	SPACER DETAILS	FLOW CONDITIONS	OBSERVED EFFECT
Möller and Tschöke (1980)	19-rod bundle (hexagonal lattice) $P/D = 1.3$, $W/D = 1.19$	4 axially movable spacers $L_s = 27\ D_{hy}$ $D_{hy} = 6.75$ mm $\epsilon = 26\%$ for wall-channel rods and 20% for central-channel rods $w = 15$ mm	$W = 3500\ kg{\cdot}s^{-1}$, $P = 0.4$ MPa single-phase flow (sodium)	At the grid support points, great temperature peaks and temperature gradients in the axial and circumferential directions were observed. The temperature gradually decreases in the axial direction away from the spacer grid. The temperatures, away from the grid supporting points but within the grid region, decreases along the grid length in the flow direction.
Hassan and Rehme (1981)	3-rod bundle (triangular lattice), smooth and rough tubes	honeycomb-type spacers, blockage factor between 25% and 35%	Single-phase air flow Reynolds number from 600 to $2{\cdot}10^5$	Heat transfer enhancement reaches maximum just downstream of spacer, and decays exponentially with increased distance from spacer. The enhancement has also been observed at a short distance upstream of the spacer. Spacer effect is more pronounced in smooth than in rough surfaces.
Yoder et al. (1982a,1982b)	8 × 8 rod bundle (square lattice)	six egg-crate type spacer grids $L_s = 61$ cm	$G = 226\text{-}806\ kg{\cdot}m^{-2}{\cdot}s^{-1}$, $P = 4.38\text{-}13.37$ MPa, $q_w = 320\text{-}940\ KW{\cdot}m^{-2}$, $x_{do} = 0.373\text{-}0.967$	T_w downstream of a spacer are up to 110 °C lower than T_w upstream of the grid spacer. Spacer effects last ~20 to 30 D_{hy} downstream of the spacer. Grid spacer length effect is consistent with entrance length studies, and suggests a boundary layer breakup-rebuild process at the grid.
Sugimoto and Murao (1984)	6 × 6 rod bundle (square lattice)	7 spacers with a moveable central grid spacer	Bottom flooding. Flooding rate = 0.04 and 0.06 $m{\cdot}s^{-1}$. $P = 0.1$ and 0.2 MPa	The heat transfer coefficient is about 20 to 50% higher just downstream of the spacer than just upstream of it. The grid spacer at the mid-plane of the rod bundle rewetted early during the experiments. The sequence of flow regimes observed were single phase vapor, dispersed flow, and slug flow. Flow visualization showed that droplets just downstream of a spacer were smaller, thus increasing vapor-to-droplets heat transfer.
Kumamaru et al. (1987)	5 × 5 rod bundle (square lattice)	8 spacers in the heated region of the test section $L_s = 35.6\ D_{hy}$	$G = 80\text{-}320\ kg{\cdot}m^{-2}{\cdot}s^{-1}$, $P = 3$ MPa, $q_w = 30\text{-}260\ KW{\cdot}m^{-2}$	The closest T/C to a spacer was about 21.2 D_{hy} downstream of it. Data showed no downstream or upstream effects. The temperature profiles (plotted vs. axial distance) were smooth. The post-dryout data were mostly obtained in the under-developed film-boiling region.
Unal et al. (1988)	3 × 3 bundle (square lattice)	One grid spacer located 76 cm from the inlet	$G = 7\text{-}26\ kg{\cdot}m^{-2}{\cdot}s^{-1}$, $P = 0.105\text{-}0.120$ MPa, $q_w = 7\text{-}50\ KW{\cdot}m^{-2}$	Data showed strong spacer effects. Spacer effects less apparent at low mass fluxes

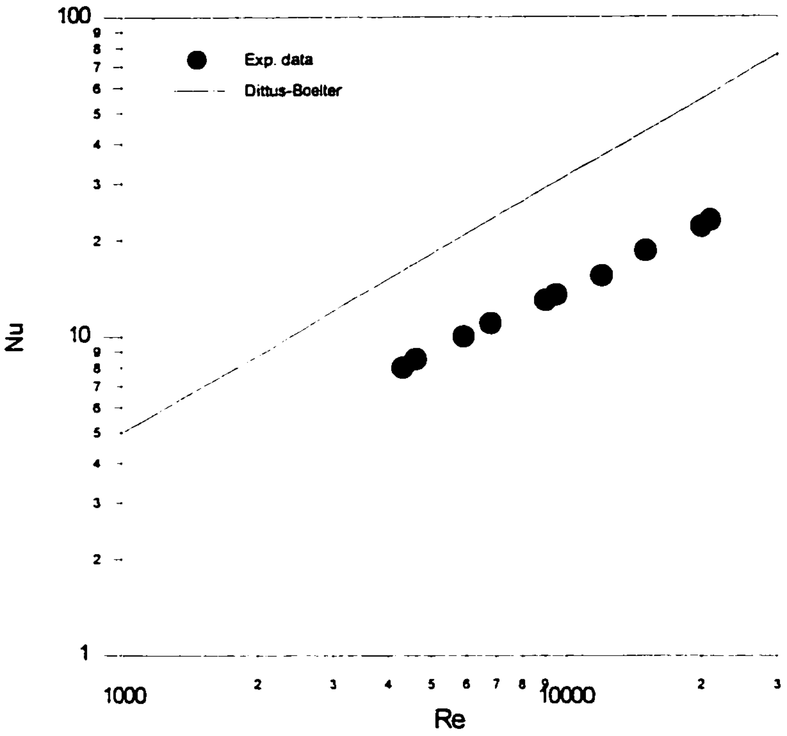

Figure 3.1. Nusselt number variation against Reynolds number (Eckert and Irvine, 1960)

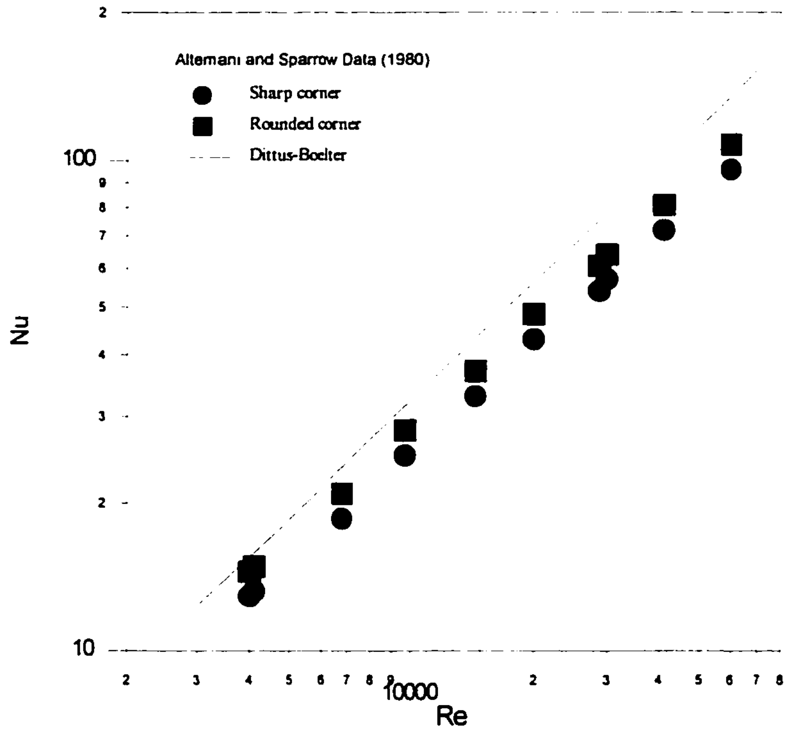

Figure 3.2. Comparison of Nusselt numbers between data for triangular channels and prediction of a tube-based equation

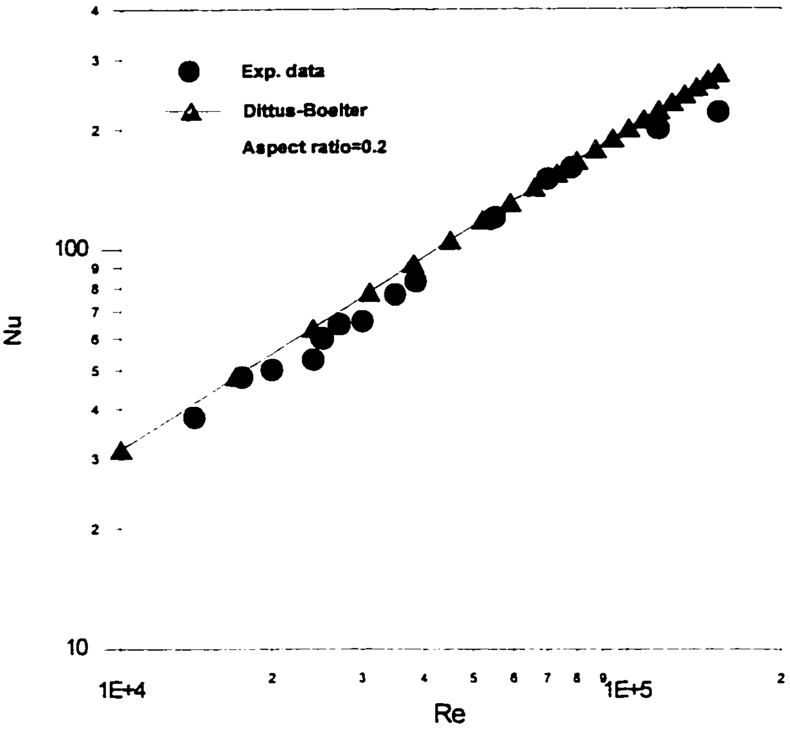

Figure 3.3. Experimentally determined Nusselt numbers (Sparrow et al., 1966)

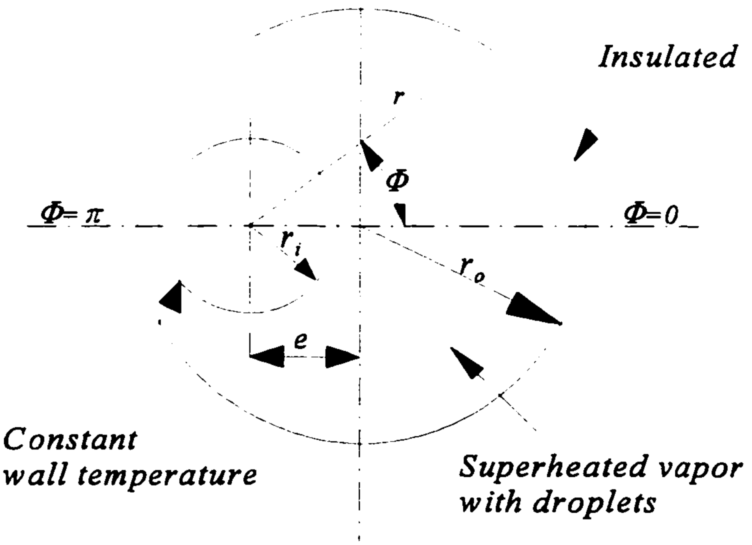

Figure 3.4. Schematic of dispersed flow in an eccentric annulus (Hwang and Jensen, 1991)

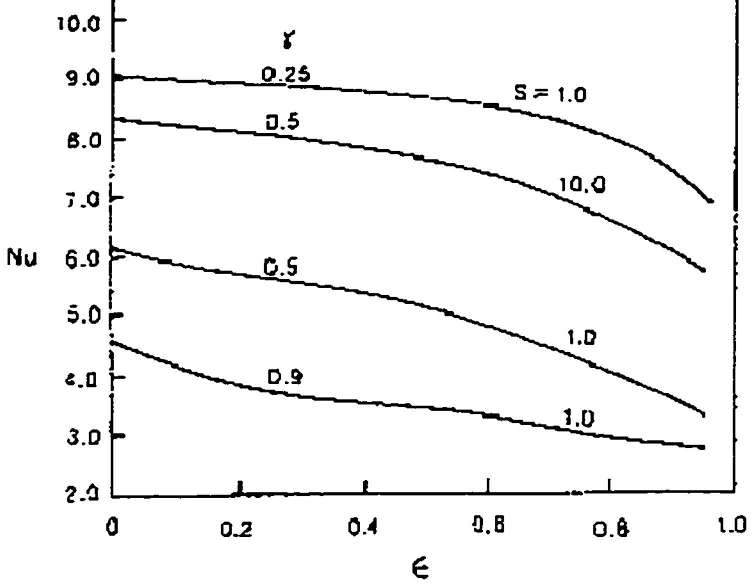

Figure 3.5. Effect of eccentricity ratio and radius ratio on Nu (Hwang and Jensen, 1991)

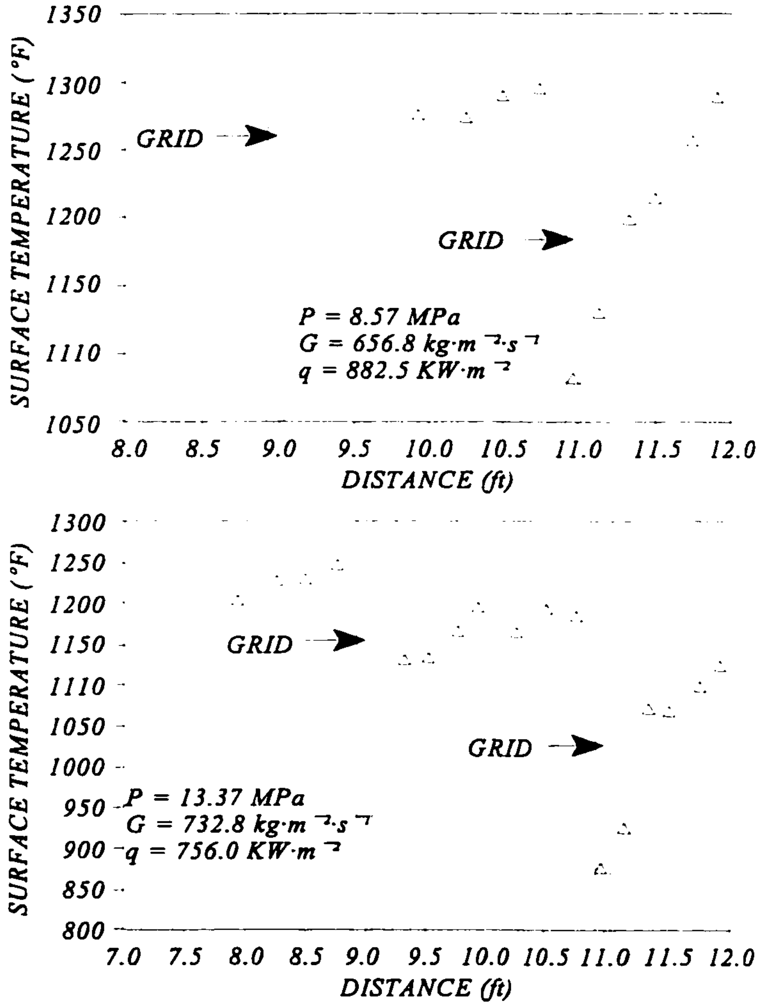

Figure 3.6. Effect of grid spacer on PDO temperature distribution in bundles (Yoder et al., 1982b)

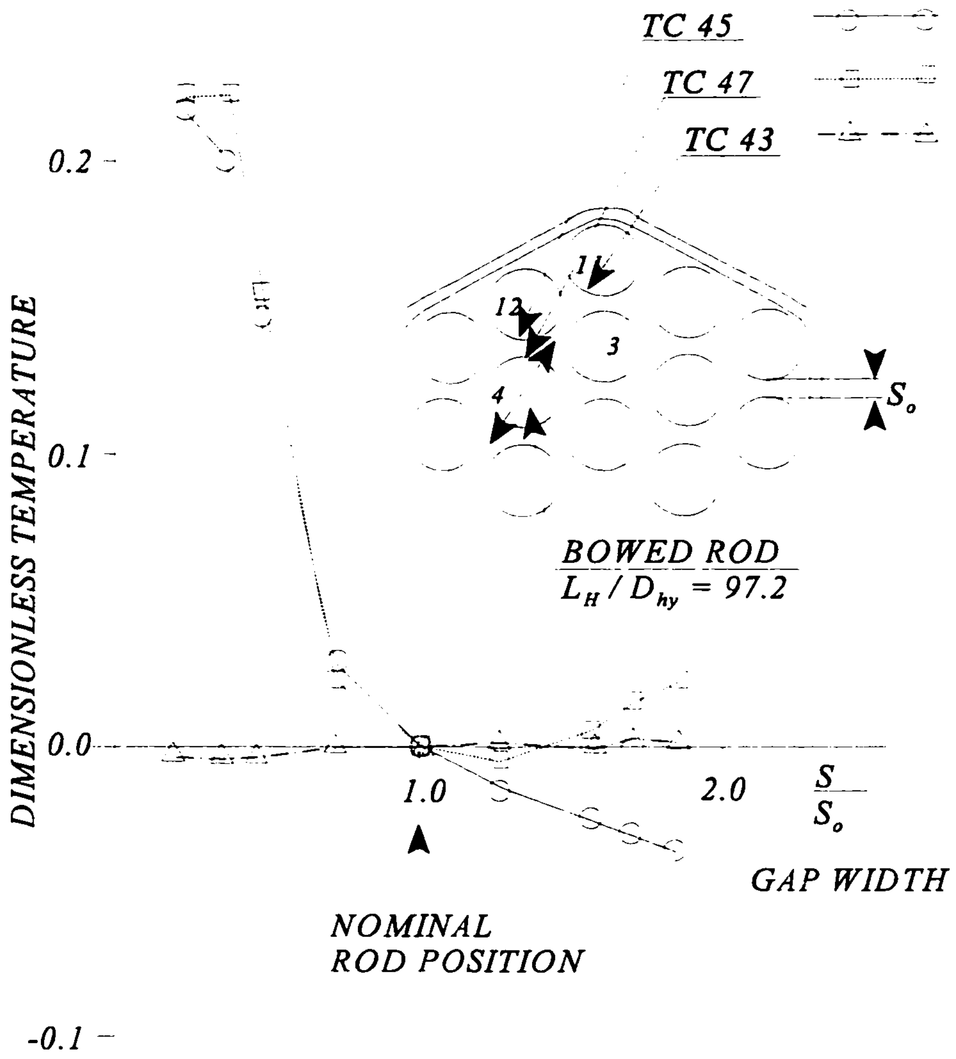

Figure 3.7. Azimuthal temperature distribution for different bowing positions (Möller and Tschöke, 1980)

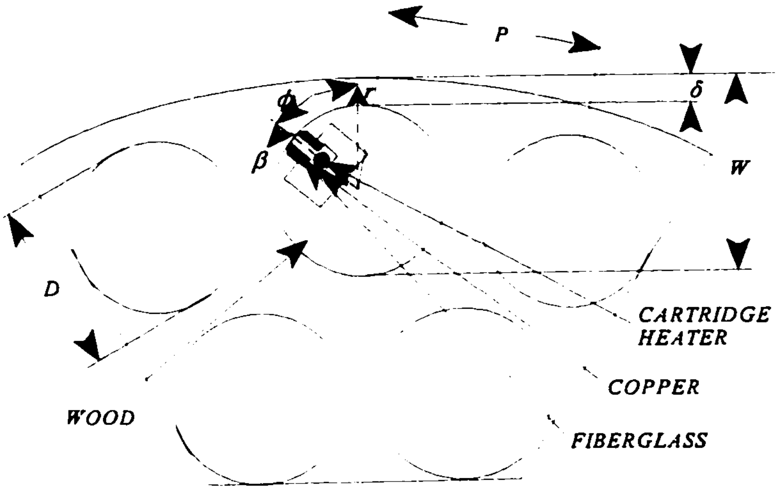

Figure 3.8. Test section setup of the Guellouz and Tavoularis study (1992)

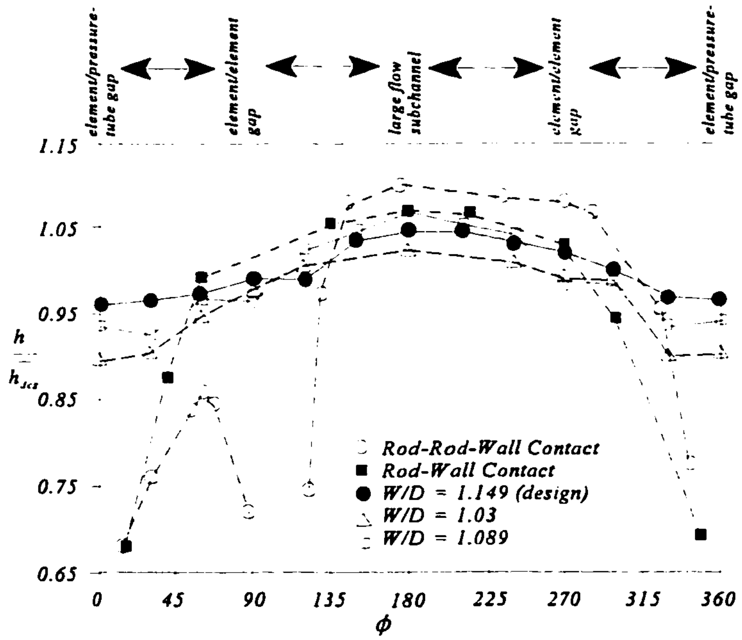

Figure 3.9. Ratio of heat transfer coefficients at various azimuthal locations (Guellouz and Tavoularis, 1992)

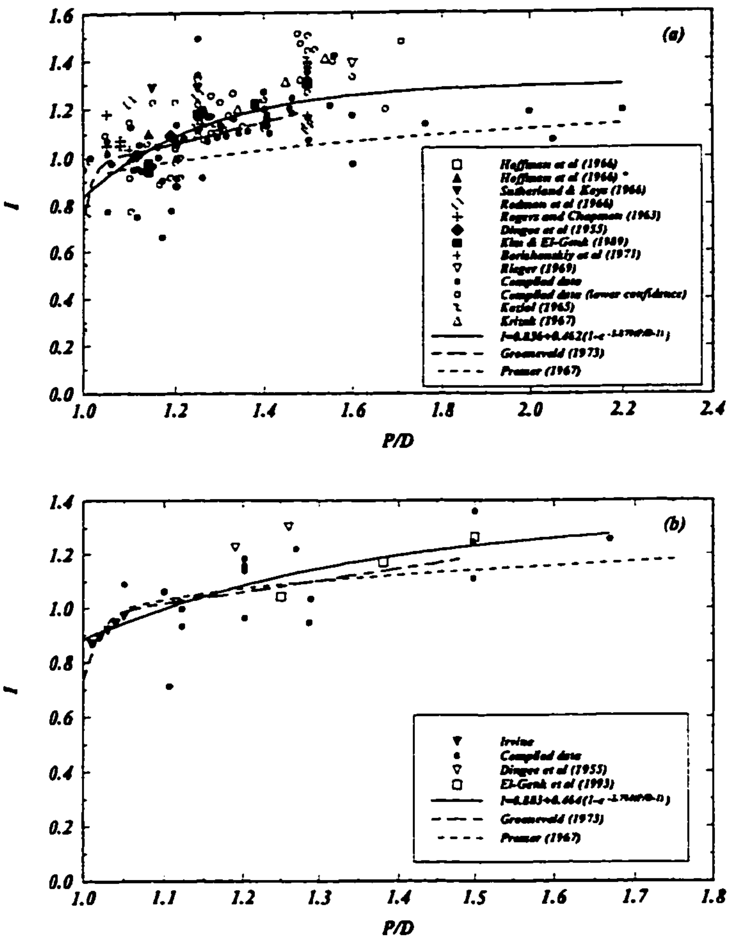

Figure 3.10. Variation of the I factor with the P/D ratio for triangular (a) and square (b) arrays (Guellouz and Tavoularis, 1995)

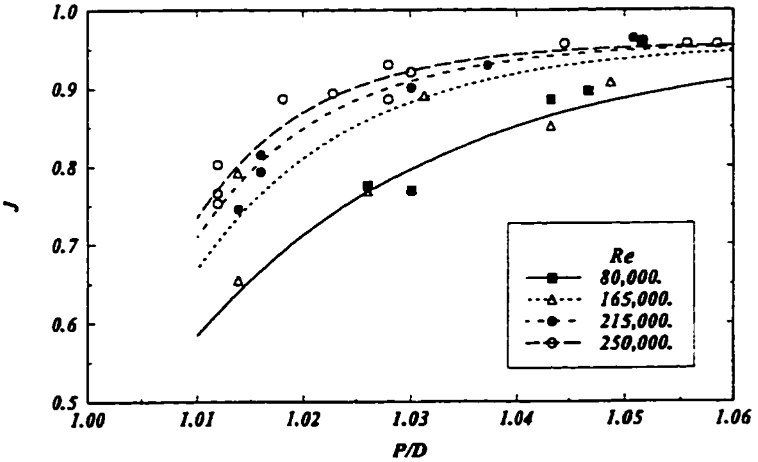

Figure 3.11. Variation of the J factor with the P/D ratio , based on Irvine's measurement (Groeneveld, 1973)

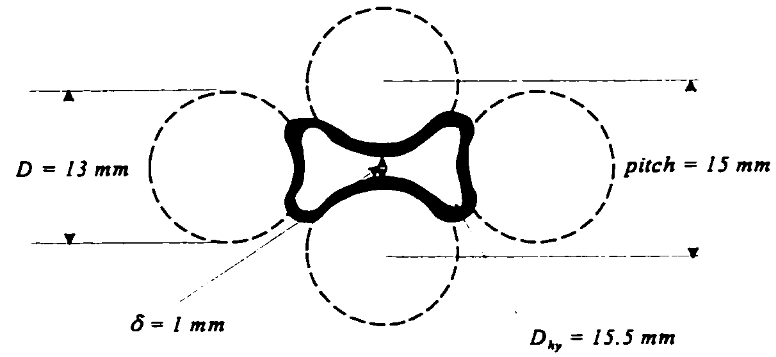

Figure 3.12. Dumbbell-shaped test section (Burdunin et al., 1987)

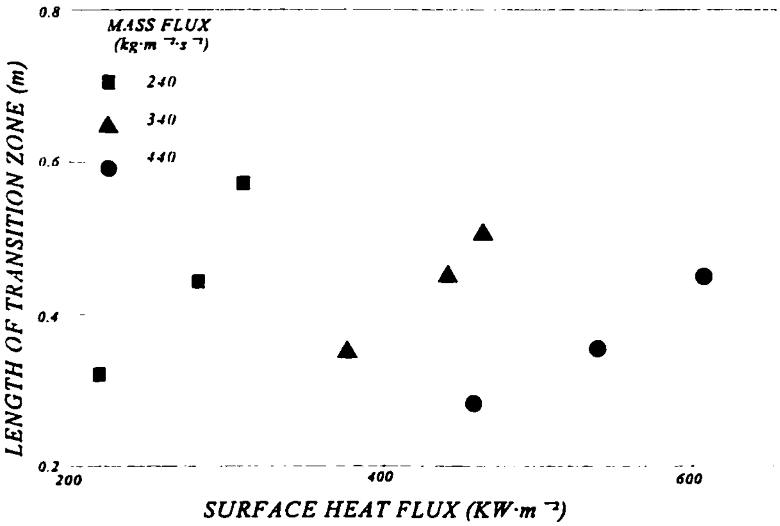

Figure 3.13. Length of transition zone from developing to fully developed flow (Burdunin et al., 1987)

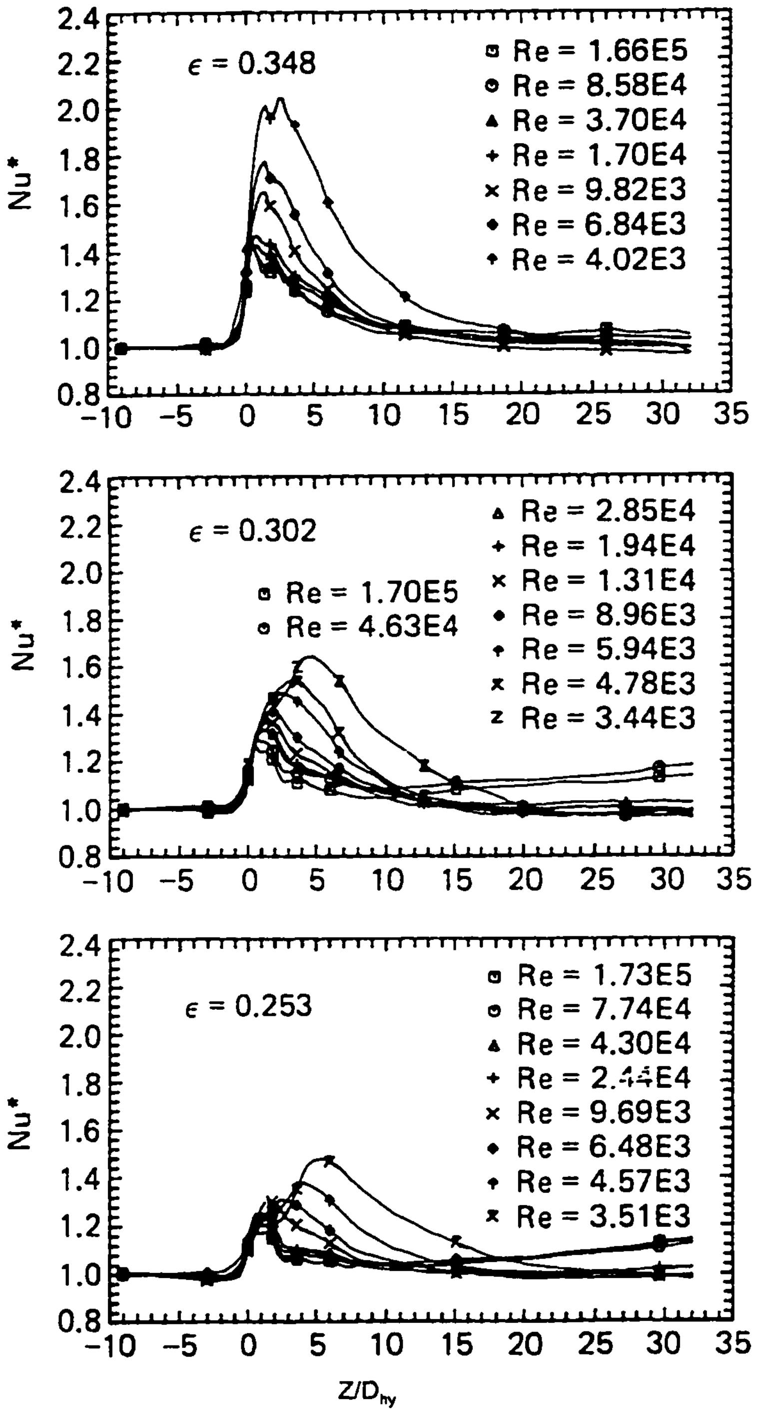

Figure 3.14. Axial distribution of Nu ratio of rough surface (Hassan and Rehme, 1981)

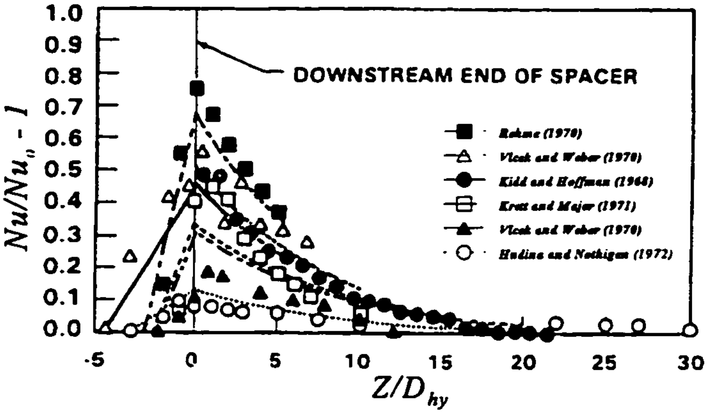

Figure 3.15. Heat transfer near spacers at single-phase flow (Yao et al., 1982)

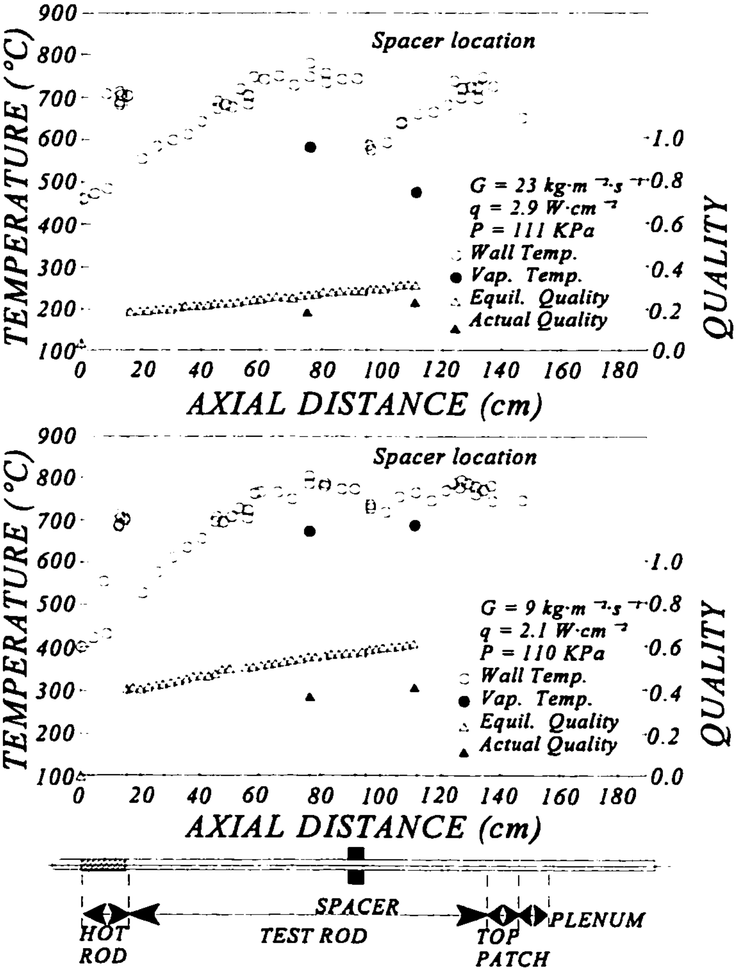

Figure 3.16. Effect of grid spacer on PDO temperature distribution in tubes (Unal et al., 1988)

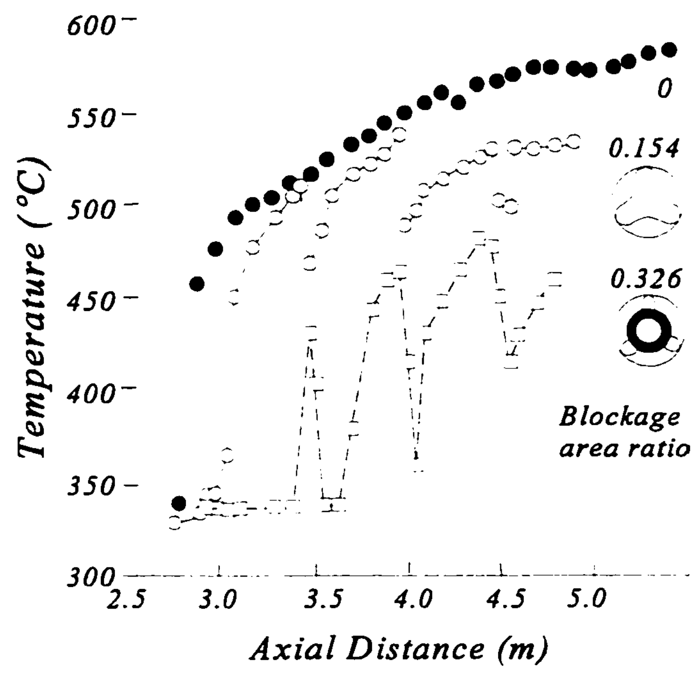

Figure 3.17. Temperature variation along the tube length (Sergeev et al., 1990)

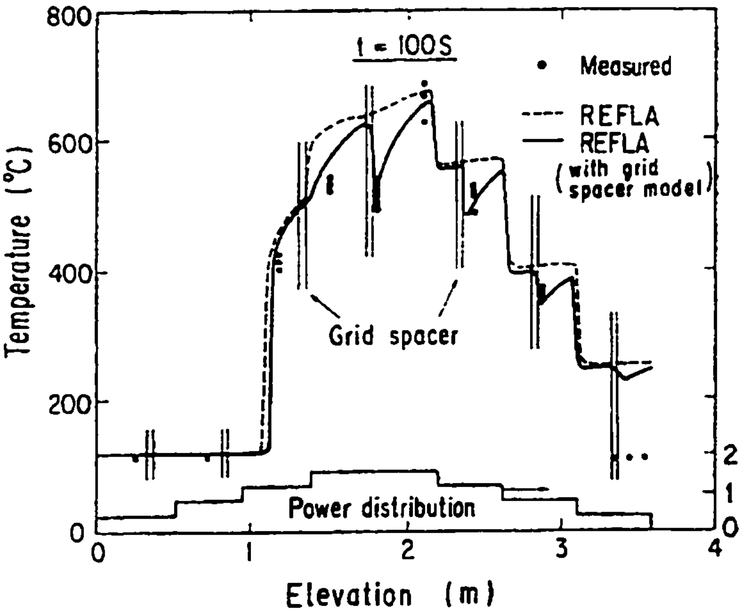

Figure 3.18. Comparison of calculated and measured axial temperature distribution (Sugimoto and Murao, 1984)

4. DEVELOPMENT OF CORRELATIONS FOR THE EFFECTS OF CROSS-SECTIONAL SHAPE AND SPACING DEVICES ON PDO HEAT TRANSFER

The literature review shows a strong effect of spacing devices but a relatively small effect of cross-sectional shape on single-phase and PDO heat transfer. However, most existing prediction methods are not applicable over a wide range of flow conditions and geometries. Therefore, a more generalized approach is used to develop appropriate prediction methods for these effects.

The present approach employs the tube-based correlation as the reference prediction method, and introduces modification factor for these effects. It provides a correct asymptotic trend for both channels with sharp corners and obstacles. Furthermore, there is ample data available for tubes and hence the uncertainty of the tube-based correlation is generally much smaller than that of other geometries.

4.1 Cross-Sectional Shape Effect

The following observations were made from the literature review of the effect of cross-sectional shape on PDO heat transfer:

- Only limited number of data are available for triangular-shaped, rectangular-shaped, dumbbell-shaped channels.
- A relatively large amount of data are available for annuli and bundles, but the shape effect is often coupled with other effects (e.g., gap size, surface curvature, etc.) and is difficult to be isolated.
- The Nusselt number is the largest for circular tubes and the smallest for triangular channels.
- A further reduction in the heat transfer coefficient is observed for channels with sharp

corners or narrow gaps, and

- A separate correlation is proposed for a specific channel shape and cannot be inter-related.

The channel-shape effect on PDO heat transfer is commonly applied to bundle analyses, in either the cross-sectional average or subchannel approach. In general, there is no sharp corners in a normal bundle geometry. Therefore, the proposed correlation has to be valid for channels with rounded corners. Under abnormal conditions, however, sharp corners can be encountered in a bundle and the corner effect must also be covered with the proposed correlation. Figure 4.1 shows a schematic diagram of elements in normal and abnormal bundles (e.g., bowing of an element towards other neighboring elements or swelling of an element).

The following modification factor for shape effect is proposed

$$K_{shape} = \frac{Nu_{non-tube}}{Nu_{tube}} = Minimum(K_{channel}, K_{gap}) \qquad \textbf{(4-1)}$$

where $Nu_{non\text{-}tube}$ and Nu_{tube} are Nusselt numbers for the channel of interest and tube, respectively. At the same local flow conditions, the $K_{channel}$ and K_{gap} are modification factors for the channel effect and gap effect, respectively. The Guellouz and Tavoularis correlation (1995) was developed with a relatively large data base and has been shown to be the most appropriate for the gap effect. It is expressed as

$$K_{gap} = 0.267 + 0.280\,[1 - e^{-250.94(P/D - 1)}] + 0.471\,[1 - e^{-9.65(P/D - 1)}] \qquad (1.0 \leq P/D \leq 1.5) \qquad \textbf{(4-2)}$$

This equation provides the modification to the minimum heat transfer coefficient because it was derived with surface-temperature data obtained at the narrow-gap region of the channels.

A geometry-based correlation is developed for the channel effect, $K_{channel}$, and is expressed as

$$K_{channel} = \left(\frac{L_1}{L_3}\right)^{0.356}\left(\frac{D_{he}}{D_{hy}}\right)^{0.071}\left(\frac{L_2}{L_1}\right)^{0.287} \qquad \textbf{(4-3)}$$

where L_1 is the minimum distance (in meters) from the centroid to any side, L_2 is the maximum distance (in meters) from the centroid to any side, L_3 is the maximum distance (in meters) from the centroid to any apex, D_{he} is the equivalent heated diameter in meters, and D_{hy} is the equivalent hydraulic diameter in meters. Figure 4.2 illustrated the definitions of various distances in both rectangular and triangular channels. For a uniformly heated tube, Equation (4-3) becomes 1.The exponent values in Equation (4-3) were optimized with triangular-channel data of Altemani and Sparrow (1980), Eckert and Irvine (1960) and Usui et al. (1982), and rectangular-channel of Novotny et al. (1964) and Sparrow et al. (1966). These data were obtained at the heated surface away from the corners and hence represent the average heat transfer values. A further reduction of heat transfer rate is anticipated at the corners where the flow velocity is low.

The channel-effect correlation is assessed with the same data base. Table 4.1 presents the prediction accuracy for each set of data. Although a large scatter among these data is observed, the overall agreement between predictions and data is relatively good. The overall average prediction error is 0.36% and root-mean-square (RMS) error is 10.83% for 92 data points. The average error is defined as

$$Average\ Error = \frac{1}{N}\sum_{i=1}^{n}(Error)_i \qquad \textbf{(4-4)}$$

and the RMS error is

$$RMS\ Error = \sqrt{\frac{1}{N}\sum_{i=1}^{n}(Error)_i^2} \qquad \textbf{(4-5)}$$

where

$$Error = \frac{Pred.Nu - Exp.Nu}{Exp.Nu} \qquad \textbf{(4-6)}$$

Figures 4.3 to 4.5 show separately the comparisons between predictions of the correlation for the channel-shape effect and experiment data of the triangular-shaped channels, while figures 4.6 to 4.9 are for rectangular-shaped channels. As indicated above, the agreement between data and predictions is good for the triangular-shaped channels. A good agreement is also observed between predictions and data of the rectangular-shaped channel having an aspect ratio of 1. However, the correlation tends to underpredict the measurements of Novotny et al. (1964) but overpredict those of Sparrow et al. (1966) in rectangular-shaped channels of small aspect ratios (0.1 and 0.2).

The proposed correlation for the shape effect is anticipated to be valid at high quality PDO conditions with thermodynamic quality approaching or greater than 1. At low qualities with high droplet concentration in the core, the droplet impingement rate is expected to be high at the low velocity region of the corners for both rectangular and triangular channels. The use of this correlation may result in an underprediction of the heat transfer coefficient. This has to be confirmed with experiment data.

4.2 Effect of Spacing Devices

The following observations were made from the literature review of the effect of spacing devices on PDO heat transfer:

- Steam desuperheating downstream of the grid, because of a high intensity of turbulence near the spacer that produces intensive mixing of liquid droplets with the superheated steam, and hence the heat transfer is improved.
- High turbulence near the spacer that increases the rate of liquid droplet impact and breakup with the spacer grid, causing an increase in the interfacial heat transfer area, and an improved interfacial heat transfer.
- Reduction in the flow area resulting in an increase in coolant velocity. This improves the convective heat transfer in the vicinity of the spacer grid (including a short region upstream of the spacer).

- A "fin" effect where heat is lost to the coolant by conduction through the spacer grid at its area of contact with the hot wall.
- Increased absorption of radiant heat from the hot wall, although this effect tends to be small.
- Reduction in enthalpy and flow imbalances between rod bundle subchannels in the plane of the grid spacer, because of improved inter-subchannel mixing caused by high transverse turbulence intensities.
- Existing correlations are valid for specific types of spacing devices and flow conditions and cannot be extended to other types or conditions.

A generalized correlation is developed for the effect of spacing devices on PDO heat transfer. Similar to the approach used in developing the shape-effect correlation, it is based on a modification factor to the reference geometry (i.e., tubes), which is expressed as

$$K_{spacer} = \frac{Nu_{spacer}}{Nu_{no\ spacer}} \tag{4-7}$$

where Nu_{spacer} and $Nu_{no\ spacer}$ are Nusselt numbers in a channel with and without spacers, respectively, at the same local flow conditions.

In single-phase flow, the spacer enhancement effect mostly depends on Z/D_{hy} or blockage-area ratio. Downstream of the spacer, the heat transfer enhancement decays sharply and is relatively short-lived. Yao et al. (1982) correlation predicts the above-mentioned trends well. This can be shown in Figure 3.15. Normally, this effect will be disappeared with Z/D_{hy} of 20 to 40.

In post-dryout heat transfer, due to the vapor superheating, the non-equilibrium in vapor enthalpy has to be considered. At the dryout location the vapor is at saturation and the amount of heat transferred to droplet is small. Further downstream the vapor superheat becomes large because of higher wall temperatures transferring heat to the vapor which in turn is cooled by the evaporating droplets. Poor interfacial heat transfer (such as at low flows) inhibits evaporation and results in high vapor superheats. The Groeneveld-Delorme (1976) correlation clearly explained this phenomenon. The vapor superheat can be expressed as the difference between T_g and T_{sat}, i.e.

$$\frac{H_{va}-H_{ve}}{H_{fg}}=\frac{Cp_g(T_g-T_{sat})}{H_{fg}}=f(G,x,Z/D_{hy},\ldots) \qquad \textbf{(4-8)}$$

Based on Groeneveld-Delorme (1976) correlation, the vapor desuperheating effect which depends on amount of liquid present in the flow and by the flow obstruction can be expressed as

$$C\frac{(H_{va}-H_{ve})}{H_{fg}}=f(K_{ob},Z/D_{hy},G,x,\ldots) \qquad \textbf{(4-9)}$$

where C is the desuperheating factor varies from 0 to 1. When C equals to 0, there is no superheat effect which corresponds to the single-phase flow. When C equals to 1, that is in two-phase flow condition but with no desuperheating effect, i.e., with no flow obstruction. C is normally less than 1 for any flow obstruction inside the flow channel. The degree of desuperheating effect depends on the flow obstruction and Z/D_{hy}, as well as mass flux and quality. C is lower for a large K_{ob} or G and small Z/D_{hy}.

The vapor superheat is reduced by increasing the turbulence in the flow e.g., downstream of the spacer, old boundary layer is destroyed and the new one is established. Due to the high turbulence produced by the spacer, the droplets break up and increase the interfacial surface area. It absorbs the heat from the vapor and therefore the superheat decreases. It has an accumulative effect on improving the heat transfer until the droplets start to coalesce again. The increased turbulence intensity is decaying continuously. Comparing with single-phase short-lived decay effect, the two-phase flow desuperheating effect is a relatively long-lived one.

Based on the approaches employed by Yao et al. (1980) and Kim and Korol'Kov (1991), the following correlation for the spacer effect is derived:

$$K_{spacer} = 1 + \left(0.47 + 4.81\,x_e(1 - x_e)^{0.105}\right) K_{ob} \exp\left(-0.13 \frac{Z}{D_{hy}} \right) \qquad \textbf{(4-10)}$$

where x_e is the equilibrium quality, Z is the distance downstream of the spacer (or flow blockage) in meters, D_{hy} is the hydraulic diameter of the free-flow area in meters and K_{ob} is the single-phase loss coefficient. The constants in this correlation are optimized with the single-phase (air-flow) data of Rehme (1977), Vleck and Weber (1970), Kidd and Hoffman (1968), Krett and Majer (1971) and Hudina and Nothigen (1972) as well as the PDO data of Sergeev et al. (1990). Other data listed in the literature review are not applicable because the spacer effect is coupled with other effects. For example: rewetting of the heated surface is observed at locations just downstream of the spacers in the data of Kim and Korol'Kov and hence both the spacer and the flow-development effects are significant. Although the correlation provides a correct asymptotic trend for equilibrium qualities approaching 0 (single-phase liquid flow is assumed and $Nu_{no\ spacer}$ is calculated with liquid properties), there are no data available to verify the trend at qualities lower than 0.9.

The single-phase loss coefficients for the spacers of interest were not presented in various studies. They were calculated with the Leung and Hotte equation (1997) that provides single-phase loss coefficients for obstructions installed at four different cross-sectional locations inside a tube (figure 4.10). The loss coefficient is calculated with

$$K_{ob} = a_1 \left(\tan\left(\left(\frac{A_{ob}}{A_f} \right)^2 \frac{\pi}{2} \right) \right)^{b_1} \qquad \textbf{(4-11)}$$

The constants a_1 and b_1 were optimized with single-phase data of Salcudean and Leung (1988), and are shown in Table 4.2 for various blockage locations. Their data showed a relatively strong effect of blockage location on pressure drop. Based on the configurations of the spacer, the constants for the central-segment obstruction is used in this study.

Strictly speaking, the vapor-weight quality (or mass quality) is more appropriate than the equilibrium quality for use as the correlating parameter. Due to the complex calculations and lack of experimental data for the vapor-weight quality, the equilibrium quality is used as a simplification. It is anticipated that the decay function (i.e., the exponential term) may also be affected by the single-phase loss coefficient. The recovery length downstream of the spacing device should be longer for a larger blockage. Furthermore, the magnitude of the enhancement is probably influenced by the mass flow rate (a high mass flow rate reduces the vapor superheat and hence increases the level of enhancement. But it does not allow for vapor desuperheating as there is little superheat at high flow conditions). These phenomena cannot be verified due to the lack of experimental data.

The proposed correlation is more generalized than that of Yao et al. (1982) because it includes the single-phase loss coefficient that can take into the consideration of the effects of blockage shape and location on turbulence generation (hence heat transfer enhancement). Yao et al. (1982) employed the blockage-area ratio as the parameter, which is valid for a specific type of spacing device only. In addition, the proposed correlation provides a correct asymptotic trend as the equilibrium quality approaches 1 (it predicts an enhancement of single-phase heat transfer coefficient). The Kim and Korol'Kov equation (1991), on the other hand, predicts no enhancement effect when the equilibrium quality becomes 1.

The spacer-effect correlation is assessed with the data base listed in Table 4.3 which presents the prediction accuracy for each set of data. Although a large scatter among these data is observed, the overall agreement between predictions and data is relatively good. The overall average prediction error is 1.01% and root-mean-square (RMS) error is 4.71% for 42 data points of single-phase air flow, and -5.35% and 20.05%, respectively, for 17 data points of PDO steam-water flow (Sergeev et al. 1990).

Figures 4.11 to 4.16 show the comparison between predictions of the spacer-effect correlation and experimental data. A good agreement is observed for the large-blockage data of Rehme (1977). The Nusselt numbers in other data sets are either overpredicted or underpredicted systematically.

However, the differences are relatively small.

Figures 4.17 to 4.18 show the comparison between predictions and PDO data of Sergeev et al. (1990), which were obtained with two types of spacers. In the present study, only data of fully developed PDO flow are used to avoid the flow-developing effect. The sharp variation of Nusselt-number ratio is caused by the presence of spacers. The ratio is large at the spacer and decreases with increasing distance downstream of the spacer. The predictions follow closely the trend displayed in the figure for the spacer of small blockage-area ratio. A slightly larger deviation is observed for the large spacer. Nevertheless, the trend is also predicted closely.

4.3 Summary

The correlations for both the shape and the spacer effects on PDO heat transfer are derived with a limited set of data. Although a good agreement is generally shown between predictions and data, extrapolation to other geometries and flow conditions may be questionable. These correlations have to be validated with additional experimental data to ensure that their predictions remain valid at other conditions and geometries.

The data showed that the effect of channel shape on single-phase and PDO heat transfer is relatively small, and the tube-based correlation appears to provide reasonable predictions for other geometry. Therefore, this validation exercise focuses mainly on the effect of spacing devices on PDO heat transfer. An experiment has been set up to obtain PDO data in a tube equipped with a flow blockage. It is described in the next chapter, and is followed by the results of validation.

Table 4.1. Prediction accuracy of the correlation for the channel-shape effect

References	Channel shape	Heating conditions	No. of Data	Average error (%)	RMS error (%)
Altemani and Sparrow (1980)	Equilateral triangular	two sides	10	3.16	6.55
Eckert and Irvine (1960)	Isosceles triangular	all sides	14	-1.06	9.35
Usui et al. (1982)	Isosceles triangular	all sides	13	0.89	4.61
Triangular channel			37	0.77	7.22
Novotny et al. (1964) α=0.1	Rectangular	two long sides	9	-13	13.75
Novotny et al. (1964) α=0.2	Rectangular	two long sides	16	-4.25	6.13
Novotny et al. (1964) α=1	Rectangular	two long sides	16	-3.13	7.42
Sparrow et al. (1966) α=0.2	Rectangular	one long side	14	19.94	21.13
Rectangular Channel			55	0.08	12.69
Overall			92	0.38	10.35

Table 4.2. Constants in the loss-coefficient equation (Equation (4-9)) for various flow blockages (Leung and Hotte, 1997)

	Obstruction			
Constants	Central	Peripheral	Central segment	Peripheral segment
a_1	7.59	14.038	9.3797	11.859
b_1	0.9175	1.4748	1.088	1.2874

Table 4.3. Prediction accuracy of the correlation for the spacer effect

References	Blockage area ratio	Number of data points	Average error (%)	RMS error (%)
Rehme (1977)	0.348	6	-0.10	0.75
Vlcek and Weber (1970)	0.289	5	-5.23	5.54
Kidd and Hoffman (1968)	0.245	11	-4.23	5.28
Krett and Majer (1971)	0.303	8	6.57	7.33
Vlcek and Weber (1970)	0.237	6	5.84	6.05
Hudina and Nothigen (1972)	0.156	6	3.21	3.33
Subtotal for single-phase conditions		42	1.01	4.71
Sergeev et al. (1990)	0.154	9	5.77	11.88
Sergeev et al. (1990)	0.326	8	-16.46	28.22
Subtotal for two-phase conditions		17	-5.35	20.05
Total for all conditions		59	-0.58	8.55

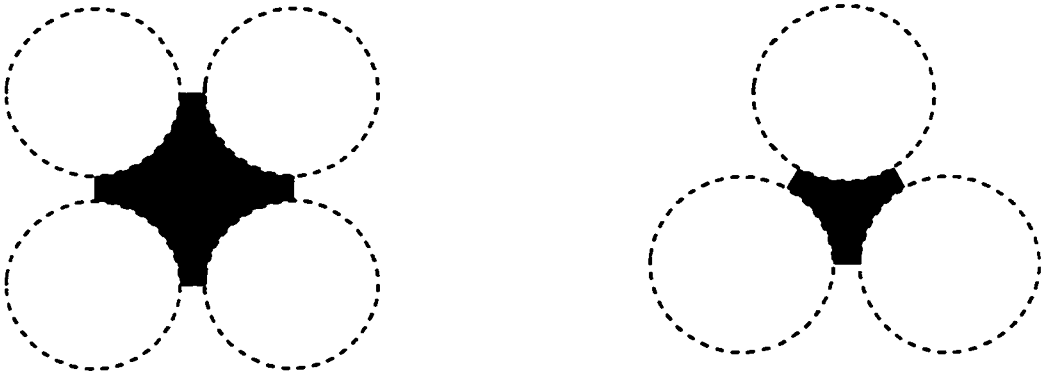

SQUARE SUBCHANNEL IN
AN INTACT BUNDLE

TRIANGULAR SUBCHANNEL
IN AN INTACT BUNDLE

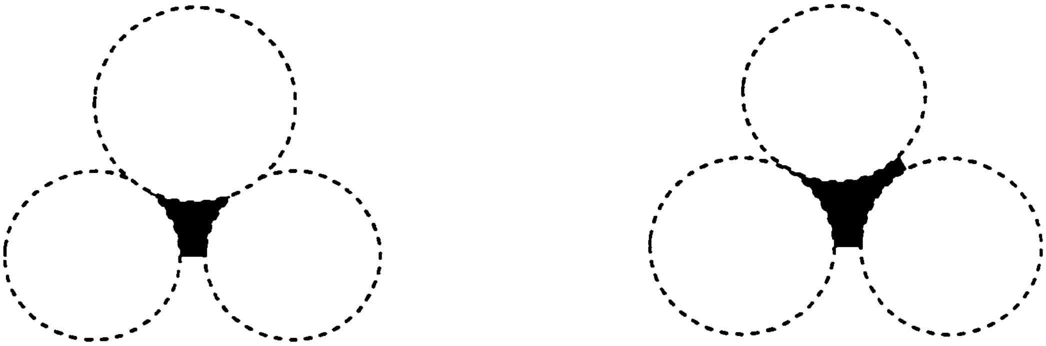

TRIANGULAR SUBCHANNEL IN A DISTORTED
BUNDLE WITH A SWELLED ELEMENT

TRIANGULAR SUBCHANNEL IN A DISTORTED
BUNDLE WITH A BOWED ELEMENT

Figure 4.1. Subchannel configurations of intact and distorted bundles

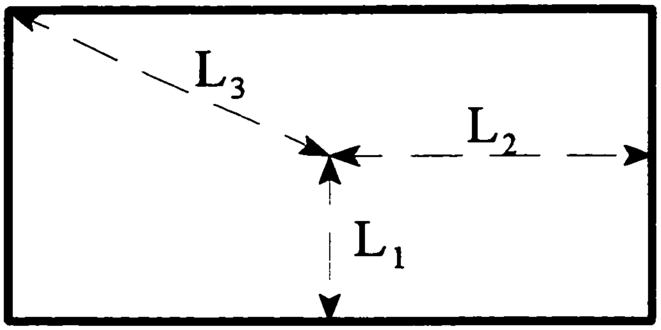

Rectangular channel

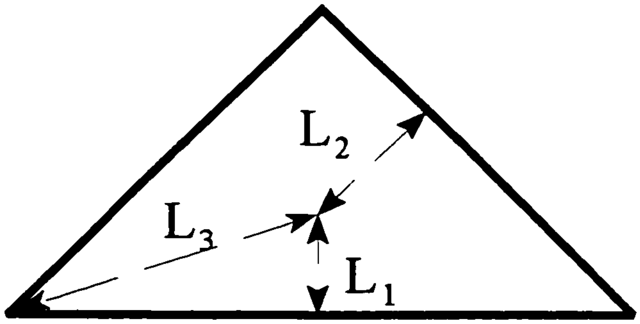

Triangular channel

Figure 4.2. Definitions of various distance in rectangular and triangular channels

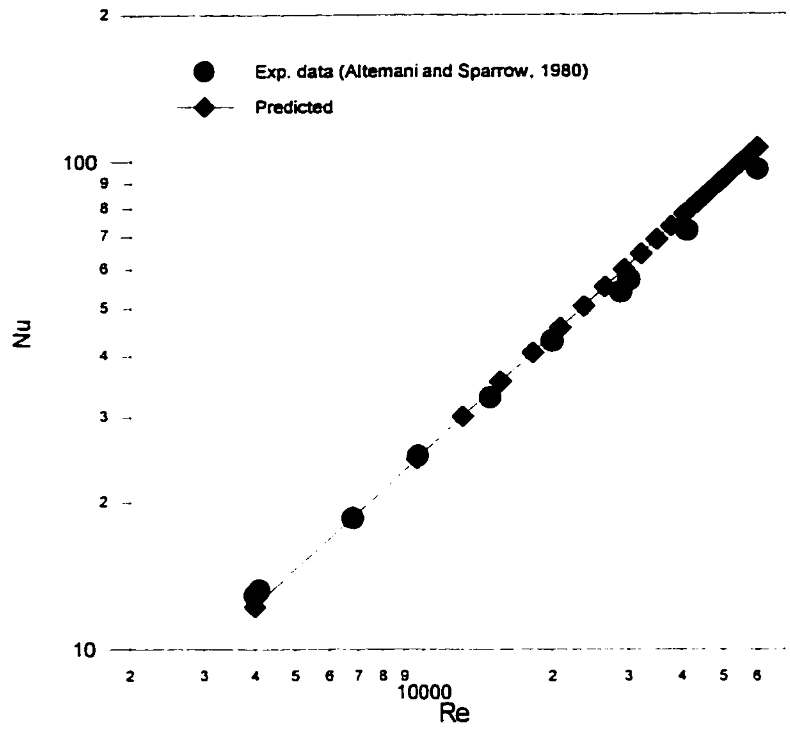

Figure 4.3. Comparison of Nu between prediction and triangular data of Altemani and Sparrow (1980)

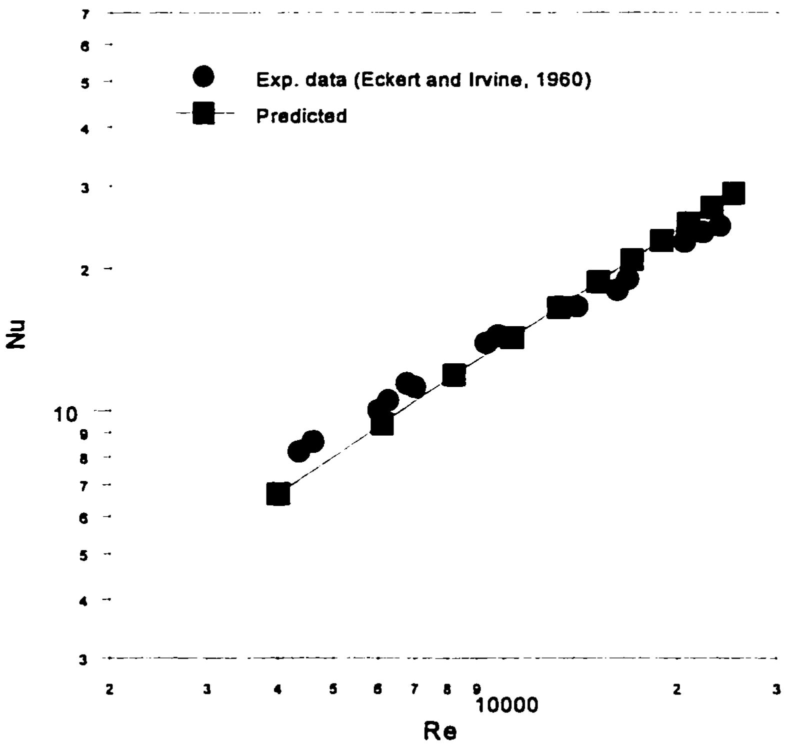

Figure 4.4. Comparison of Nu between prediction and triangular data of Eckert and Irvine (1960)

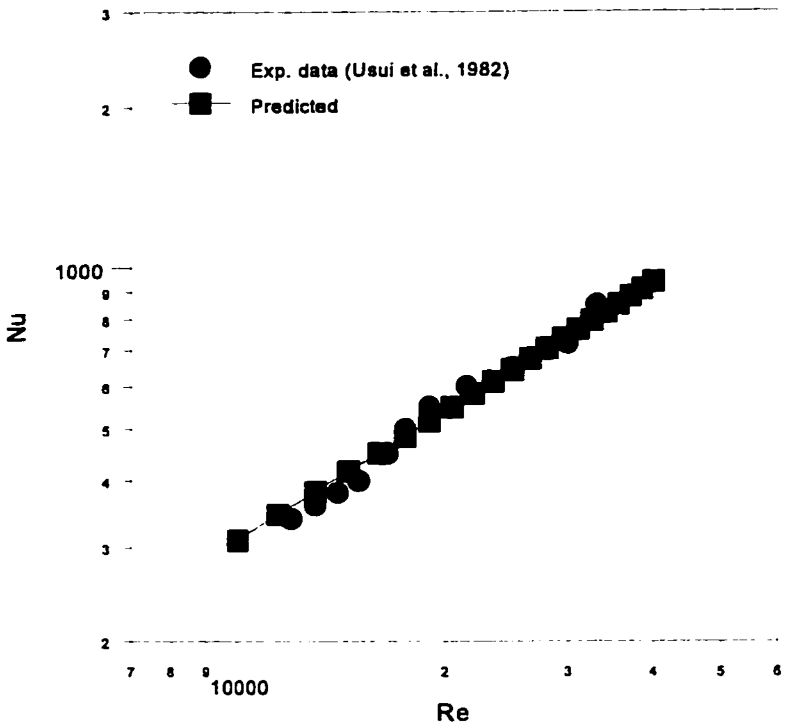

Figure 4.5. Comparison of Nu between prediction and triangular data of Usui et al. (1982)

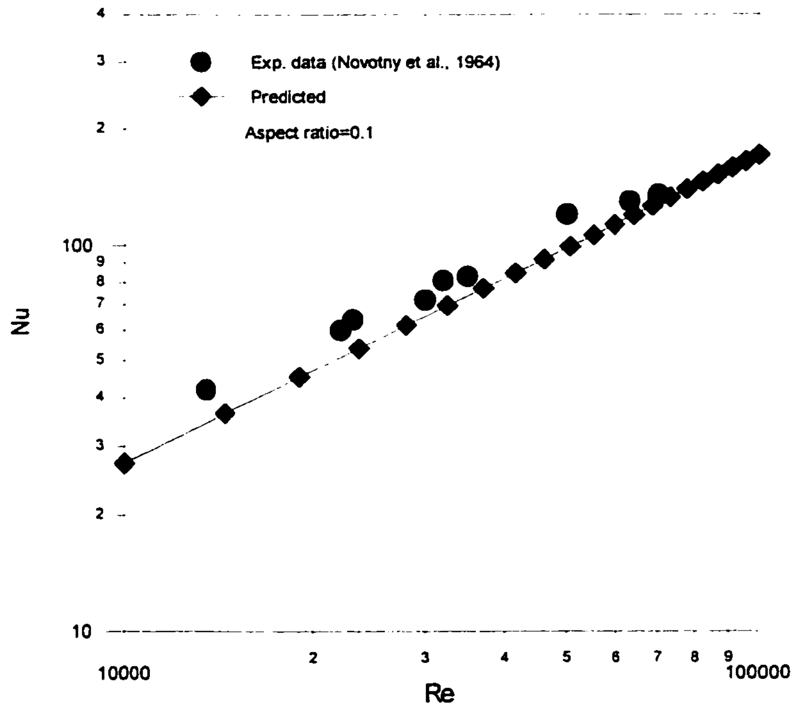

Figure 4.6. Comparison of Nu between prediction and rectangular data of Novotny et al. (1964) at aspect ratio of 0.1

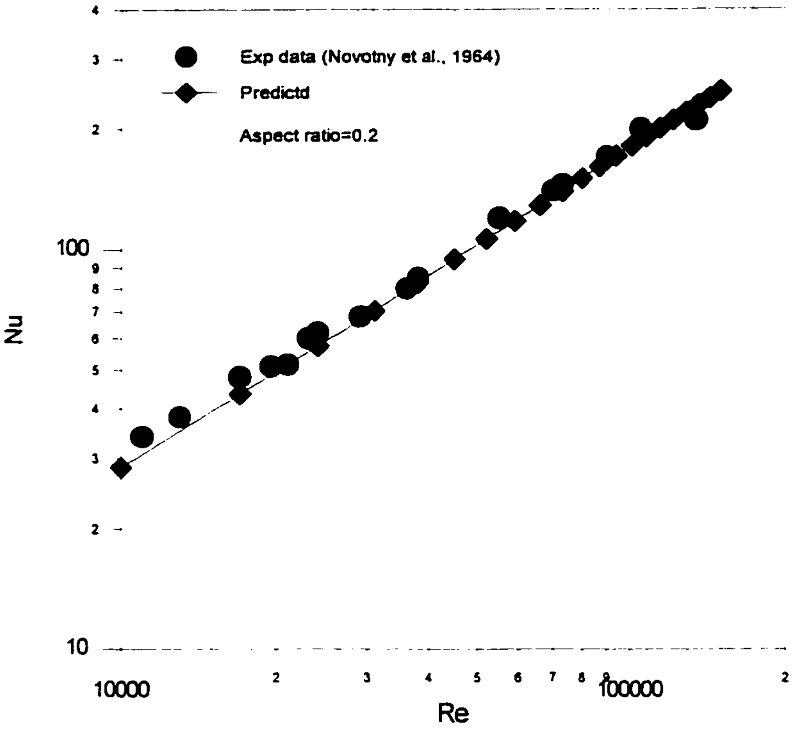

Figure 4.7. Comparison of Nu between prediction and rectangular data of Novotny et al. (1964) at aspect ratio of 0.2

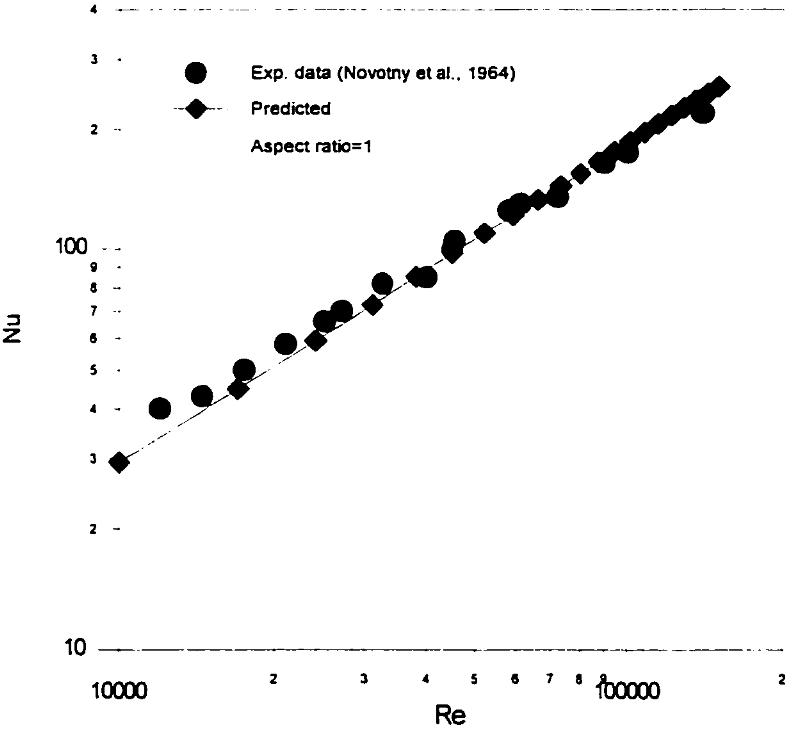

Figure 4.8. Comparison of Nu between prediction and rectangular data of Novotny et al. (1964) at aspect ratio of 1

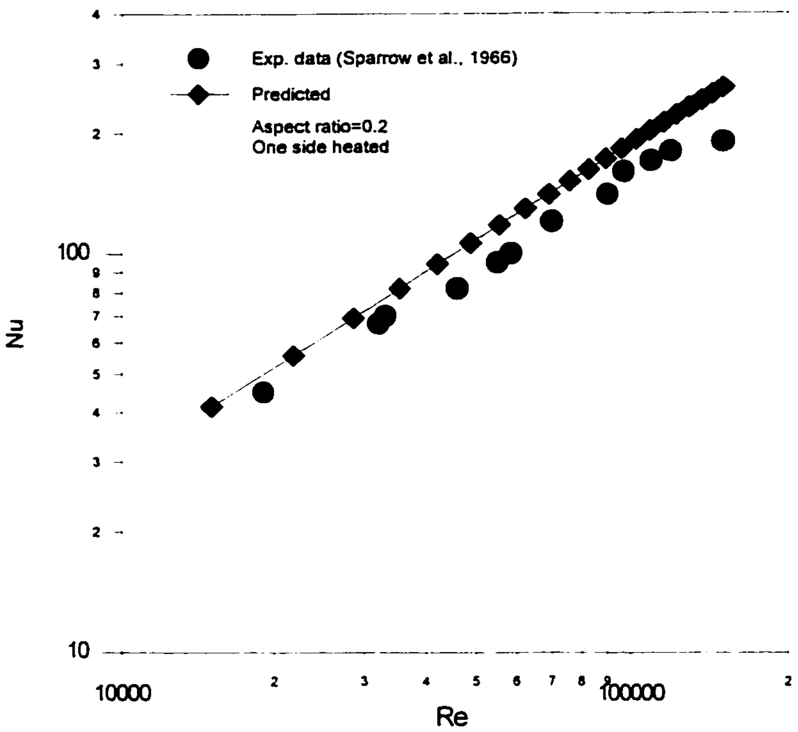

Figure 4.9. Comparison of Nu between prediction and rectangular data of Sparrow et al. (1966) as aspect ratio of 0.2

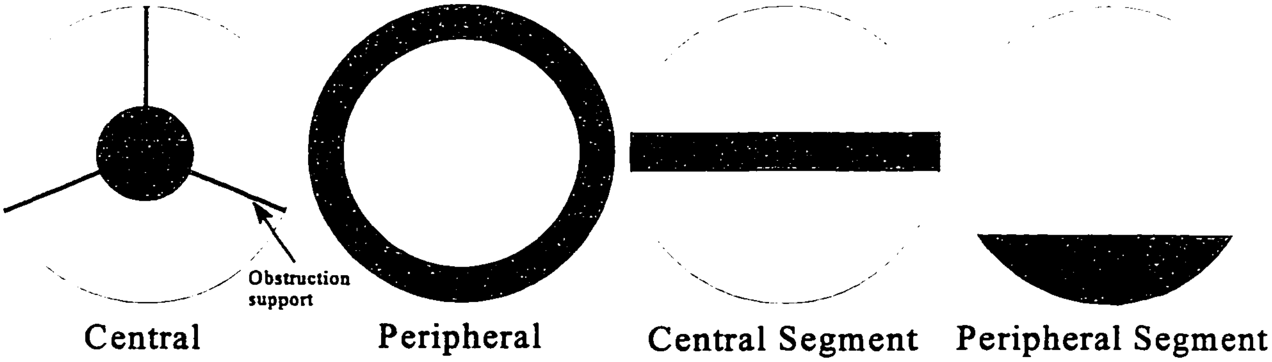

Figure 4.10. Types of obstruction tested by Salcudean and Leung (1988)

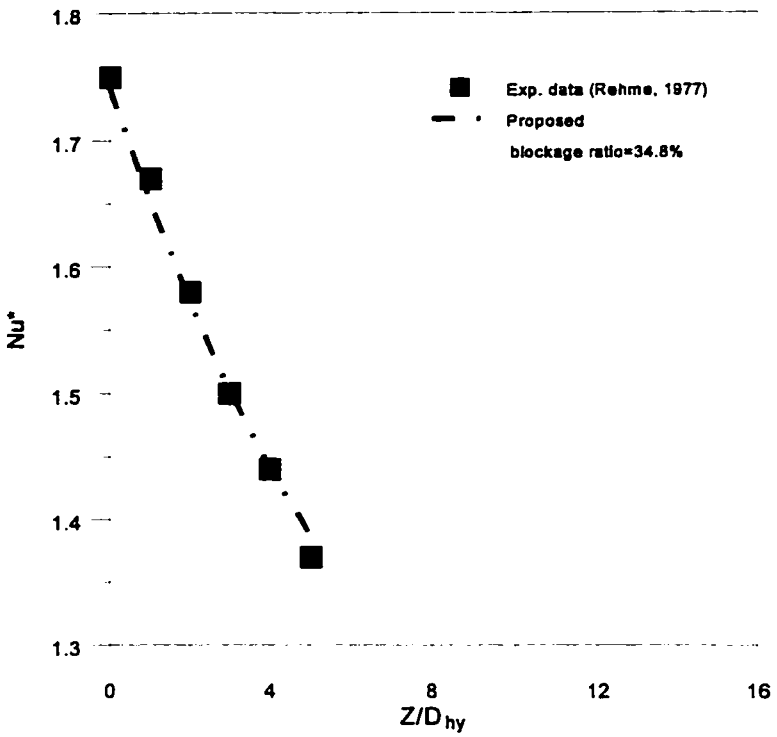

Figure 4.11. Comparison between the proposed correlation with experiment data of Rehme (1977)

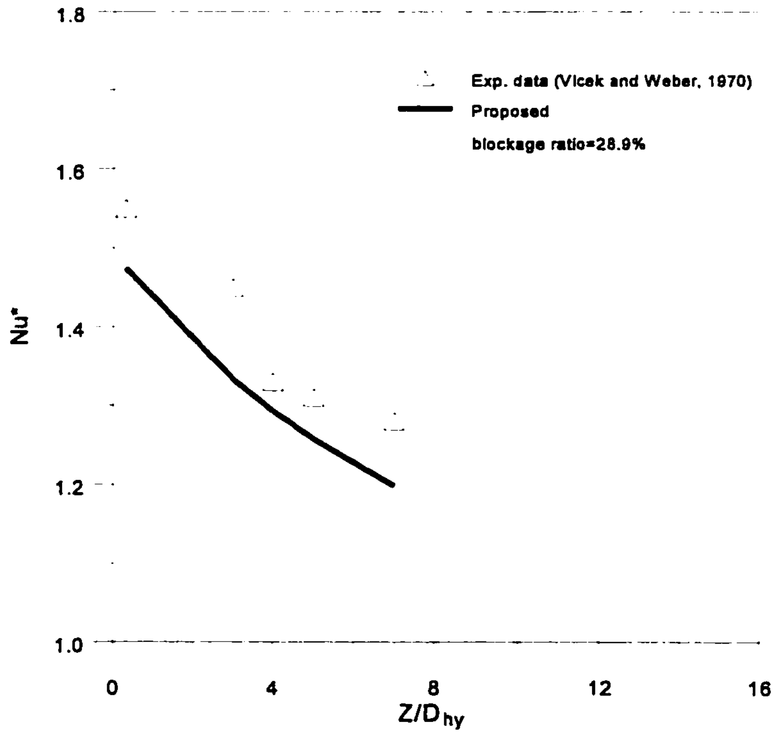

Figure 4.12. Comparison between the proposed correlation with experiment data of Vlcek and Weber (1970)

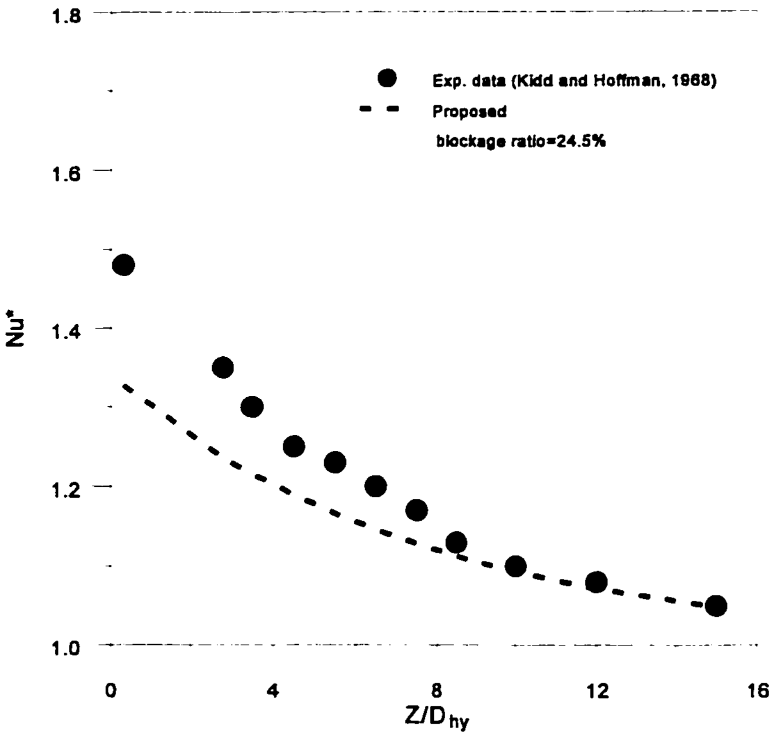

Figure 4.13. Comparison between the proposed correlation with experiment data of Kidd and Hoffman (1968)

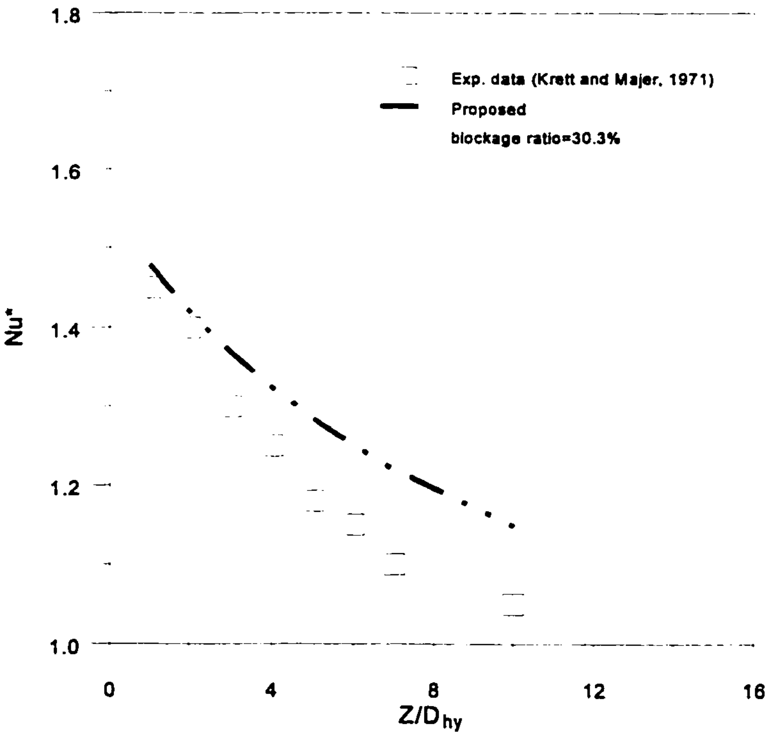

Figure 4.14. Comparison between the proposed correlation with experiment data of Krett and Majer (1971)

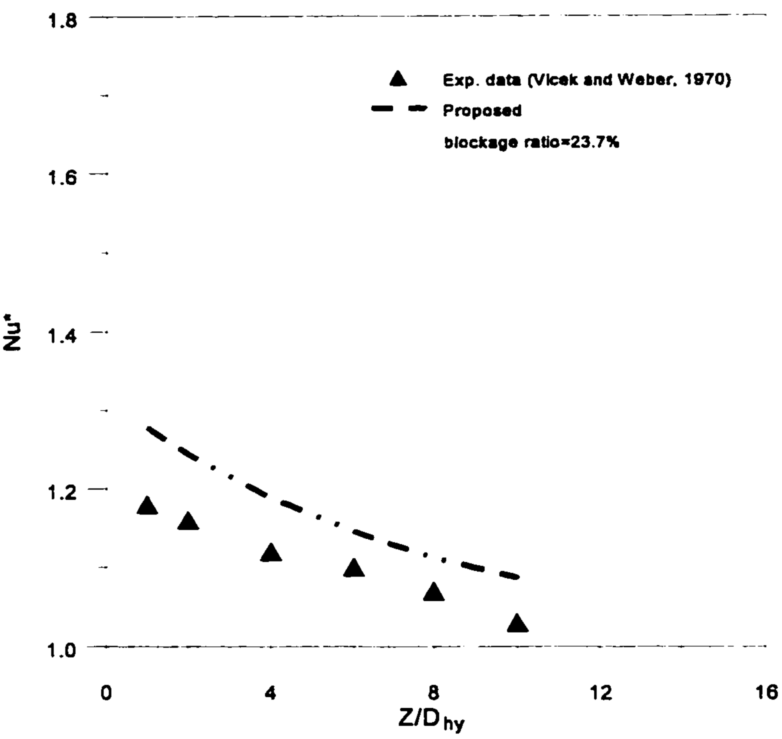

Figure 4.15. Comparison between the proposed correlation with experiment data of Vlcek and Weber (1970)

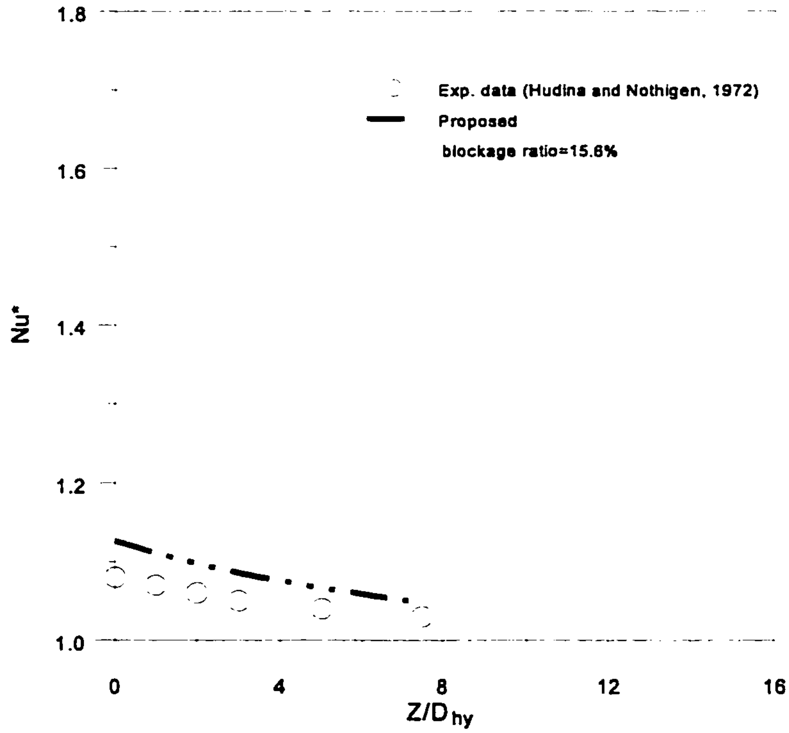

Figure 4.16. Comparison between the proposed correlation with experiment data of Hudina and Nothigen (1972)

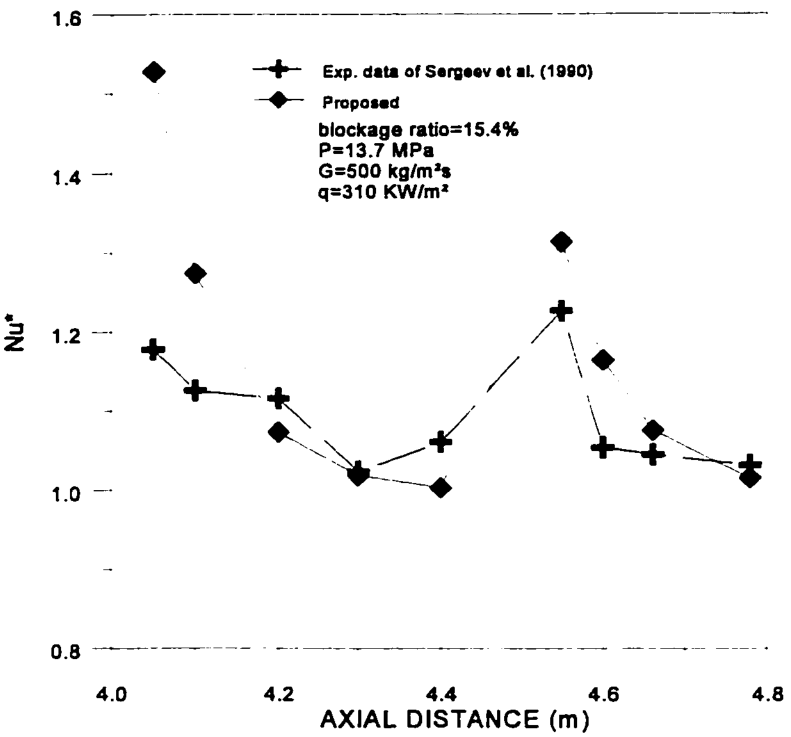

Figure 4.17. Comparison of the proposed correlation with Sergeev et al. (1990) data for ϵ=0.154

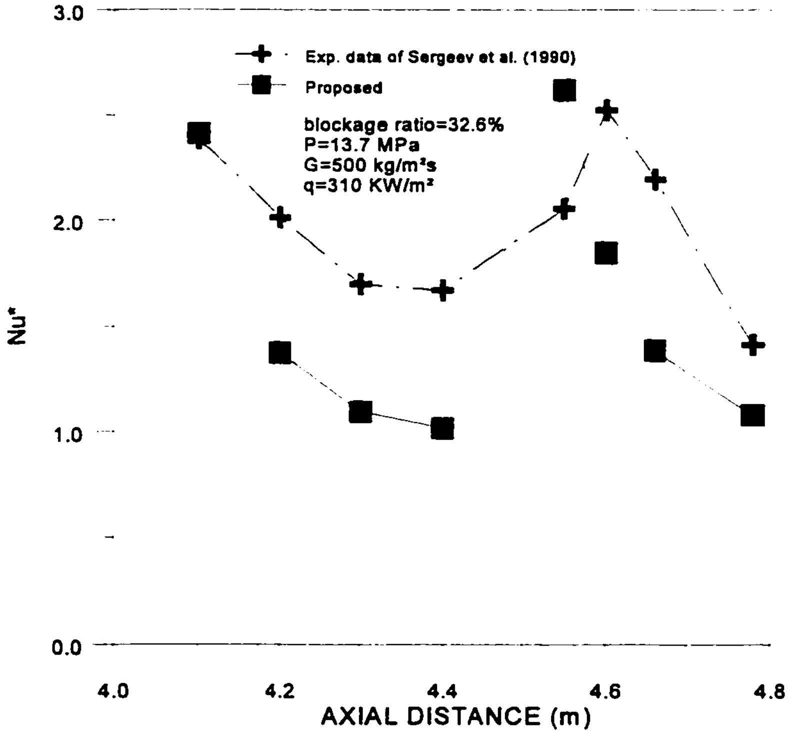

Figure 4.18. Comparison of the proposed correlation with Sergeev et al. (1990) data for ϵ=0.326

5. EXPERIMENTAL STUDY OF THE EFFECT OF A FLOW BLOCKAGE ON PDO HEAT TRANSFER

Experimental data are needed to validate the proposed correlation for predicting the effect of spacing devices on PDO heat transfer. Previous experimental studies on the same effect were mostly carried out in either annuli or bundles. Although they related closely to the geometry of interest in real applications, these experimental data included also the geometry effect (particularly the gap effect) in addition to the spacer effect. To eliminate other effects, a simple tube is used as the test section in the present experiment. A flow blockage is installed at various locations to examine the enhancement effect on PDO heat transfer.

5.1 Experiment Loop

The test was conducted in the multi-fluid loop at University of Ottawa. Figure 5.1 shows schematically the set up of the loop which consists of gear pumps, flow meter, preheater, test section, heat exchanger and pressurizer, etc. Coolant leaving the pump passes through the flow meter and a preheater. A valve is used to adjust the flow rate. The fluid temperature at the inlet of the test section is controlled by adjusting the power to the preheater. The coolant passes through the test section and extracts heat in the process. The absorbed heat is then released to the water in the secondary side of the heat exchanger. Leaving the heat exchanger, the coolant is circulated through the loop. The fluid temperature at the inlet and the system pressure at the outlet of the test section are measured. In the present experiment, the coolant is Freon-134a.

5.2 Test Section and Test Conditions

The test section is constructed with an Inconel-600 tube of 4.1 mm inside diameter. Two power clamps are connected to the inlet and outlet ends of the test section, providing an overall heated length of 100 cm. Eight Chromel-Alumel (K-type) thermocouples were attached to the outside of the test section at locations from 72 cm to the end of the heated length. Seven of these thermocouples are spring loaded and the last one is attached directly at the outlet. Figure 5.2 shows schematically the test section and the locations of the thermocouples.

Three types of flow obstruction with a blockage-area ratio (i.e., blockage-area/free-flow-area) of 37.8% are tested in the experiment. They are made of carbon steel and are shaped into either a ring, cube or hex. Figure 5.3 shows the configurations and dimensions of these flow obstructions. The blockage is held in the location with two magnets; this allows the variation of blockage location when the power is on.

The following flow conditions are tested in the present experiment:

Pressure: 1.13 MPa (equivalent pressure of 7 MPa for water flow)
Mass flow rate: 0.0264 and 0.0396 $kg{\cdot}s^{-1}$ (mass fluxes of 2000 and 3000 $kg{\cdot}m^{-2}{\cdot}s^{-1}$)
Inlet temperature: 27°C
Heat flux: 203 $KW{\cdot}m^{-2}$ to 222 $KW{\cdot}m^{-2}$ (14% to 33% beyond CHF)
Thermodynamic quality: 16% to 50%

5.3 Experimental Procedures

The following experimental procedures are used to obtain surface temperature measurements at PDO conditions:

(i) The flow conditions of the loop are set by adjusting the pressurizer (for system pressure), flow-control valve (for flow rate), and preheater power (for inlet temperature).
(ii) The flow blockage is moved, by moving the magnets, to the inlet of the test section.
(iii) The power is slowly increased until the last thermocouple indicated dryout (a sharp rise in temperature); the flow conditions and power are recorded.

(iv) The power is continuously increased until the dryout front moves to the first upstream thermocouple at a location of about 72 cm from the inlet. For the cube type obstacle, the dryout front moves to the upstream thermocouple at about 80 to 84 cm. The flow conditions, power and thermocouple readings are recorded. This is used as the reference run (where the flow blockage does not pose any influence).

(v) The obstacle is moved slowly downstream and placed before the first thermocouple; the flow conditions, power and thermocouple readings are recorded.

(vi) The obstacle is moved further downstream in several steps until reaching the location of 89 cm from the inlet; the flow conditions, power and thermocouple readings are recorded at each step.

(vii) The procedures are repeated for other power and flow rate.

Appendix presents the recorded data at each run.

5.4 Experimental Observations

Several observations have been made during the experiment. They are presented as follows:

- The surface temperature measurements remain close to the saturation value (~44°C) at conditions before the occurrence of dryout.
- The last thermocouple shows a sudden increase in temperature (deviates from the more or less constant values) at dryout, but the increase is moderate.
- The thermocouples at upstream locations indicate dryout sequentially with increasing power.
- A sharp drop in surface temperature at the first upstream thermocouple is observed as the flow blockage is moved slowly downstream from the inlet end; this is an indication of rewetting. The same phenomenon is shown for the neighbouring thermocouples as the flow blockage continues to move towards the outlet.
- After the flow blockage passes over the location of the thermocouple, the surface temperatures at thermocouples upstream of the flow blockage increase back to the PDO

values while those downstream of the flow blockage remain wet.

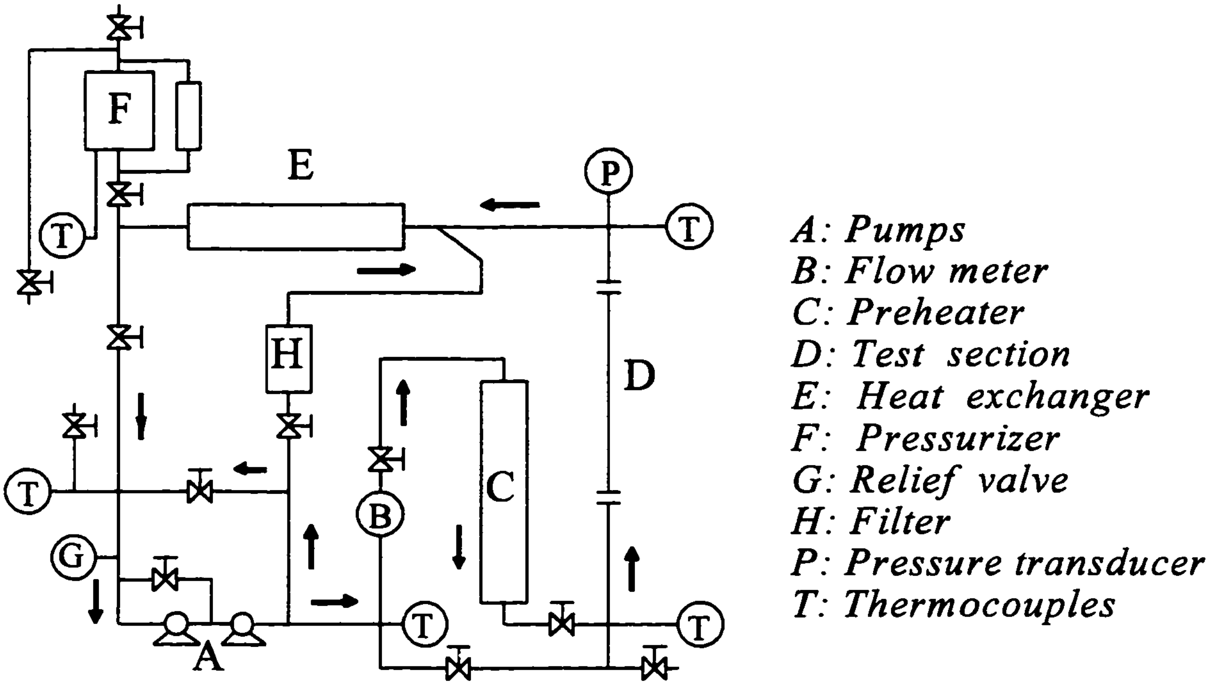

Figure 5.1. Sketch of multi-fluid loop

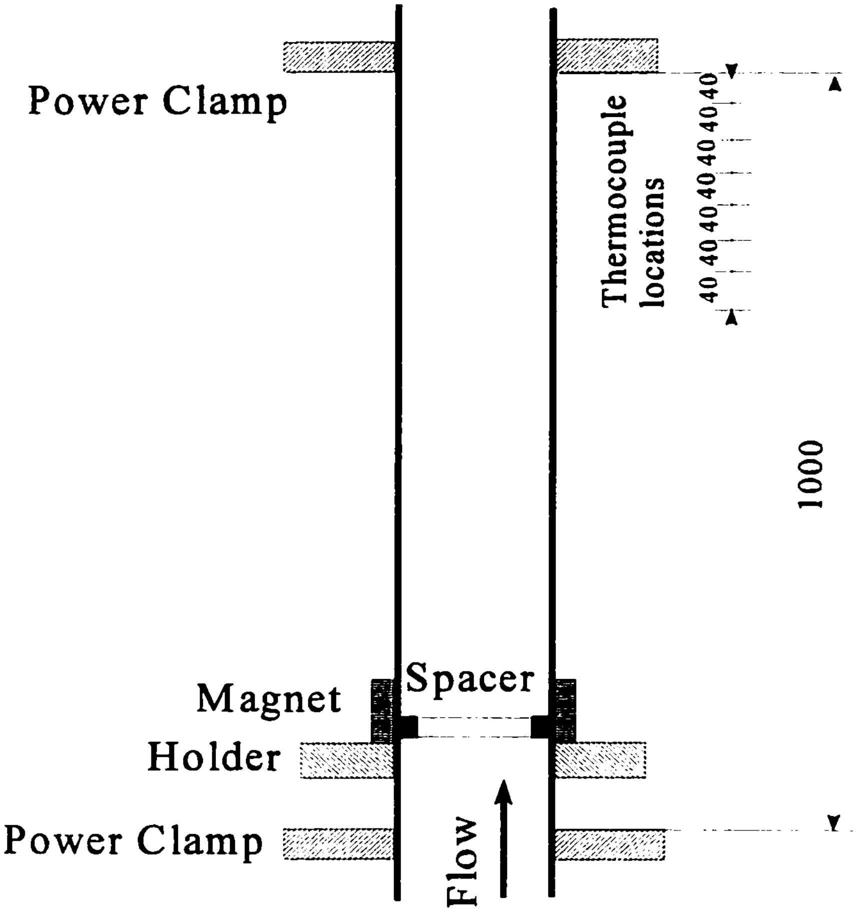

Figure 5.2. Test section (Dimensions in mm)

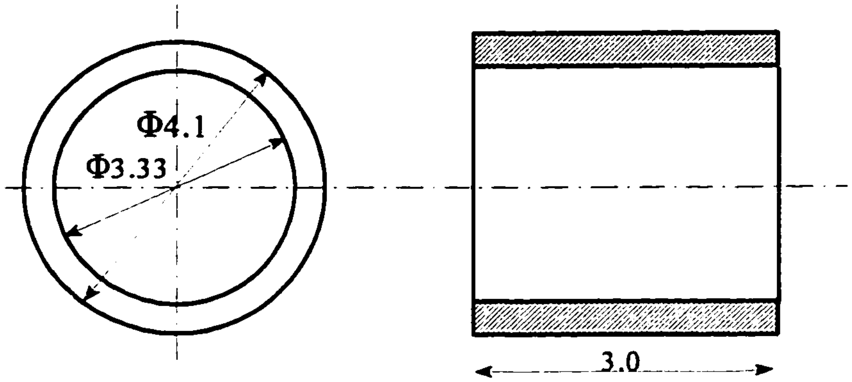

Ring type spacer

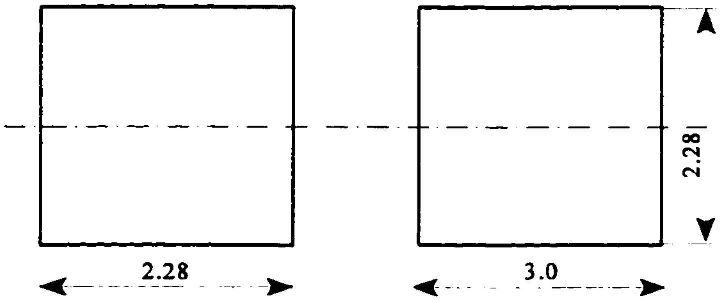

Cube type spacer

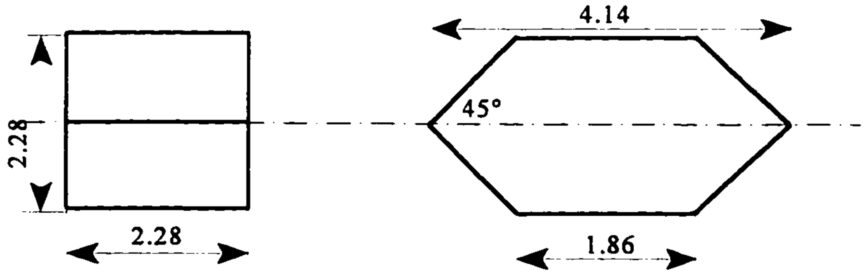

Hex type spacer

Figure 5.3 Configurations and dimensions of the flow obstructions (Dimensions in mm)

6. ANALYSIS OF EXPERIMENTAL DATA AND VALIDATION OF CORRELATION FOR THE EFFECT OF FLOW BLOCKAGE ON PDO HEAT TRANSFER

The surface temperature measurements obtained from the experiment are examined for the effect of flow blockage on PDO heat transfer. As discussed in previous chapters, this effect is anticipated to be similar to that induced by a spacing device of rod-bundle geometry. Hence, the findings of this experiment can be extended to bundle applications, which may include other effects caused by channel shape, gap size and others. The present analysis focuses mainly on the downstream region of the test section, where the thermocouples are located.

6.1 Surface Temperature Distributions for Tubes without Flow Blockage

Figure 6.1 shows the PDO surface temperature distributions at the downstream end of the test section for various sets of flow conditions. In these cases, the flow blockage was placed at a location 25 cm from the inlet end of the test section, while the first thermocouple was located at 72 cm. This corresponds to a length-to-diameter ratio of 115 between the flow blockage and the first point of measurement. Based on the results of other studies (e.g., Yao et al. (1982), Sergeev et al. (1990) and Kim and Korol'Kov (1991)), the flow blockage is not anticipated to have any influence on the flow or heat transfer at the locations where measurements were obtained.

The surface temperature measurements follow generally a similar trend, but are quite inconsistent. The higher temperature is observed at the last thermocouples (TC-1) for all runs. The temperatures decrease at TC-2 and TC-3, increase at TC-4 and TC-5, and decrease at TC-6. The variation of temperature at TC-7 and TC-8 depends on the flow conditions; it becomes lower indicating the occurrence of dryout or remains high for PDO conditions at these locations. This fluctuation of temperature measurements is mainly caused by the attachment technique of the thermocouples and is generally a function of the contact resistance between the thermocouples and the surface. The last thermocouple was attached permanently to the surface. This reduces the contact resistance and hence it is anticipated to provide the closest measurement of the actual temperature. On the other hand, the spring-loaded technique does not provide the "true" temperature measurements due to the contact resistance. It results in a systematic offset between the measurement and the actual temperature. Based on the observed trends, the contact resistance is the highest for both the TC-3 and TC-6, which provide systematically lower temperature measurements than those indicated by their neighboring thermocouples. A correction to the measurements can be introduced to account for the effect of contact resistance (Huang et al. 1996). However, it is felt unnecessary since the present study focuses only on the relative effect (surface temperature variations with and without the flow blockage).

At the mass flux of 2 $\mathrm{Mg \cdot m^{-2} \cdot s^{-1}}$, dryout was observed at a location between 76 and 80 cm for low heat flux (203 $\mathrm{KW \cdot m^{-2}}$). With increasing heat flux, the dryout front spread further upstream and beyond the measuring sections. At a mass flux of 3 $\mathrm{Mg \cdot m^{-2} \cdot s^{-1}}$, dryout was observed within the measuring section for high heat flux (222 $\mathrm{KW \cdot m^{-2}}$) but appears to have spread outside this section for low heat flux (217 $\mathrm{KW \cdot m^{-2}}$). This contradicts the general trend where the size of the dry patch is proportional to heat flux. Therefore, one of these two sets of data is erroneous.

Figure 6.2 shows the comparison of surface temperature values at various flow conditions. Most measurements scatter over the range of 140 to 200°C. The only exception are those obtained at the mass flux of 3 $\mathrm{Mg \cdot m^{-2} \cdot s^{-1}}$ and heat flux of 217 $\mathrm{KW \cdot m^{-2}}$; these data are systematically lower than the others. As indicated above, this set of data is probably erroneous. The quality range covered in the data is slight higher for low (i.e., 2 $\mathrm{Mg \cdot m^{-2} \cdot s^{-1}}$) than high (i.e., 3 $\mathrm{Mg \cdot m^{-2} \cdot s^{-1}}$) mass flux conditions.

6.2 Correction of Temperature Measurements

The temperature measurements can be corrected by calculating properly the contact resistance for each set of spring-loaded thermocouples. However, this correction is not feasible in the present set up of the experiment. As an alternative, the deviation between measurements and actual temperature readings can be determined by comparing the measurements of the reference tube against the predictions of a tube-based correlation. As indicated above, the reference tube data are obtained by moving the flow blockage to a location 25 cm from the inlet end of the test section.

A number of prediction methods have been derived for post-dryout heat transfer. Recently, Leung et al. (1997) developed a look-up table for post-dryout heat transfer coefficient, which covers a wide range of flow conditions and provides better prediction accuracy than other correlations and semi-analytical models. The post-dryout look-up table presents the heat transfer coefficient for an upward flow of steam-water mixture inside a 8-mm tube at discrete values of pressure, mass flux, thermodynamic quality and heat flux. Linear interpolation is applied for conditions in between of the table values. Since the table is valid only for steam-water flow, its predictions have to be transformed into Freon-134a equivalent values for comparison. In the present study, the following fluid-to-fluid modeling parameters are applied:

for pressure,

$$\left(\frac{\mu_g\, Cp_g}{k_g}\right)_{Freon-134a} = \left(\frac{\mu_g\, Cp_g}{k_g}\right)_{water} \tag{6-1}$$

for mass flux,

$$\left(\frac{G\, D}{\mu_g}\right)_{Freon-134a} = \left(\frac{G\, D}{\mu_g}\right)_{water} \tag{6-2}$$

for thermodynamic quality,

$$x_{Freon-134a} = x_{water} \tag{6-3}$$

for heat flux,

$$\left(\frac{q}{G\ H_{fg}} \right)_{Freon-134a} = \left(\frac{q}{G\ H_{fg}} \right)_{water} \tag{6-4}$$

for heat transfer coefficient,

$$\left(\frac{h\ D}{k_g} \right)_{Freon-134a} = \left(\frac{h\ D}{k_g} \right)_{water} \tag{6-5}$$

Based on the Dittus-Boelter equation, the effect of tube diameter (i.e., from 8 mm to the diameter of interest) can be accounted for using

$$\left(\frac{h_D}{h_{D=0.008m}} \right) = \left(\frac{D}{0.008} \right)^{-0.2} \tag{6-6}$$

The procedure for the transformation is described as follows:

(1) Use the experimental pressure value to evaluate the vapor properties of Freon-134a and calculate the Prandtl number (i.e., Equation (6-1)).

(2) Apply the steam table through iteration to determine the equivalent pressure value and vapor properties for water.

(3) Use the experimental mass flux value to calculate the Reynolds number (i.e., Equation (6-2)).

(4) Apply the same Reynolds number and steam viscosity to calculate the equivalent mass flux value for water.

(5) No transformation for thermodynamic quality is necessary (i.e., Equation (6-3)).

(6) Use the experimental heat flux and mass flux values together with the latent heat of vaporization to calculate the boiling number (i.e., Equation (6-4)).

(7) Apply the water-equivalent values of mass flux and latent heat of vaporization to obtain the water-equivalent heat flux value.

(8) Evaluate the post-dryout heat transfer coefficient based on the water-equivalent values of pressure, mass flux, heat flux and thermodynamic quality.

(9) Convert the heat transfer coefficient to Freon-134a equivalent value using Equation (6-5).

(10) Modify the table prediction for the tube diameter of interest using Equation (6-6).

(11) Calculate the surface temperature with

$$T_w = \frac{q}{h_D} + T_{sat} \tag{6-7}$$

where T_{sat} is the saturation temperature in K (or °C).

Figure 6.3 presents the comparison of the predictions of the post-dryout look-up table and the experimental data for various flow conditions. As expected, the post-dryout look-up table tends to overpredict most of the temperature measurements. However, except for the data obtained at the mass flux of 3 $\mathrm{Mg \cdot m^{-2} \cdot s^{-1}}$ and heat flux of 217 $\mathrm{KW \cdot m^{-2}}$, the agreement between predictions and data is relatively good. Based on the differences between predictions and data, a temperature correction is calculated for each thermocouples reading (i.e., $T_{w,\,corr} = T_{w,\,table} - T_{w,\,data}$) and is applied to the measurements. Figure 6.4 illustrates the differences between the original and corrected measurements. The corrected measurements are presented in the following comparisons from here on.

6.3 Effect of Flow Blockage on Post-Dryout Heat Transfer

The effect of flow blockage on post-dryout heat transfer is examined by (i) varying the location of the blockage along the channel, and (ii) using different types of flow blockage. As described in the previous chapter, three types of flow blockage were tested in the present study: ring-shape, cube-shape and hex-shape.

6.3.1 Ring-Shaped Blockage

Figure 6.5 shows the surface temperature distributions with a ring-shaped blockage located upstream of the thermocouples at a mass flux of 2 $Mg{\cdot}m^{-2}{\cdot}s^{-1}$. A decrease in surface temperature was observed at two upstream thermocouples while those close to the exit of the test section approach the temperature of a plain tube. This decrease is often referred to as the rewetting phenomenon and is caused by the enhancement effect of the blockage. The extent of this effect covers approximately 16 cm from the blockage and is independent from the blockage location.

At locations close to the dryout point in the post-dryout region (where the surface temperature begin to increase sharply), the surface temperature is slightly lower than that of a plain tube. This is caused by the developing flow effect at these conditions while that of a plain tube represents the fully developed post-dryout conditions. With increasing distance from the dryout point, the flow approaches fully developed conditions and the measurements approach the plain tube temperature. The small systematic differences in temperature (about 10°C) for the blockage located between 60 cm and 62 cm are probably due to uncertainty in the temperature measurements.

Figure 6.6 shows the surface temperature distributions for the same blockage at a mass flux of 3 $Mg{\cdot}m^{-2}{\cdot}s^{-1}$. A similar trend to that of Figure 6.5 was observed; thermocouples at the upstream locations display a lower temperature than those at the downstream locations. The temperature rise at the dryout point, however, appears to be much more rapid at these conditions than that observed previously at a mass flux of 2 $Mg{\cdot}m^{-2}{\cdot}s^{-1}$. A comparison of surface temperature distributions for various mass fluxes is not feasible since there is no overlapping range of thermodynamic quality. In general, a lower surface temperature was observed at high mass flux conditions.

Figure 6.7 shows the surface temperature distributions with a ring-shaped blockage located inside the thermocouples region at a mass flux of 2 $Mg{\cdot}m^{-2}{\cdot}s^{-1}$. Unlike the trends exhibited in Figures 6.5 and 6.6, high temperature is shown at both the upstream and downstream ends of the thermocouples region (approaching the plain tube value) while low temperature (wet region) is displayed at locations just downstream of the blockage. The dryout front (i.e., corresponds to the thermocouples with a sharp temperature rise) moves downstream with the variation in blockage locations. The developing-flow region can be clearly identified at each case. With the blockage located at 85 cm (local thermodynamic quality of 0.4), a decrease in surface temperature was also observed at the location of the blockage. This enhancement effect is caused by the increase in velocity as the flow passes through the reduced area over the blockage. The same phenomenon was also noted by Hassan and Rehme (1981) in single-phase flow over a spacer grid.

Figure 6.8 shows the surface temperature distributions with a ring-shaped blockage located inside the thermocouples region at a mass flux of 3 $Mg{\cdot}m^{-2}{\cdot}s^{-1}$. As observed previously in Figure 6.7, high-temperature measurements are shown at locations upstream of the blockage while rewetting of surface is exhibited at locations immediately downstream of the blockage. Dryout is repeated at locations close to the exit of the test section.

6.3.2 Cube-Shaped Blockage

The surface temperature distributions along the channel equipped with a cube-shaped blockage are shown in Figure 6.9, which corresponds to those of Figures 6.5 to 6.8. They exhibit similar trends to those displayed for the ring-shaped blockage, where a strong enhancement effect of heat transfer rate (low surface temperature) is shown at locations downstream of the blockage. Dryout is re-established at downstream locations far away from the blockage, indicating the deterioration of the enhancement effect.

When the blockage is placed within the thermocouples region, the post-dryout region at locations upstream of the blockage is suppressed by the presence of the blockage. Only a short temperature spike is shown at the location just upstream of the blockage, beyond which the surface rewets quickly due to the enhancement effect.

6.3.3 Hex-Shaped Blockage

The tests with a hex-shaped blockage cover only a mass flux of 2 $Mg{\cdot}m^{-2}{\cdot}s^{-1}$. Figure 6.10 shows the surface temperature distributions obtained from these tests. Although the same trends as those previously shown for other blockages were observed, a rather different characteristic is exhibited for this blockage. The developing flow region at the vicinity of the dryout point covers a wider range of conditions. This signifies a relatively higher turbulence level for the hex-shaped blockage.

6.3.4 A Comparison of Surface Temperature Distributions between Various Blockages

The surface temperature distributions between various types of blockage are compared to determine the effectiveness of post-dryout heat transfer enhancement. Figure 6.11 shows the comparison of surface temperature for constant flow conditions and a fixed blockage location (at 60 cm). The heat flux is slightly lower for the cube-shaped blockage while those of the ring-shaped and hex-shaped blockages are relatively close. At the upstream locations of the thermocouples region, the surface temperature is low due to the enhancement effect of the blockage. As discussed above, this signifies that the tube surface is wet. Depending on the shape of the blockage, the extent of the wet region is quite different. The re-establishment of the post-dryout region occurs at a much lower thermodynamic quality for the ring-shaped blockage than for the cube-shaped blockage. Although the slightly lower heat flux for the channel with the cube-shaped blockage is probably part of the contributing factor, the main reason is caused by the higher turbulence level generated by the cube-shaped blockage.

Salcudean and Leung (1988) showed that the location of the blockage influences strongly the single-phase pressure drop and hence the turbulence level in the channel. They observed a higher pressure drop for a blockage located at the central region than one placed in the peripheral region of the channel, based on the same blockage area and flow conditions. Figure 4.10 presents the schematic diagram of various blockage locations tested by Salcudean and Leung (1989). The ring-shaped blockage corresponds closely to the peripheral obstruction, while the cube-shaped blockage may be considered as a peripheral-segment obstruction. Table 4.2 presents the single-phase loss coefficients for various obstructions.

The differences in surface temperature distributions between the cube-shaped and hex-shaped blockages lie mainly on the gradual variations of the leading and trailing edges for the latter. As shown by Idelchik (1994), a blockage with an equilateral triangular-shaped leading edge reduces the drag by 50% as compared to one with a flat leading edge. Therefore, the turbulence level downstream of the hex-shaped blockage is anticipated to be lower, and the heat transfer enhancement is less, than that of the cube-shaped blockage.

Figure 6.12 shows a similar comparison for blockages located inside the thermocouples region. The surface temperature distribution of the ring-shaped blockage has shifted slightly to higher quality conditions (by about 5%). By adjusting this distribution to coincide with the others, the same trend as observed in Figure 6.11 is displayed. The enhancement effect at downstream locations is much stronger for the cube-shaped blockage than for the ring-shaped blockage.

6.4 Validation of Correlation for the Effect of Flow Blockage on Post-Dryout Heat Transfer

The data obtained from the present experiment are used to validate the methodology described in Chapter 4. This validation exercise is based on a comparison between the measured and predicted surface temperature distributions in the channel equipped with a blockage. Since the present study focuses mainly on the effect of spacer on post-dryout heat transfer, other relevant information are obtained with either available correlations (or look-up table) or the experimental data. According to Equations (4-7) and (4-10), the following parameters are required: the geometric parameters (i.e., both the axial distance downstream from the blockage, Z, and the hydraulic-equivalent diameter,

D_{hy}), local equilibrium quality, x_e, single-phase loss coefficient, K_{ob}, and the reference heat transfer coefficient for post-dryout flow in a tube (without any blockage), $h_{no\ spacer}$. The local surface temperature is calculated with the heat transfer coefficient of a spacer-equipped tube, h_{spacer} (Equation (4-7)).

Among these parameters, both the axial distance, Z, and hydraulic equivalent diameter are available from the location of interest. The local thermodynamic quality, x_{th} (in this experiment x_e=x_{th}), is calculated with a heat balance, i.e.,

$$x_{th} = \frac{1}{H_{fg}}\left(\frac{Power}{W} + H_{in} - H_f\right) \quad \textbf{(6-8)}$$

where Power is the local power in Watt, W is the mass flow rate in kg·s^{-1}, H_{in} is the bulk-fluid enthalpy at the inlet in J·kg^{-1}, H_f is the saturated-liquid enthalpy in J·kg^{-1}, and H_{fg} is the latent heat of vaporization in J·kg^{-1}. The single-phase loss coefficient is evaluated with Equation (4-9) (Leung and Hotte 1997); the constants for the peripheral obstruction are applied to the ring-shaped blockage and those for the peripheral segment obstruction are used to the cube-shaped blockage. Based on Idelchik (1994), the single-phase loss coefficient for the hex-shaped blockage is assumed to be half of the value for the cube-shaped blockage. The reference heat transfer coefficient for fully developed post-dryout flow in a tube is predicted using the post-dryout look-up table (Leung et al. 1997).

6.4.1 Other Separate Effects on Post-Dryout Heat Transfer

There are other separate effects on post-dryout heat transfer, in addition to the spacer effect. A brief description on two of these effects, which are relevant to the present validation, is presented here together with their prediction methodologies. Detailed discussions on these effects are not provided since they are beyond the scope of the present study.

Figure 6.13 shows the comparison of surface temperature distributions between predictions and measurements along the channel with a ring-shaped blockage. A good agreement is shown at high temperature region (i.e., post-dryout conditions at both ends of the section) but the correlation overpredicts considerably the surface temperature at the wet region. The overprediction is caused by neglecting the rewetting phenomenon due to the enhancement effect of the blockage on CHF.

To improve the prediction accuracy, a correlation for the enhancement effect of blockage on local CHF is derived with the present set of data. It is derived using the same form as suggested by Doerffer et al. (1996) and is expressed as

$$\frac{CHF_{sp}}{CHF_0} = 1 + 0.55 \exp\left(-0.015 \frac{Z}{D_{hy}} \right) \tag{6-9}$$

where CHF_0 is the reference CHF value for a plain tube in $W \cdot m^{-2}$. At each location of interest, the local heat flux is compared against the enhanced CHF value as predicted by the above equation. Nucleate boiling is assumed when local heat flux is less than the enhanced CHF value. Otherwise, post-dryout boiling is considered.

Figure 6.14 shows the comparison of surface temperature distributions between predictions (including the enhancement effect of the blockage on CHF) and measurements. A significant improvement is displayed in surface temperature predictions at the wet region. However, at the location where dryout is re-established, the surface temperature values remain to be overpredicted by the present methodology. As discussed previously in Section 6.3, the post-dryout flow has to develop gradually downstream of the dryout point. Over the developing-flow region, a large amount of liquid droplets impinge on the heated surface and in turn accelerate the heat transfer process through the droplet-surface interaction. This increase in heat transfer rate has to be accounted appropriately to improve the prediction accuracy over this region.

Up until recently, no generalized prediction method has been presented to account for the developing-flow effect on post-dryout heat transfer. A few recommended correlations were derived with dimensional parameters and hence are not applicable for the present applications. Recently, AECL has completed an analysis of the developing flow effect on post-dryout heat transfer (Leung and Zhang, report in preparation). A correlation was derived with the AECL post-dryout data bank of steam-water flow. It is expressed as

$$\frac{Nu_{dev}}{Nu_{pdo}} = 1 + \left(\frac{Nu_{pre}}{Nu_{pdo}} - 1 \right) \exp\left(-10.83 \left(\frac{q}{CHF_{sp}} - 1 \right)^{0.37} We^{-0.08} \left(\frac{\rho_f}{\rho_g} \right)^{0.28} \right) \qquad \textbf{(6-10)}$$

where Nu_{dev} is the Nusselt number at developing-flow conditions, Nu_{pre} is the Nusselt number at fully developed pre-dryout conditions, Nu_{pdo} is the Nusselt number at fully developed post-dryout conditions, CHF_{sp} is the local critical heat flux in $W \cdot m^{-2}$, q is the local heat flux in $W \cdot m^{-2}$. We is the Weber number, and ρ_f and ρ_g are the densities for saturated liquid and saturated vapor, respectively. Although this correlation was derived with steam-water data, it is anticipated to be also applicable for Freon-134a flow because of its non-dimensional form.

Figure 6.15 presents the comparison of surface temperature distributions between predictions (including both the CHF enhancement effect of blockage and developing-flow effect) and measurements. The agreement has been significantly improved; the measured temperature distribution is predicted closely by the present methodology. Improvement has also been observed at the high temperature region near the exit of the test section, as compared to that shown in Figure 6.13.

6.4.2 Validation Results for the Proposed Prediction Methodology

Several additional comparisons are presented in the following figures to illustrate the capability of the present prediction methodology for various flow conditions and blockage types. Figure 6.16 presents the comparisons of surface temperature distributions along the channel with the ring-shaped blockage located at various locations for a mass flux of 2 $Mg{\cdot}m^{-2}{\cdot}s^{-1}$ (Figure 6.15 is also repeated in this figure for completeness). All surface temperature distributions are predicted closely by the proposed methodology including both the dry and wet regions.

Figure 6.17 shows the comparisons for a mass flux of 3 $Mg{\cdot}m^{-2}{\cdot}s^{-1}$. The prediction accuracy remains good at post-dryout conditions. Improvement may be needed in the calculation of heat transfer coefficients in nucleate boiling (which is outside the scope of present study). On the other hand, this set of data appears to have a much higher uncertainty than the others as discussed previously in Section 6.3.

The measured surface temperature distributions in the channel with a cube-shaped blockage are compared against the predictions. Figure 6.18 shows also a close agreement between measurements and predictions for both the pre- and post-dryout regions.

Figure 6.19 shows the comparison between the predictions and the surface temperature distributions with a hex-shaped blockage. Again, a close agreement has been obtained in the post-dryout regions.

6.5 Summary

Experimental data have been obtained to show the effect of flow blockage on post-dryout heat transfer. The heat transfer rate was enhanced significantly in the presence of a flow blockage. This enhancement depends strongly on the location and shape of the blockage. It is higher for the blunt-type blockage which extends further to the core flow than one obstructing the low-velocity flow close to the surface. Rewetting of surface has been noted at locations downstream of the blockage. This results in a sharp increase in heat transfer rate (at nucleate boiling).

The proposed prediction methodology for the enhancement effect of spacers has been validated against the experimental data. Due to the complex nature of the phenomena, several additional adhoc correlations have been introduced to account for the enhancement effect of flow blockage on CHF and the developing-flow effect on post-dryout heat transfer. Using the combined methodology, the measured surface temperature distributions were predicted closely at both the wet and dry regions. This validates the proposed prediction methodology which was derived mainly with single-phase air-flow and high-quality steam-water data. The fact that it is applicable for relatively low quality flow of Freon-134a has improved further the confident level.

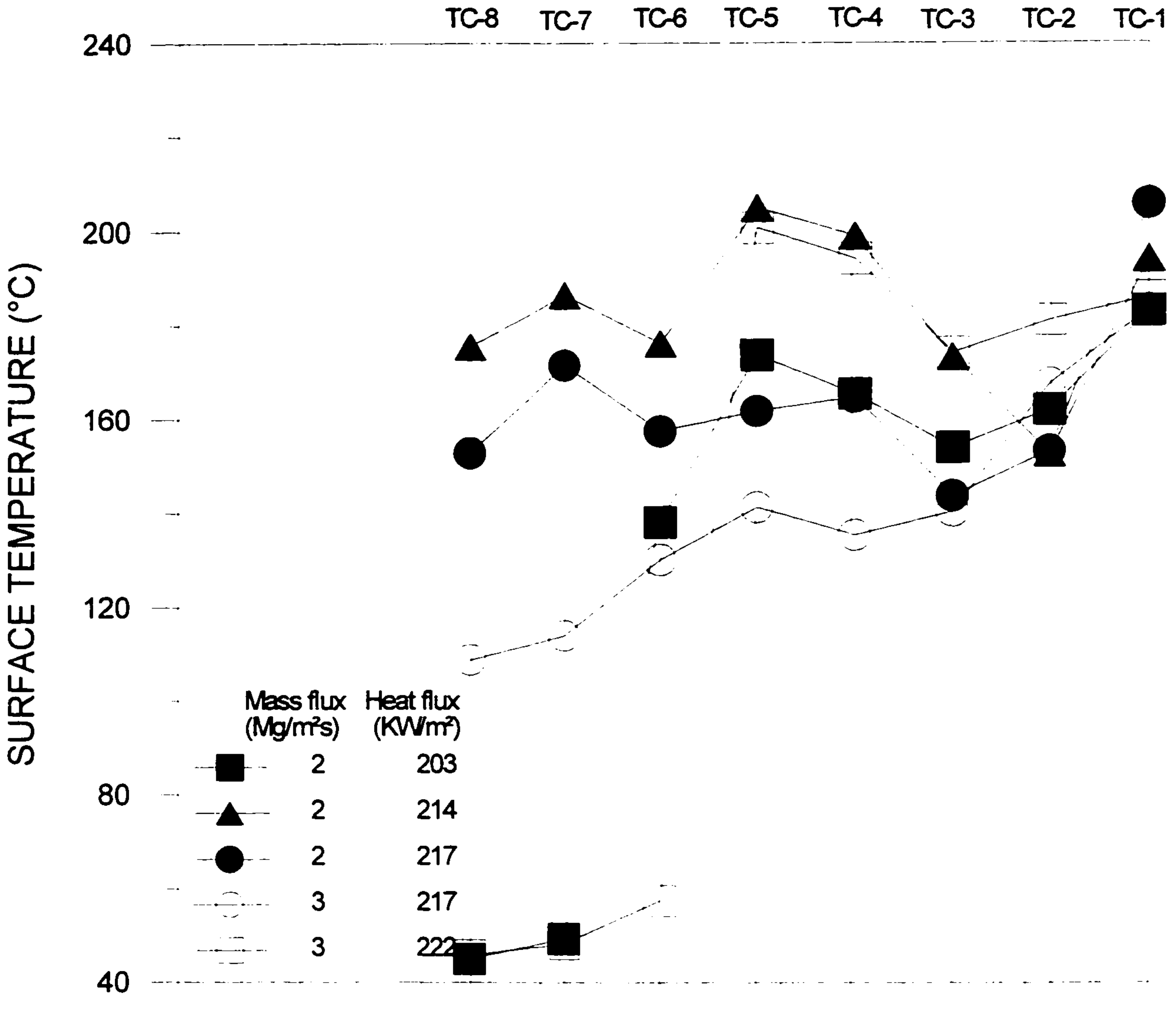

Figure 6.1. Surface temperature distributions at PDO conditions

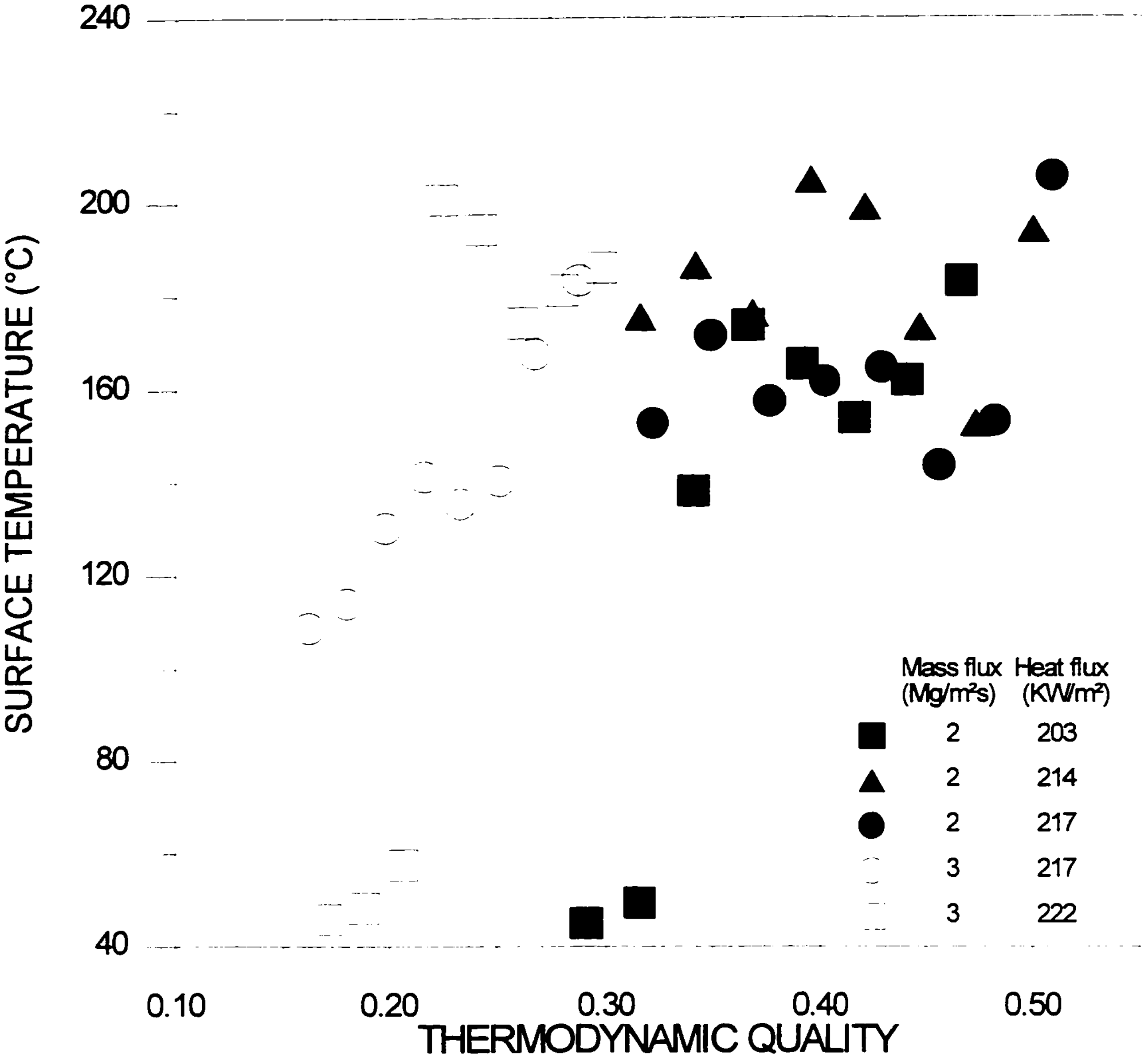

Figure 6.2. Surface temperature measurements at various thermodynamics qualities

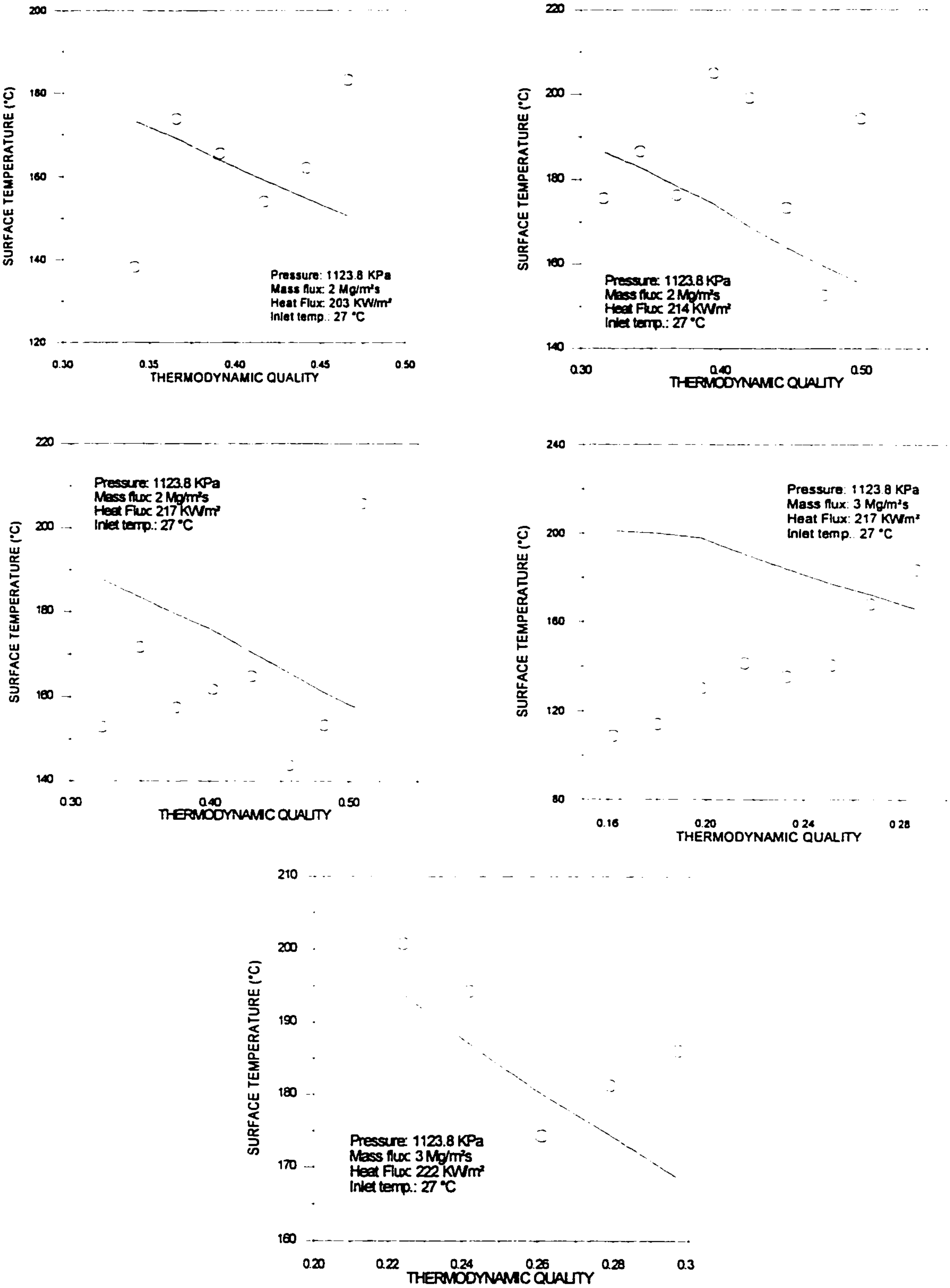

Figure 6.3. Comparison of prediction of the post-dryout look-up table against experimental data

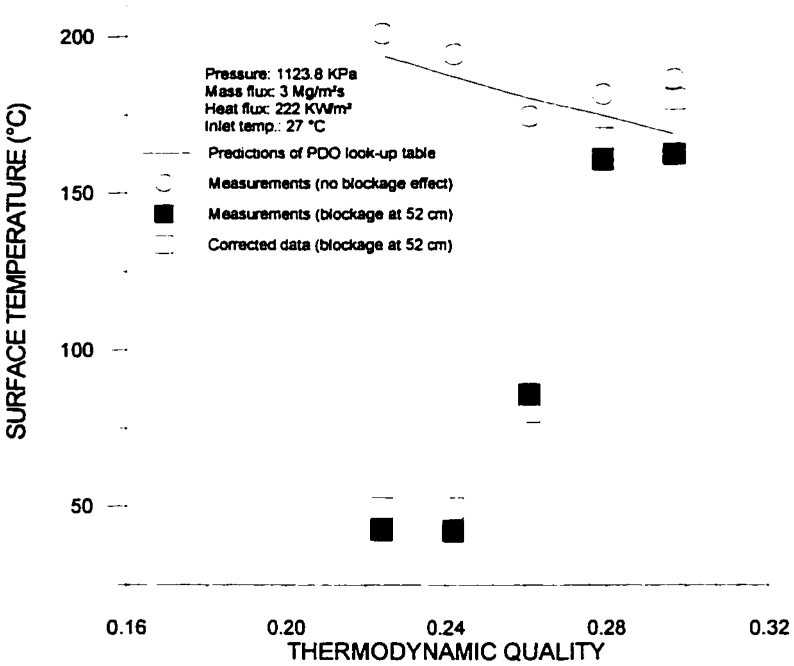

Figure 6.4. Illustration of difference between original and corrected measurements

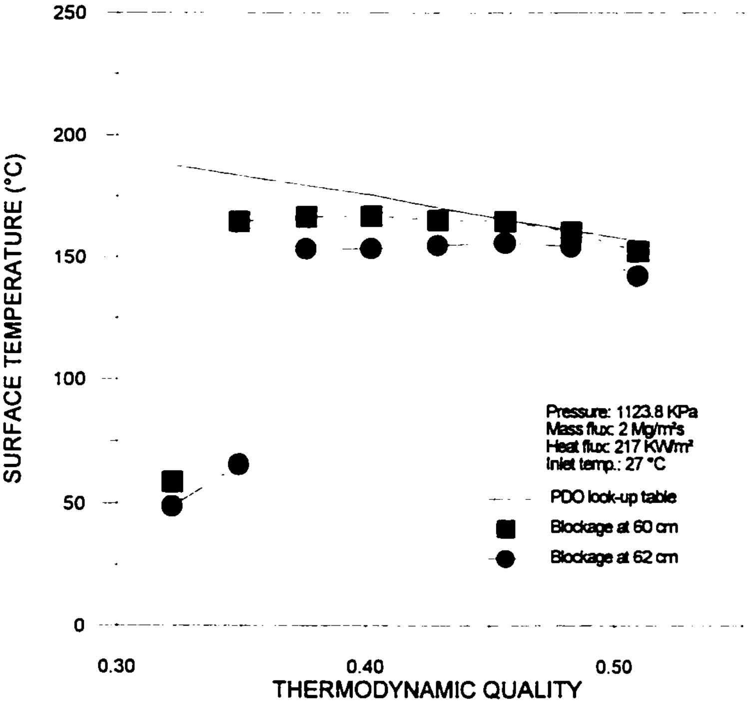

Figure 6.5. Distributions of surface temperature with the ring-shaped blockage located before the thermocouples at a mass flux of 2 Mg/m²s

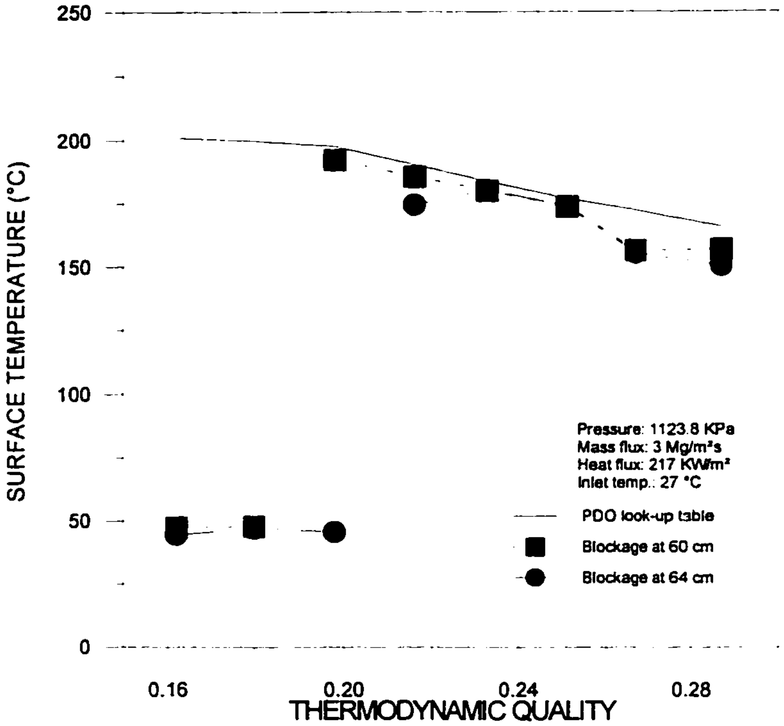

Figure 6.6. Distributions of surface temperature with the ring-shaped blockage located before the thermocouples at a mass flux of 3 Mg/m²s

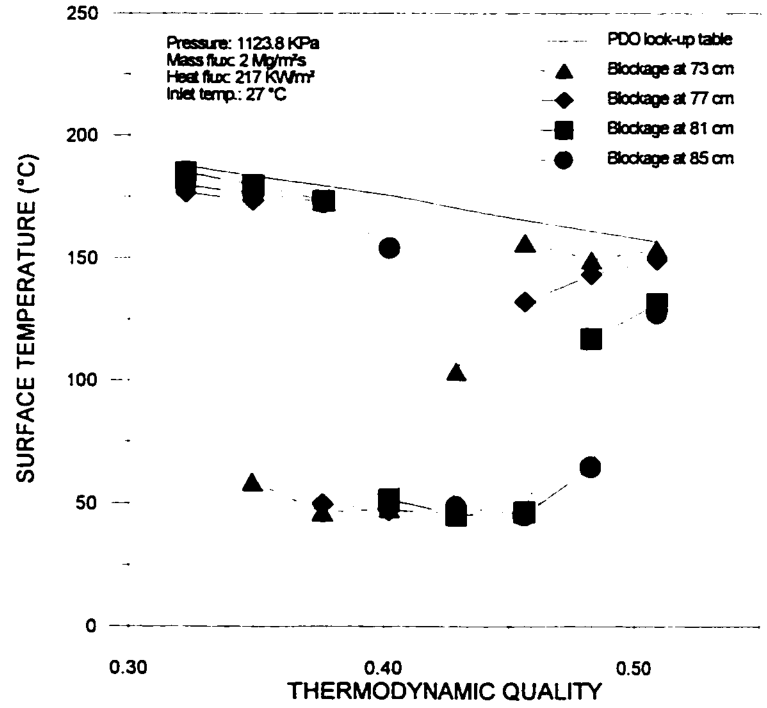

Figure 6.7. Distributions of surface temperature with the ring-shaped blockage located inside the thermocouples region at a mass flux of 2 Mg/m²s

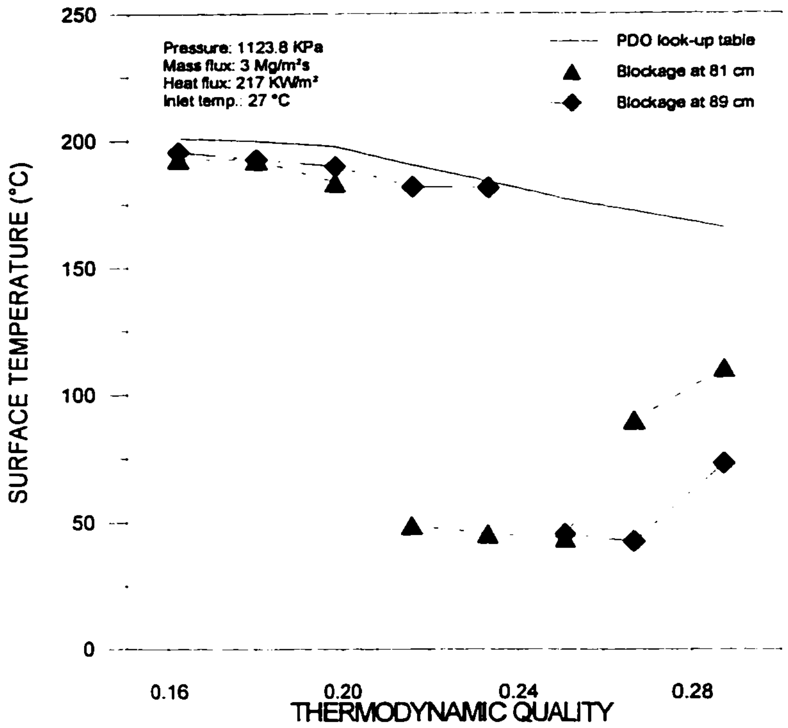

Figure 6.8. Distributions of surface temperature with the ring-shaped blockage located inside the thermocouples region at a mass flux of 3 Mg/m^2s

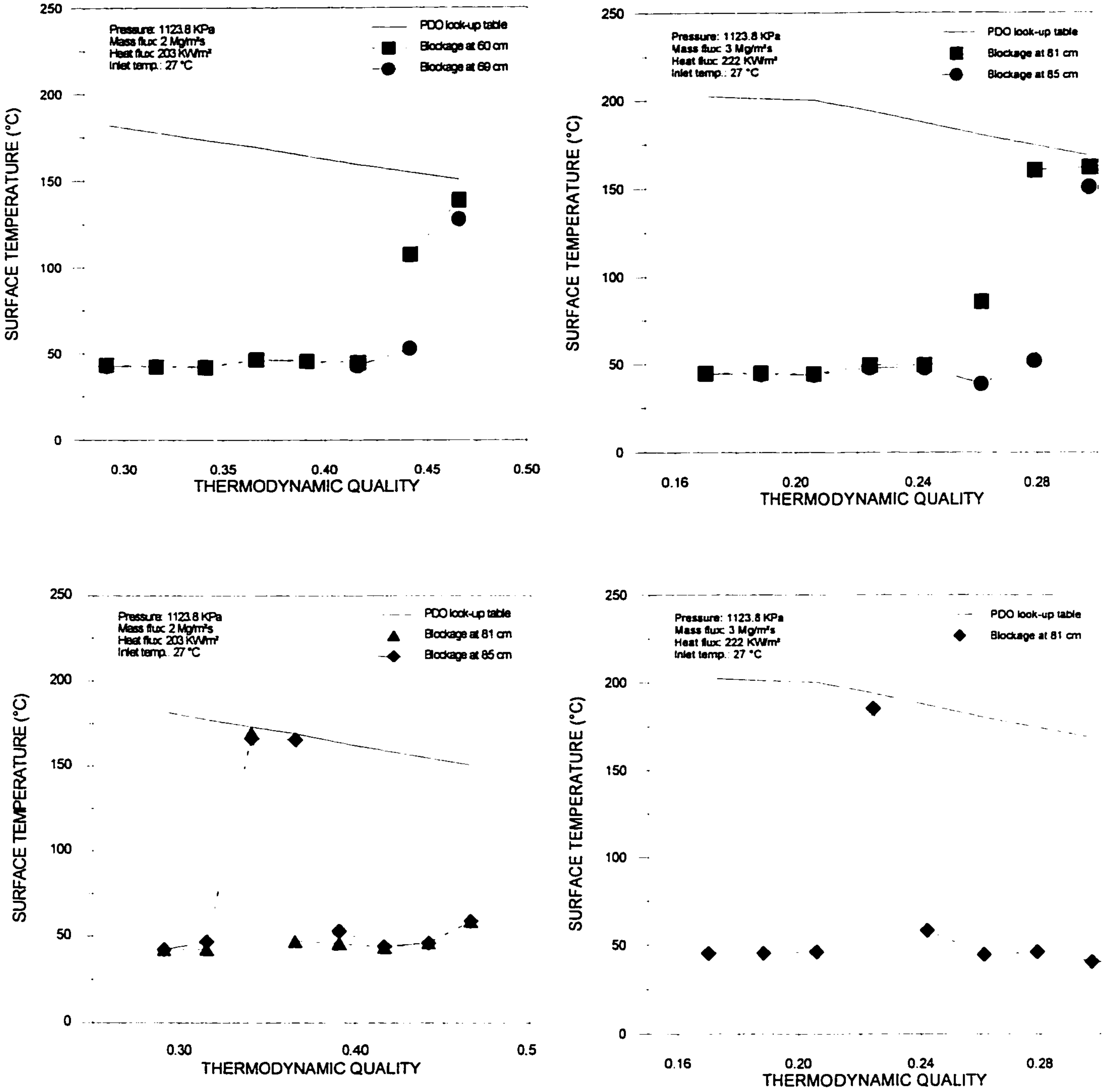

Figure 6.9. Distributions of surface temperature with the cube-shaped blockage

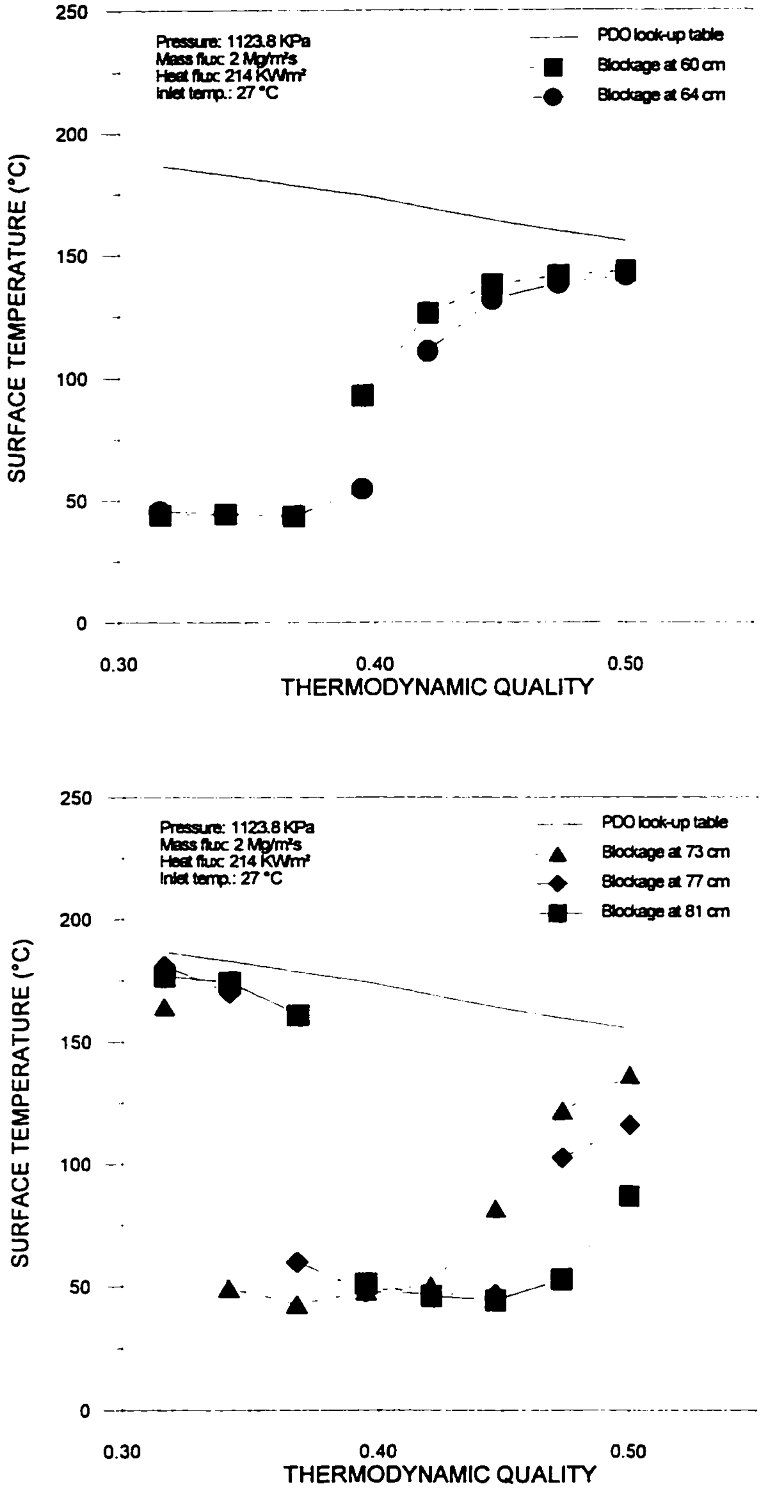

Figure 6.10. Distributions of surface temperature with the hex-shaped blockage

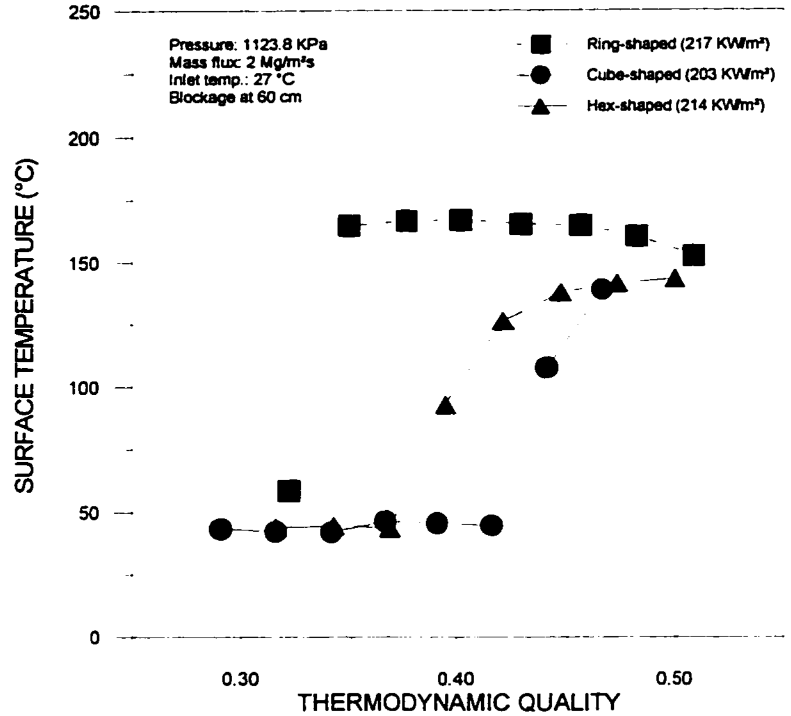

Figure 6.11. A comparison of surface temperature distributions for various blockages located upstream of the thermocouples region at a mass flux of 2 Mg/m²s

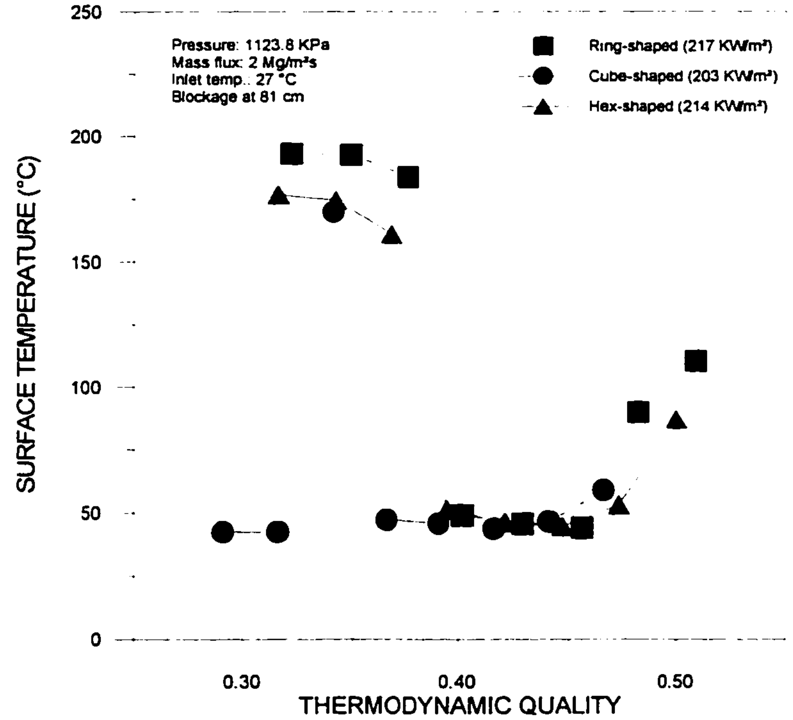

Figure 6.12. A comparison of surface temperature distributions for various blockages located inside the thermocouples region at a mass flux of 2 Mg/m²s

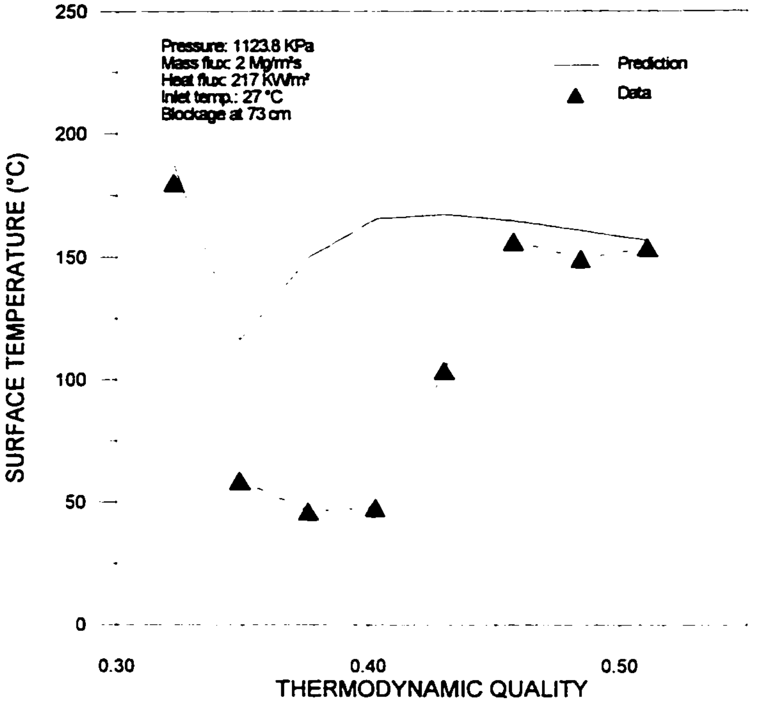

Figure 6.13. A comparison of surface temperature distributions between predictions and measurements along the channel with a ring-shaped blockage

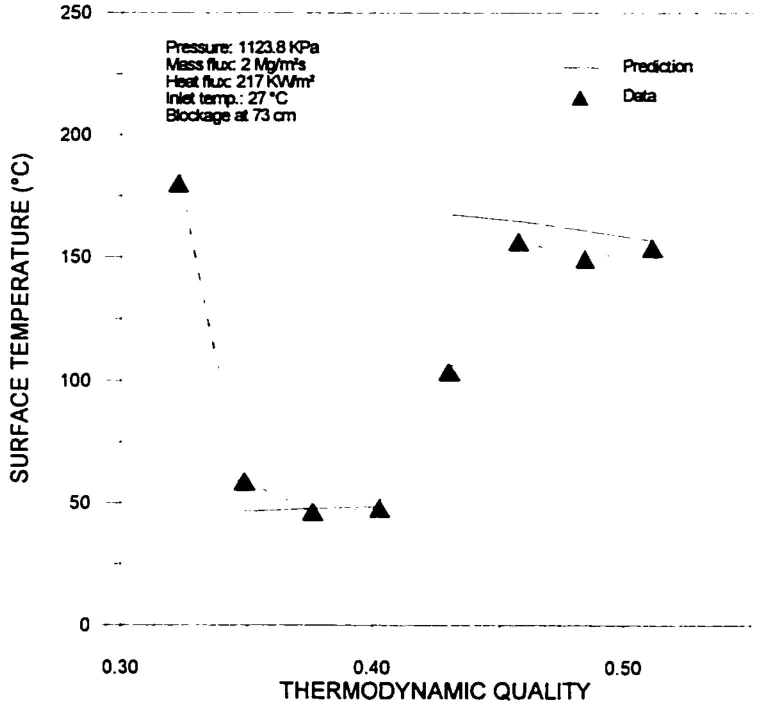

Figure 6.14. A comparison of surface temperature distributions between predictions and measurements along the channel with a ring-shaped blockage (including the CHF enhancement effect of the blockage)

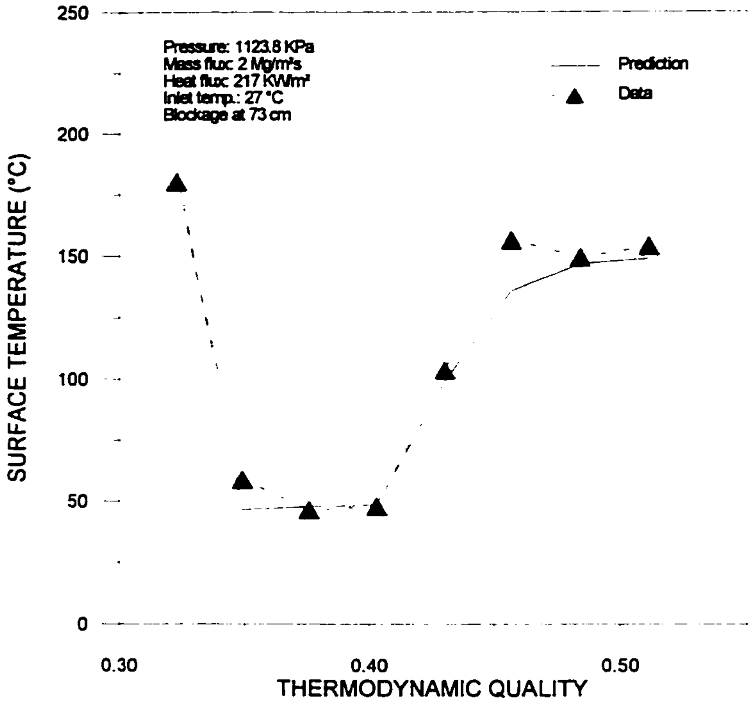

Figure 6.15. A comparison of surface temperature distributions between predictions and measurements along the channel with a ring-shaped blockage (including the CHF enhancement effect of the blockage and developing flow effect)

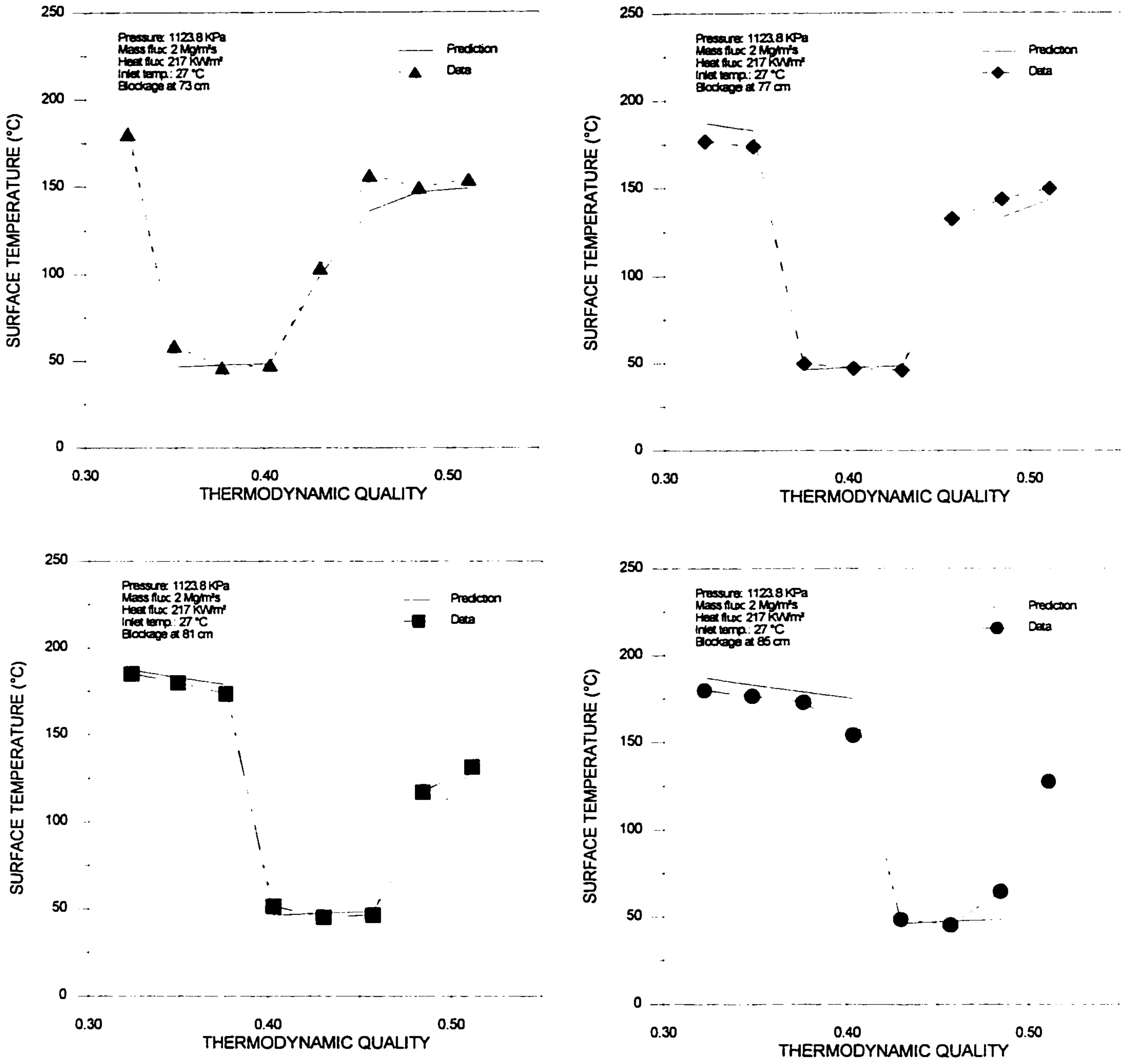

Figure 6.16. A comparison of surface temperature distributions between predictions and measurements along the channel with a ring-shaped blockage at various locations for a mass flux of 2 Mg/m²s (including the CHF enhancement effect of the blockage and developing flow effect)

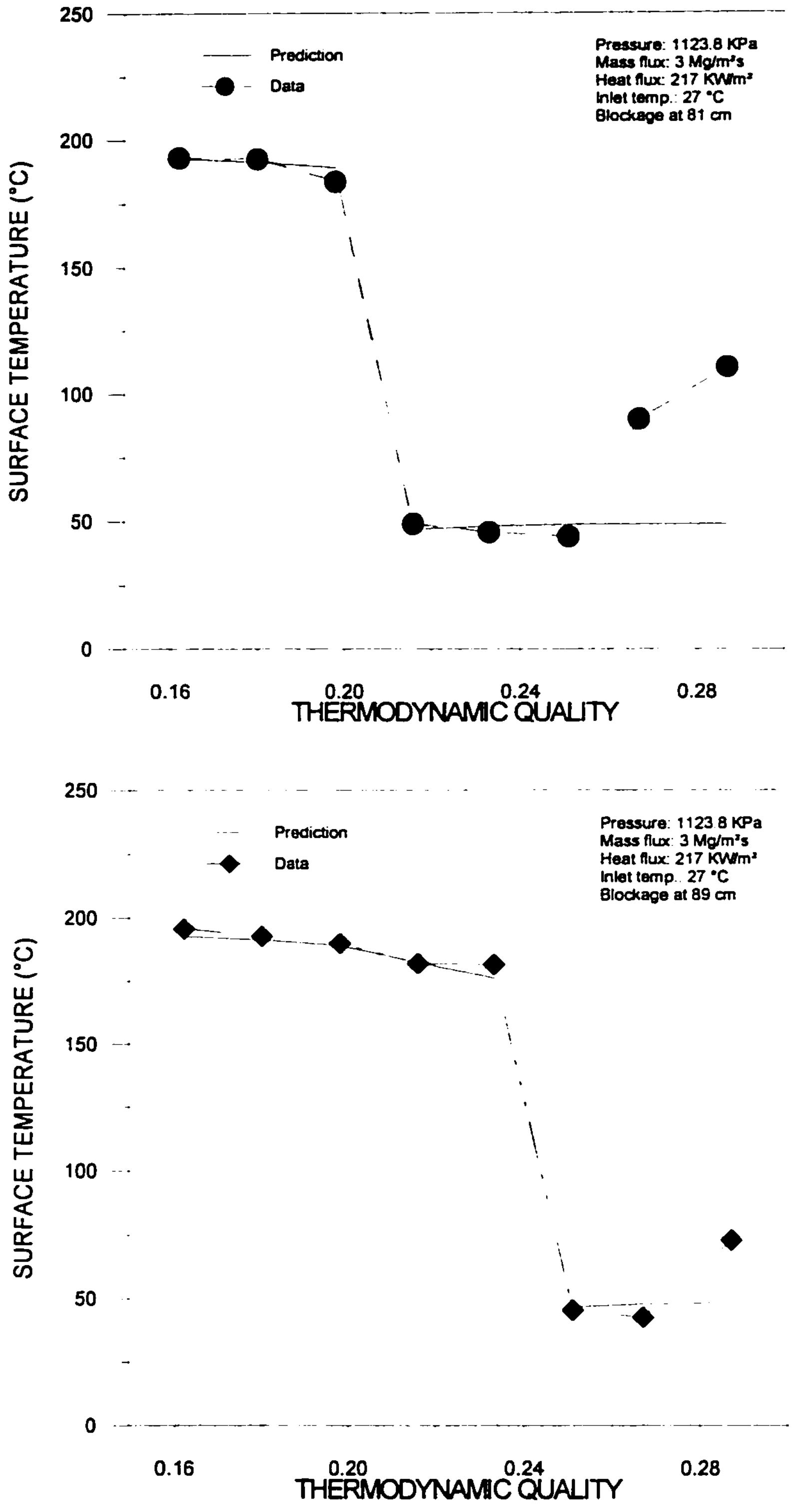

Figure 6.17. A comparison of surface temperature distributions between predictions and measurements along the channel with a ring-shaped blockage at various locations for a mass flux of 3 Mg/m²s (including the CHF enhancement effect of the blockage and developing flow effect)

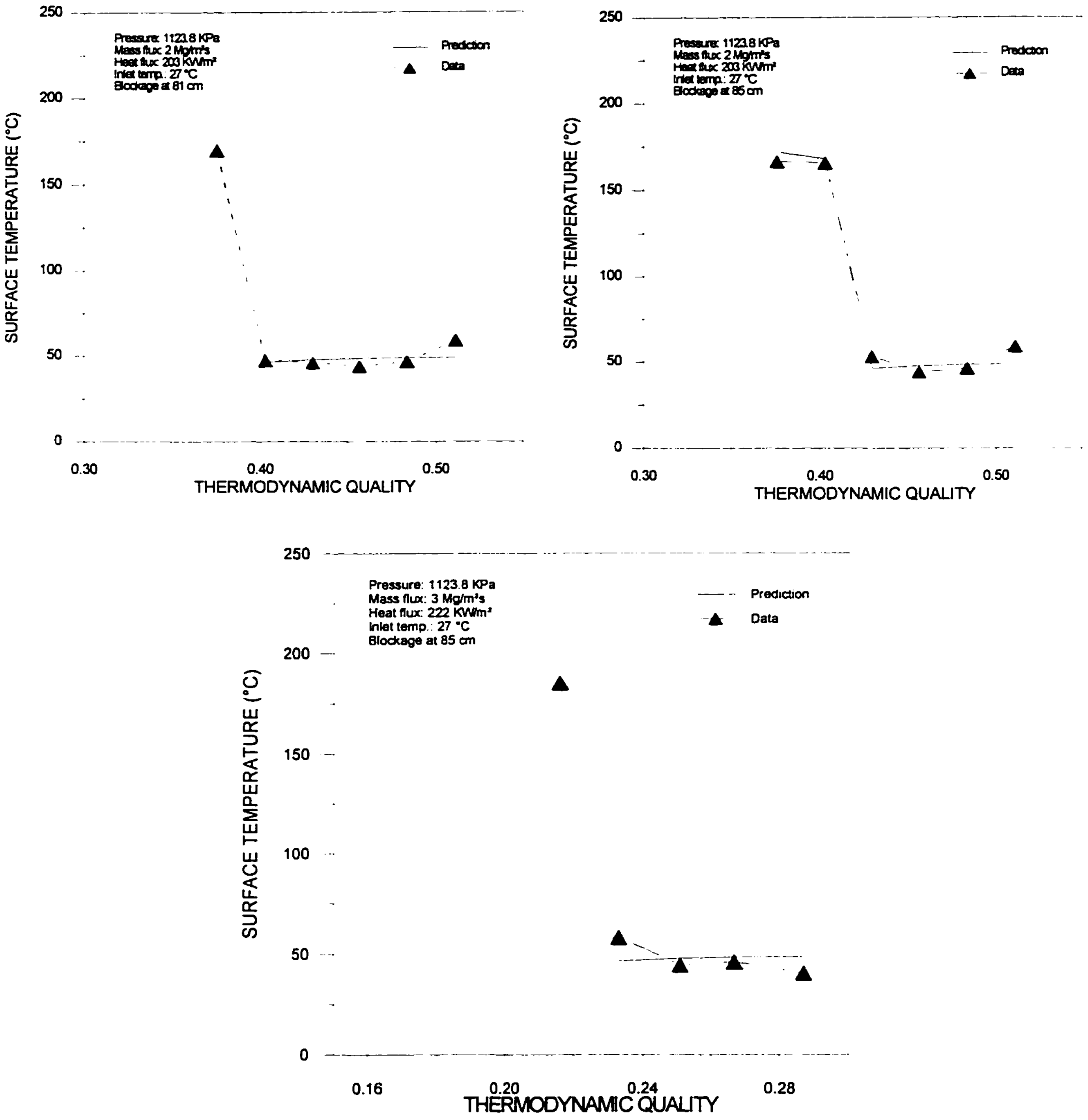

Figure 6.18. A comparison of surface temperature distributions between predictions and measurements along the channel with a cube-shaped blockage at various locations (including the CHF enhancement effect of the blockage and developing flow effect)

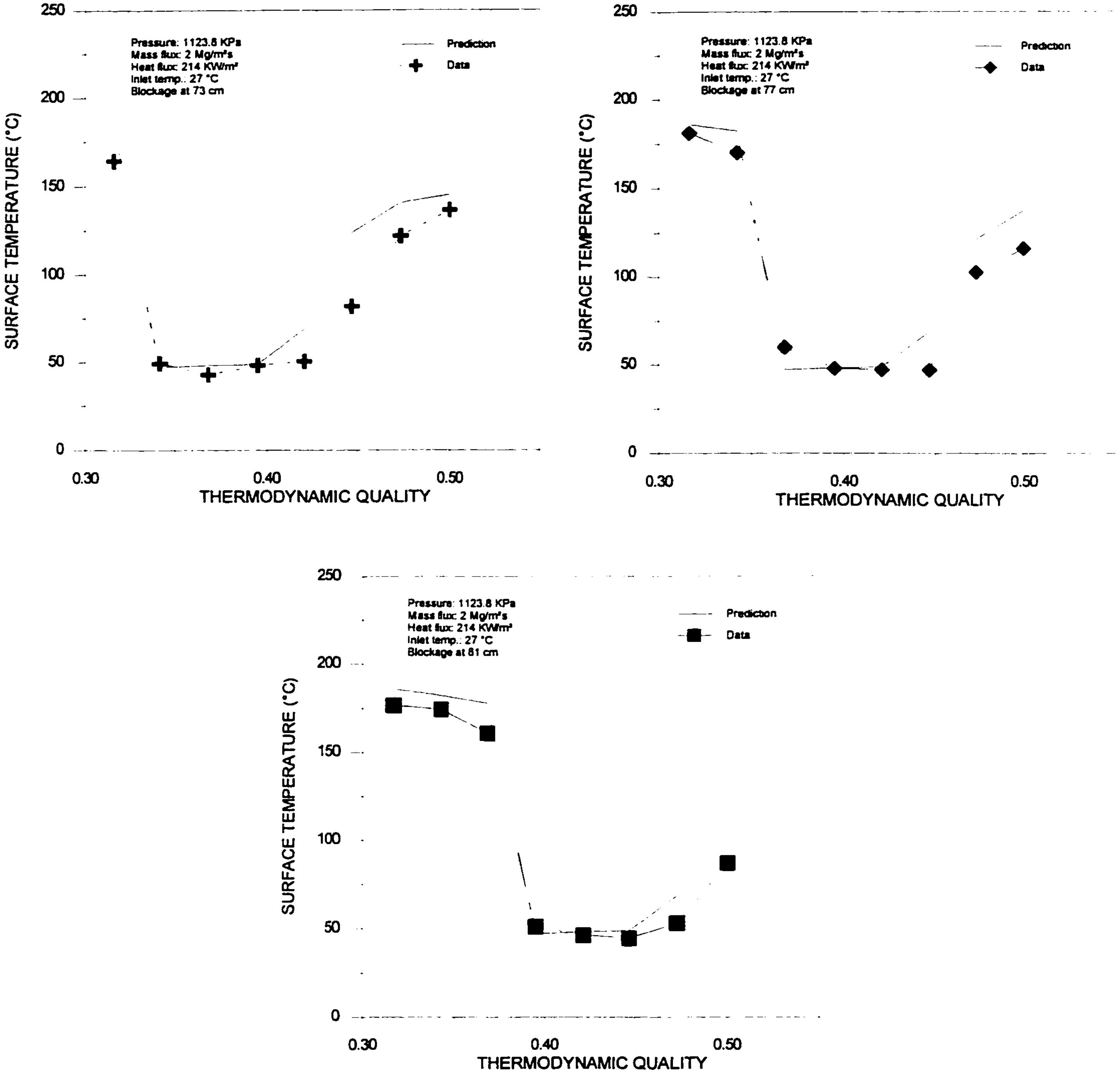

Figure 6.19. A comparison of surface temperature distributions between predictions and measurements along the channel with a hex-shaped blockage at various locations for a mass flux of 2 Mg/m^{2}s (including the CHF enhancement effect of the blockage and developing flow effect)

7. CONCLUSIONS AND RECOMMENDATIONS

- Correlations for the effects of channel shape and spacing devices on single-phase and post-dryout heat transfer have been developed. They are based on the modifications to the Nusselt number in tubes for the same flow conditions. The advantages of using these correlations are that:
    - they provide better prediction accuracy than existing correlations,
    - they provide correct asymptotic and parametric trends of Nusselt number with respect to flow conditions and geometries and hence can be extrapolated to conditions slightly beyond the database,
    - the correlation for shape effect is based on the geometric characteristics of the channel and hence can be applied to a wide variety of channel shape, and
    - the correlation for spacing-device effect is expressed in terms of the single-phase loss coefficient, which is a generalized parameter that can account for the effect of blockage shape and location on heat transfer.

- A thorough literature review of various geometric effects on single-phase and post-dryout heat transfer has been completed. It clearly shows a lack of information (both experimental and analytical) on these effects at post-dryout conditions. The available experimental data cover generally limited range of flow conditions and the combined database of various studies displays a large scatter among data at similar flow conditions. The use of the hydraulic-equivalent diameter approach to account for the channel-shape effect is appropriate for channels of shape close to a tube. It overestimates considerably the heat transfer rate for other channels, especially those with corners of a small apex angle. A strong enhancement of post-dryout heat transfer is observed at locations downstream of the spacing devices. At low quality conditions, in particular, the spacing devices can induce rewetting of the surface. This results in a significant increase in heat transfer rate (up to 10-30 times).

- An experiment has been completed to study the effect of blockage on post-dryout heat transfer using three different types of blockage in a tube with Freon-134a as coolant. The results clearly show the strong enhancement effect of blockage on heat transfer at locations downstream of the blockage, as observed from the literature review.

- A comparison between predictions of the correlation for spacing-device effect and experimental data shows an underprediction of heat transfer rate at locations downstream of the blockage. This is caused by the rewetting of the surface at the blockage, beyond which the developing-flow effect becomes dominant. The agreement between predictions and data is significantly improved after the developing-flow effect is included with a modification factor.

- Although the present correlations provide good agreement between predictions and present database, they have to be validated against other data that cover a wide range of flow conditions. This will ensure their applicability outside of the database and provide the prediction uncertainty at those flow conditions.

- The present study examines three types of geometric effect on post-dryout heat transfer: channel shapes, spacing devices and gap sizes. These effects are anticipated to have a strong impact on heat transfer. However, other effects (such as the axial and radial heat-flux distributions, neighboring heated and unheated surface, flow development, etc.) can also affect the heat transfer rate and hence should be examined.

8. REFERENCES

Abraham, S. C., 1966, "Preliminary Post-Dryout Data for Vertically Upward Steam-Water Annular Flow", AECL unpublished Report, APPE-43.

Altemani, C. A. C. and Sparrow, E. M., 1980, "Turbulent Heat Transfer and Fluid Flow in an Unsymmetrically Heated Triangular Duct", J. of Heat Transfer, Vol. 102, pp. 590-597.

Anderson, J. G. M., 1976, "Low Flow Film Boiling Heat Transfer on Vertical Surfaces - Part I: Theoretical Model", Presented at the 16th National Heat Transfer Conference, AIChE-52, St. Louis.

Becker, K. M., Ling, C. H., Hedberg, S. and Strand, G., 1983, "An Experimental Investigation of Post-Dryout Heat Transfer", Dept. of Nuclear Reactor Engineering, Royal Institute of Technology, Sweden, KTH-NEL-33.

Bennett, A. W., Hewitt, G. F., Kearsey, H. A. and Keeys, R. K. F., 1967, "Heat Transfer to Steam-Water Mixtures Flowing in Uniformly Heated Tubes in Which the Critical Heat Flux Has Been Exceeded", Chemical Engineering and Process Technology Division, Atomic Energy Research Establishment, Britain, AERE-R 5373.

Bromley, L. A., 1950, "Heat Transfer in Stable Film Boiling", Chem. Eng. Prog., Vol. 46, No. 5, pp. 211-227.

Burdunin, M. N., Zvonarev, Yu. A., Komendatov, A. S. and Kuzma-kichta, Yu. A., 1987, "Investigation of Post-Dryout Heat Transfer in Channel of Complex Shape" Heat Transfer Soviet Research, Vol. 19, No. 1, pp. 115-121, Jan. - Feb.

Chen, J. C., Morgan, C. D. and Sundaram, R. K., 1984, "A Correlation of Low Flow, Low Pressure, and Low-to-Moderate Quality Post-CHF Data", Proceedings of the Int. Workshop on Post-Dryout Heat Transfer, Salt Lake City, April 1-4.

Chen, W. J. and Lee, Y., 1979, "Effect of Partial Flow Blockage on Rewetting of Vertical and Horizontal Circular Ducts", Paper presented at the 18th National Heat Transfer Conference, San Diego, CA, August 5-8.

Cluss, E. M., 1978, "Post Critical Heat Flux Heat Transfer in a Vertical Tube Including Spacer Grid Effects", M. Sc. Thesis in Mechanical Engineering, M.I.T.

Collier, J. G., 1981, Post-Dryout Heat Transfer, in "Two-Phase Flow and Heat Transfer in the Power and Process Industries", pp. 282-324, Eds: Bergles, A. E., Collier, J. G., Delhaye, J. M., Hewitt, G. F. and Mayinger, F., Hemisphere Publishing Corporation.

Collier, J. G., 1982, "Heat Transfer in the Post Dryout Region and During Quenching and Reflooding", *HandBook of Multiphase Systems*, Editor: G. Hetsroni, McGraw-Hill Book Company.

Collier, J. G. and Thome, J. R., 1994, "Convective Boiling and Condensation", Oxford Science Publications

Dittus, F. W. and Boelter, L. M. K., 1930, "Heat Transfer in Automobile Radiators of the Tubular Type", Publications in Engineering, University of California, Berkeley, Vol. 2, pp. 443-461.

Doerffer, S., Groeneveld, D. C. and Schenk, J. R., 1996, "Experimental Study of the Effects of Flow Inserts on Heat Transfer and Critical Heat Flux", Paper presented at the 4th International Conference on Nuclear Engineering, New Orleans, March 10-14.

Dougall, R. S. and Rohsenow, W. M., 1963, "Film Boiling on the Inside of Vertical Tubes with Upward Flow of the Fluid at Low Qualities", MIT-TR-9079-26.

Eckert, E. R. G. and Irvine, Jr. T. F., 1960, "Pressure Drop and Heat Transfer in a Duct with Triangular Cross Section", J. of Heat Transfer, Vol. 82, pp. 125-138.

Era, A., Gaspari, G. P., Hassid, A., Milani, A. and Zavattarelli, R., 1967, "Heat Transfer Data in the Liquid Deficient Region for Steam-Water Mixtures at 70 kg/cm^2 Flowing in Tubular and Annular Conduits", CISE-R-184.

Fahmy, A. S. A., Mariy, A. H., Swidan, M. M. and Sylym, R. A., 1986, "Eccentric Annuli in Subcooled Boiling", Atomkernenergie Kerntechnik, Vol. 49, pp. 74-78.

Groeneveld, D. C., 1972, "The Thermal Behavious of a Heated Surface at and Beyond Dryout", AECL Report, AECL-4309.

Groeneveld, D. C., 1973, "Forced Convective Heat Transfer to Superheated Steam in Rod Bundles", AECL Report, AECL-4450, April.

Groeneveld, D. C., 1982, "Prediction Methods for Post-CHF Heat Transfer and Superheated Steam Cooling Suitable for Reactor Accident Analysis", Report TT/SETRE/82-4-E.

Groeneveld, D. C., 1984, "Inverted Annular and Low Quality Film Boiling: a State-of-the-Art Report", Proceedings of the Int. Workshop on Post-Dryout Heat Transfer, Salt Lake City, April 1-4.

Groeneveld, D. C., Cheng, S. C., Leung, L. K. H. and Nguyen, C.,1989, "Computation of Single- and Two-Phase Heat Transfer Rates Suitable for Water-Cooled Heat Transfer Equipment", Nuclear Engineering and Design, Vol. 114, pp. 61-77.

Groeneveld, D. C. and Delorme, G. G. J., 1976, "Prediction of Thermal Nonequilibrium in the Post-Dryout Regime", Nuclear Engineering and Design, Vol. 36, No. 1, pp. 17-26.

Groeneveld, D. C. and Yousef, W. W., 1980, “Spacing Devices for Nuclear Fuel Bundles: A Survey of Their Effect on CHF, Post-Dryout Heat Transfer and Pressure Drop”, Proc. of the ANS/ASME/NRC Int. Topical Meeting on Nuclear Reactor Thermal-Hydraulics, Vol. 2, pp. 1111-1125, Saratoga Springs, New York, Oct. 5-8.

Guellouz, M. S., 1989, “Heat Transfer in Rod Bundle Subchannels”, M. A. Sc. Thesis, University of Ottawa, Ottawa, Canada.

Guellouz, M. S. and Tavoularis, S., 1992, “Heat Transfer in Rod Bundles Subchannels with Varying Rod-Wall Proximity”, Nuclear Engineering and Design, Vol. 132, pp.351-366.

Guellouz, M. S. and Tavoularis, S., 1995, “Convective Heat Transfer Coefficient in Single-Phase Flow Through Rod Bundles”, Technical Report, UOME-BF-95-04.

Hammouda, N., 1996, “Subcooled Film Boiling in Non-Aqueous Fluids”, Ph.D. thesis, University of Ottawa, Ottawa, Ontario.

Hassan, Y. A., 1987, “Predictions of Vapour Superheat in a Rod Bundle Geometry with Modified RELAP5/MOD2”, Trans. Am. Nucl. Soc. V. 54, pp. 212-214.

Hassan, M. A. and Rehme, K., 1981, “Heat Transfer near Spacer Grids in Gas-Cooled Rod Bundles”, Nuclear Technology, Vol. 52, pp. 401-414.

Hewitt, G. F., 1982, “Burnout”, *HandBook of Multiphase Systems*, Editor: G. Hetsroni, McGraw-Hill Book Company.

Hsu, Y. Y., 1982, “Pre-Burnout Convective Boiling”, *HandBook of Multiphase Systems*, Editor: G. Hetsroni, McGraw-Hill Book Company.

Huang, X. C., Cheng, S. C., Groeneveld, D. C. and Rudzinski, K. F., 1996, "Analysis of the Conjugation Effect During Convective Flow Film Boiling Conditions in an Eccentric Annular Test Section", Nuclear Engineering and Design, Vol. 163, pp. 177-190.

Hudina, M. and Nothigen, H., 1972, "Experiment Study of Local Heat Transfer under and near Grid Spacers Developed for GCFR", Report TM-IN-526, Swiss Federal Institute for Reactor Research Wirenlingen, 2nd NEA-GCFR Specialist Meeting on Heat Transfer.

Hwang, T. H. and Jensen, M. K., 1991, "An Analysis of Convective Heat Transfer to Laminar Dispersed Flow in Eccentric Annuli", Int. Comm. Heat Mass Transfer, Vol. 18, pp. 27-38.

Idelchik, I. E., 1994, *Handbook of Hydraulic Resistance*, 3rd edition, Begell House.

Johannsen, K. and Mosaad, M., 1989, "Assessment of Heat Transfer Correlations for Subcooled and Low Quality Film Boiling of Water in a Vertical Tube", 2nd Int. Symposium of Multiphase Flow and Heat Transfer.

Johnston, B. S., Sharon, A., Kozawa, Y. and Bankoff, S. G., 1983, "Boiling Heat Transfer in a Narrow Eccentric Annulus, Part I: Dryout", Transactions of the ASME, Vol. 105, pp. 742-747.

Johnston, B. S., Sharon, A., Kozawa, Y. and Bankoff, S. G., 1983, "Boiling Heat Transfer in a Narrow Eccentric Annulus, Part II: Heat Transfer", Transactions of the ASME, Vol. 105, pp. 748-754.

Johnston, B. S. and Bankoff, S. G., 1986, "Boiling Heat Transfer in a Narrow Eccentric Annulus, Part III: A Model of Dry Patch Extent and Temperature Distribution", J. of Heat Transfer, Vol. 108, pp. 433-440.

Jones, Jr. O. C. and Zuber, N., 1977, "Post-CHF Heat Transfer: A Non-Equibrium Relaxation

Model", ASME 77-HT-79, Presented at the AIChE-ASME Heat Transfer Conference, Salt Lake City, Utah, August 15-17.

Kidd, G. J. and Hoffman, H. W., 1968, "The Temperature Structure and Heat Transfer Characteristics of an Electrically Heated Model of a Seven-Rod Cluster Fuel Element", ASME paper 68-WA/HT-33.

Kim, I. G. and Korol'Kov, B. P., 1991, "Enhancement of Steady-State Post-Dryout Heat Transfer in an Annulus with Spacers", Heat Transfer-Soviet Research, Vol. 23, No. 5, pp. 649-657.

Koizumi, Y., Kumamaru, H., Yonomoto, T. and Tasaka, K., 1984, "Investigation of Pre- and Post-Dryout Heat Transfer in Upward Steam-Water Two-Phase Flow at Low Flow Rate with Improved Surface Temperature Measurement", J. of Nuclear Science and Technology, Vol. 21, pp. 965-968.

Koizumi, Y., Kumamaru, H., Yonomoto, T. and Tasaka, K., 1987, "Post-Dryout Heat Transfer of High-Pressure Steam-Water Two-Phase Flow in Single Rod Channel and Multi Rod Bundle", Nuclear Engineering and Design, Vol. 99, pp. 157-165.

Krett, V. and Majer, J., 1971, "Temperature Field Measurement in the Region of Spacing Elements", Report ZJE-114, Skoda Works Nuclear Power Construction Dept., Information Center Plzen-Czechoslovakia.

Kumamaru, H., Koizumi, Y. and Tasaka, K., 1987, "Investigation of Pre- and Post-Dryout Heat Transfer of Steam-Water Two-Phase Flow in a Rod Bundle", Nuclear Engineering and Design, 102, pp. 71-84.

Laperrière, A., 1983, "An Analytical and Experimental Investigation of Forced Convective Film Boiling", M.A.Sc. Thesis, University of Ottawa, Dept. of Mechanical Engineering.

Leung, L. K. H., Hammouda, N. and Groeneveld, D. C., 1997, "A Look-up Table for Film-Boiling Heat Transfer Coefficients in Tubes with Vertical Upward Flow", Paper submitted for presentation at the 8th International Topical Meeting on Nuclear Reactor Thermal-Hydraulics (NURETH-8), Kyoto, Japan, Sept. 30-Oct. 4.

Leung, L. K. H. and Hotte, G., 1997, "A Generalized Prediction Method for Single-Phase Pressure Drop in a String of Aligned CANDU-Type Bundles", Paper submitted for presentation at the 20th CNS Simulation Symposium, Sept. 7-9, Niagara-on-the Lake, Ontario.

Mattson, R. I., Condie, K. G., Bengston, S. J. and Obenchain, C. E., 1974, "Regression Analysis of Post-CHF Flow Boiling Data", Proc. 5th Int. Heat Transfer Conf., Tokyo, 3, 8, pp. 115-119.

Möller, R. and Tschöke, H., 1980, "Steady-State, Local Temperature Fields with Turbulent Liquid Sodium Flow in Nominal and Disturbed Bundle Geometries with Spacer Grids", Nuclear Engineering and Design, Vol. 62, pp. 69-80.

Morris, D. G., Mullins, C. B. and Yoder, G. L., 1982. "Rod-Bundle Transient Film Boiling of High Pressure Water in the Liquid Deficient Regime", Conference: AIAA/ASME Joint Conference on Fluids, Plasma, Thermophysics and Heat Transfer, St. Louis, Jun. 7-11.

Morris, D. G., Mullins, C. B. and Yoder, G. L., 1985, "An Experimental Study of Rod Bundle Dispersed-Flow Film Boiling with High-Pressured Water", Nuclear Technology, V. 69 (1), pp. 82-93.

Novotny, J. L., McComas, S. T., Sparrow, E. M. and Eckert, E. R. G., 1964, "Heat Transfer for Turbulent Flow in Rectangular Ducts with Two Heated and Two Unheated Walls", AIChE Journal, Vol. 10, No. 4, pp. 466-470.

Ouma, B. H. and Tavoularis, S., 1991, "Flow Measurements in Rod Bundle Subchannels with

Varying Rod-Wall Proximity", Nucl. Engineering Design, Vol. 131, pp. 193-208.

Rehme, K., 1977, "Pressure Drop of Spacer Grids in Smooth and Roughened Rod Bundles", Nuclear Technology, Vol. 31, pp. 314-317.

Saha, P., 1980, "A Non-Equibrium Heat Transfer Model for Dispersed Droplet Post-Dryout Regime", Int. J. Heat and Mass Transfer, Vol. 23, pp. 483-492.

Salcudean, M. E. and Leung, L. K. H., 1988, "Pressure Drop due to Flow Obstruction", Nuclear Engineering and Design, Vol. 105, pp. 349-362.

Sergeev, V. V., Gonin, A. I. and Remizov, O. V. 1990, "Supercritical Heat Exchange in Channels with Spacer Elements", Atomnaya Energiya, Vol. 68, No. 6, pp. 445-447, June.

Shiina, K., Nakamura, S. and Sagawa, W., 1991, "Enhancement of Forced Convective Heat Transfer in a Rectangular Channel Using Plate-type Obstacles, Part 2 - Heat Transfer and Pressure Drop Characteristics Using Spacer Configuration", ASME/JSME Thermal Engineering Proceedings, Vol. 4, pp. 455-462.

Sparrow, E. M., Lloyd, J. R. and Hixon, C. W., 1966, "Experiments on Turbulent Heat Transfer in an Asymmetrically Heated Rectangular Duct", J. of Heat Transfer, Vol. 88, pp. 170-174.

Stewart, J. C., 1981, "Low Quality Film Boiling at Intermediate and Elevated Pressures", M.A.Sc. Thesis, University of Ottawa.

Sugimoto, Jun and Murao, Yoshio, 1984, "Effect of Grid Spacers on Reflood Heat Transfer in PWR-LOCA", J. Nucl. Sci. Tech. V. 21 (2), pp. 103-114.

Tong, L. S. and Weisman, J., 1996, *Thermal Analysis of Pressurized Water Reactors*, American

Nuclear Society.

Unal, C., Tuzla, K., Badr, O., Neti, S. and Chen, J. C., 1988, "Parametric Trends for Post-CHF Heat Transfer in Rod Bundles", J. Heat Transfer, Vol. 110, pp. 721-727.

Usui, H, Sano, Y. and Fukuma, H., 1982, "Turbulence Measurements and Mass Transfer in Fully Developed Flow in a Triangular Duct with a Narrow Apex Angle", Int. J. Heat Mass Transfer, Vol. 25, pp. 615-624.

Varone, A. F. and Rohsenow, W. M., 1984, "Post Dryout Heat Transfer Prediction", Joint Japan-USA Two-Phase Flow Conference, Lake Placid, NY, USA.

Vlcek, J. and Weber, P., 1970, "The Experimental Investigation of a Local (spot) Heat Transfer Coefficient in the Fuel Spacer Area", Australian Atomic Energy Commission Research Establishment, LIB/TRANS 250.

Yao, S. C., Hochreiter, L. E. and Leech, W. J., 1982, "Heat-Transfer Augmentation in Rod Bundles Near Grid Spacers", Journal of Heat Transfer, Vol. 104, pp. 76-81.

Yoder, G. L., Morris, D. G., Mullins, C. B. and Ott, L. J., 1981, "The Effect of Spacer Grids on Post-CHF Rod Bundle Heat Transfer", Trans. American Nuclear Society, V. 39, pp. 1045-1046.

Yoder, G. L., Morris, D. G., Mullins, C. B., Ott, L. J. and Reed, D. A., 1982a, "Dispersed Flow Film Boiling in Rod-Bundle Geometry -- Steady State Heat-Transfer Data and Correlation Comparisons", NUREG/CR-2435, ORNL-5822.

Yoder, G. L., Morris, D. G., Mullins, C. B., Ott, L. J. and Reed, D. A., 1982b, "Steady-State Film Boiling Data in Rod-Bundle Geometry and Non-equilibrium Correlation Assessment", Conference: AIAA/ASME Joint Conference on Fluids, Plasma, Thermophysics and Heat Transfer, St. Louis, Jun.

7-11.

Yoder, G. L., Morris, D. G., Mullins, C. B. and Ott, L. J., 1983, "Dispersed Flow Film Boiling Heat Transfer Data near Spacer Grids in a Rod Bundle", Nucl. Tech. V. 60(2), pp. 304-313.

Yoder, G. L. and Rohsenow, W. M., 1980, "Dispersed Flow Film Boiling", MIT Heat Transfer Laboratory Report, No. 85694-103, March.

9. APPENDIX

Table 9.1. Experiment data of Sergeev et al. (1990)

Axial length	$P=13.7$ MPa, $G=500$ kg/m^{2}s, $q=310$ KW/m^2, $D_{hy}=10$ cm, wall temperature		
	$\epsilon=0$	$\epsilon=0.154$	$\epsilon=0.326$
Z (m)	T_w (°C)	T_w (°C)	T_w (°C)
3.2	500	475	340
3.3	505	495	340
3.35	510	505	340
3.45	512	510	400
3.48	515	465	430
3.5	520	480	400
3.55	525	500	345
3.6	530	510	347
3.65	535	515	375
3.75	540	520	440
3.85	545	530	460
3.9	550	540	465
4.0	550	485	415
4.05	555	495	361
4.1	560	505	430
4.2	565	510	450
4.3	555	515	465
4.4	570	520	475

Table 9.2 Data of Rehme (1977) with blockage ratio of 0.348

Z/D_{hy}	0	1	2	3	4	5
Nu*	1.75	1.67	1.58	1.50	1.44	1.37

Table 9.3 Data of Vlcek and Weber (1970) with blockage ratio of 0.289

Z/D_{hy}	0.3	3	4	5	7
Nu*	1.55	1.45	1.33	1.31	1.28

Table 9.4 Data of Kidd and Hoffman (1968) with blockage ratio of 0.245

Z/D_{hy}	0.3	2.8	3.5	4.5	5.5	6.5	7.5	8.8	10	12	15
Nu*	1.48	1.35	1.30	1.25	1.23	1.20	1.17	1.13	1.10	1.08	1.05

Table 9.5 Data of Krett and Majer (1971) with blockage ratio of 0.303

Z/D_{hy}	1	2	3	4	5	6	7	10
Nu*	1.45	1.40	1.30	1.25	1.18	1.15	1.10	1.05

Table 9.6 Data of Vlcek and and Weber (1970) with blockage ratio of 0.237

Z/D_{hy}	1	2	4	6	8	10
Nu*	1.18	1.16	1.12	1.10	1.07	1.03

Table 9.7 Data of Hudina and Nothigen (1972) with blockage ratio of 0.156

Z/D_{hy}	0	1	2	3	5	7.5
Nu*	1.08	1.07	1.06	1.05	1.04	1.03

Table 9.8. Experiment data of ring-shaped obstacle with mass flux of 2000 kg/m^{2}s

Spacer location (cm)	Pressure (KPa)	Inlet temp. (°C)	Mass flux (kg/m^{2}s)	Heat flux (KW/m^2)	Thermocouple locations (cm)							
					100	96	92	88	84	80	76	72
					TC-1 (°C)	TC-2 (°C)	TC-3 (°C)	TC-4 (°C)	TC-5 (°C)	TC-6 (°C)	TC-7 (°C)	TC-8 (°C)
25	1123.8	27	2000	217	205.8	153.3	143.7	164.8	161.8	157.5	171.6	152.8
60	1123.8	27	2000	217	201.5	152.7	143.0	159.7	153.2	144.8	152.9	58.7
62	1123.8	27	2000	217	191.3	146.6	134.2	149.4	139.8	131.6	65.6	48.8
66	1123.8	27	2000	217	184.1	140.2	127.4	138.2	127.8	65.5	54.9	48.4
73	1123.8	27	2000	217	202.9	141.7	134.6	98.1	47.8	46.3	58.7	145.4
77	1123.8	27	2000	217	198.5	135.7	110.5	46.0	47.0	49.7	161.8	141.9
81	1123.8	27	2000	217	180.6	109.5	46.5	45.2	51.5	151.6	168.0	150.2
85	1123.8	27	2000	217	176.7	64.7	45.3	48.6	140.3	151.0	164.6	144.9
89	1123.8	27	2000	217	56.1	44.9	50.4	160.3	154.3	154.9	166.3	144.9

Table 9.9. Experiment data of ring-shaped obstacle with mass flux of 3000 kg/m²s

Spacer location (cm)	Pressure (KPa)	Inlet temp. (°C)	Mass flux (kg/m²s)	Heat flux (KW/m²)	Thermocouple locations (cm)							
					100	96	92	88	84	80	76	72
					TC-1 (°C)	TC-2 (°C)	TC-3 (°C)	TC-4 (°C)	TC-5 (°C)	TC-6 (°C)	TC-7 (°C)	TC-8 (°C)
25	1123.8	27	3000	217	183.4	167.7	140.4	135.4	141.3	130.2	114.0	108.8
60	1123.8	27	3000	217	174.5	151.8	137.3	131.8	136.6	124.9	47.8	47.4
64	1123.8	27	3000	217	168.0	150.8	137.4	132.0	125.5	45.6	47.1	44.5
68	1123.8	27	3000	217	165.0	161.1	138.6	131.8	48.0	46.2	47.8	45.4
81	1123.8	27	3000	217	128.0	85.4	44.0	45.6	48.9	116.1	106.6	100.8
89	1123.8	27	3000	217	90.8	42.6	45.5	133.1	132.8	122.4	106.8	103.4

Table 9.10. Experiment data of cube-shaped obstacle with mass flux of 2000 kg/m^{2}s

Spacer location (cm)	Pressure (KPa)	Inlet temp. (°C)	Mass flux (kg/m^{2}s)	Heat flux (KW/m^2)	Thermocouple locations (cm)							
					100	96	92	88	84	80	76	72
					TC-1 (°C)	TC-2 (°C)	TC-3 (°C)	TC-4 (°C)	TC-5 (°C)	TC-6 (°C)	TC-7 (°C)	TC-8 (°C)
25	1123.8	27	2000	203	183.2	162.1	154.0	165.5	173.8	138.2	49.4	45.0
60	1123.8	27	2000	203	171.5	115.0	44.7	45.6	46.4	42.0	42.3	43.4
69	1123.8	27	2000	203	160.6	60.3	43.0	45.4	46.3	42.3	42.6	42.7
77	1123.8	27	2000	203	58.6	44.9	42.8	45.2	46.3	43.5	43.2	43.1
81	1123.8	27	2000	203	58.8	46.4	43.6	45.8	47.2	134.8	45.5	42.5
85	1123.8	27	2000	203	58.9	46.1	44.1	53.0	170.3	131.6	46.8	42.3

Table 9.11. Experiment data of cube-shaped obstacle with mass flux of 3000 kg/m^2s

Spacer location (cm)	Pressure (KPa)	Inlet temp. (°C)	Mass flux (kg/m^2s)	Heat flux (KW/m^2)	Thermocouple locations (cm)							
					100	96	92	88	84	80	76	72
					TC-1 (°C)	TC-2 (°C)	TC-3 (°C)	TC-4 (°C)	TC-5 (°C)	TC-6 (°C)	TC-7 (°C)	TC-8 (°C)
25	1123.8	27	3000	222	186.1	181.3	174.3	194.3	200.8	57.5	48.3	45.8
52	1123.8	27	3000	222	179.7	167.3	80.2	49.4	49.4	44.4	45.0	44.8
56	1123.8	27	3000	222	168.6	52.0	38.7	47.7	47.8	43.8	44.1	44.4
60	1123.8	27	3000	222	104.6	49.1	41.9	52.1	47.5	43.6	44.2	44.3
77	1123.8	27	3000	222	38.3	47.9	44.8	56.7	56.7	43.0	45.7	45.7
81	1123.8	27	3000	222	37.2	47.3	44.6	56.9	57.1	47.5	47.2	45.0
85	1123.8	27	3000	222	40.6	46.1	44.6	58.2	192.3	46.2	45.3	45.3

Table 9.12. Experiment data of hex-shaped obstacle with mass flux of 2000 kg/m^{2}s

Spacer location (cm)	Pressure (KPa)	Inlet temp. (°C)	Mass flux (kg/m^{2}s)	Heat flux (KW/m^2)	Thermocouple locations (cm)							
					100	96	92	88	84	80	76	72
					TC-1 (°C)	TC-2 (°C)	TC-3 (°C)	TC-4 (°C)	TC-5 (°C)	TC-6 (°C)	TC-7 (°C)	TC-8 (°C)
25	1123.8	27	2000	214	194.2	152.7	173.4	199.1	205.0	176.3	186.6	175.6
60	1123.8	27	2000	214	182.2	134.6	147.2	156.5	123.5	43.6	44.5	43.9
64	1123.8	27	2000	214	180.3	131.5	141.0	141.1	85.4	43.4	44.5	45.5
69	1123.8	27	2000	214	179.1	128.0	135.5	123.5	77.0	42.7	44.2	49.5
73	1123.8	27	2000	214	175.5	115.2	91.3	50.4	48.2	42.8	49.3	153.5
77	1123.8	27	2000	214	155.0	95.8	46.9	47.0	47.8	59.8	173.7	170.1
81	1123.8	27	2000	214	125.8	52.9	44.5	46.2	51.1	158.8	178.1	165.8

Table 9.13 Experiment data of Altemani and Sparrow (1980)

Re	4000	4100	6800	9700	14400	20000	28750	30000	41000	60000
Nu	12.9	13.2	18.6	25	33	43	54	57	72	96

Table 9.14 Experiment data of Eckert and Irvine (1960)

Re	4350	4600	6000	6250	6750	7000	9300	97500	13330	15660	16330	20500	22100	23680
Nu	8.2	8.6	10	10.5	11.4	11.2	13.9	14.4	16.6	18	19	22.8	23.9	24.7

Table 9.15 Experiment data of Usui et al. (1982)

Re	12000	13000	14000	15000	16500	17500	19000	21500	25000	26500	28000	30000	33000
Nu	340	360	380	400	450	500	550	600	650	675	700	720	850

Table 9.16 Experiment data of Sparrow et al. (1966)

Re	19000	32000	33000	46000	55000	58500	70000	90000	97000	110000	120000	150000
Nu	45	67	70	82	95	100	120	140	160	170	180	190

Table 9.17 Experiment data of Novotny et al. (1964)

Aspect ratio=0.1		Aspect ratio=0.2		Aspect ratio=1	
Re	Nu	Re	Nu	Re	Nu
1.35×10^4	42	1.1×10^4	34	1.2×10^4	40
2.2×10^4	60	1.3×10^4	38	1.45×10^4	43
2.3×10^4	64	1.7×10^4	48	1.75×10^4	50
3.0×10^4	72	1.95×10^4	51	2.1×10^4	58
3.2×10^4	81	2.1×10^4	51.5	2.5×10^4	66
3.5×10^4	83	2.3×10^4	60	2.7×10^4	70
5.0×10^4	120	2.4×10^4	62	3.25×10^4	82
6.3×10^4	130	2.9×10^4	68	4.0×10^4	85
7.0×10^4	135	3.6×10^4	80	4.5×10^4	100
		3.8×10^4	85	4.55×10^4	105
		5.5×10^4	120	5.8×10^4	125
		7.0×10^4	140	6.1×10^4	130
		7.3×10^4	145	7.2×10^4	135
		9.0×10^4	170	9.0×10^4	165
		10.5×10^4	200	10×10^4	175
		13.5×10^4	210	14×10^4	220

IMAGE EVALUATION
TEST TARGET (QA-3)

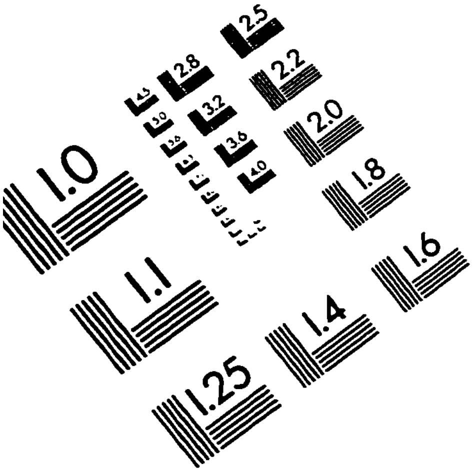

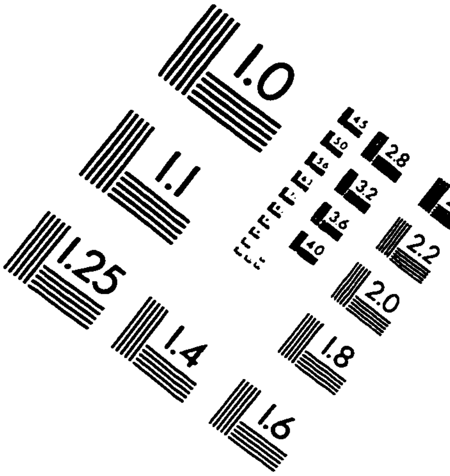

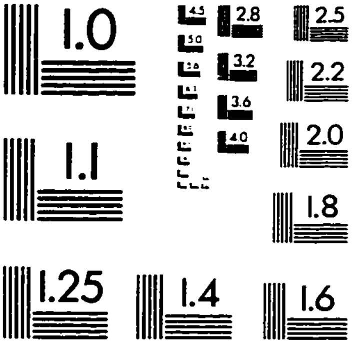

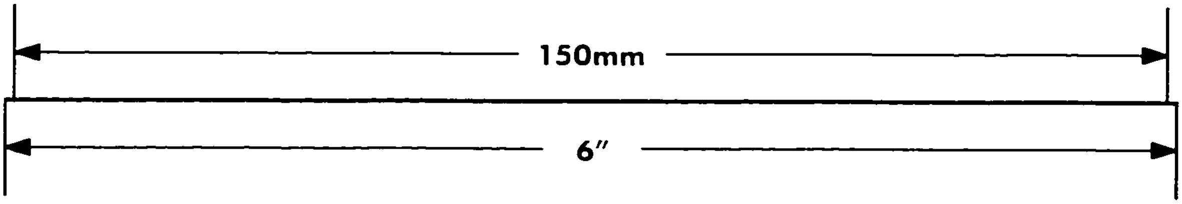

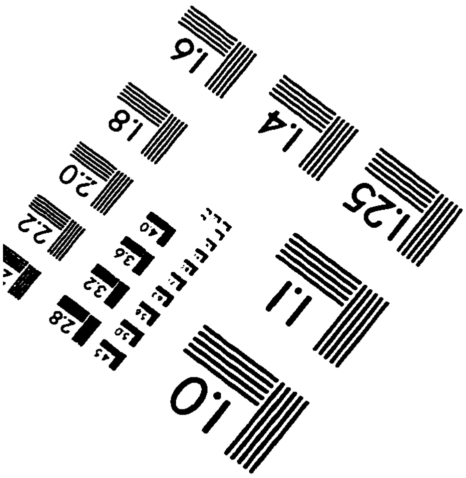

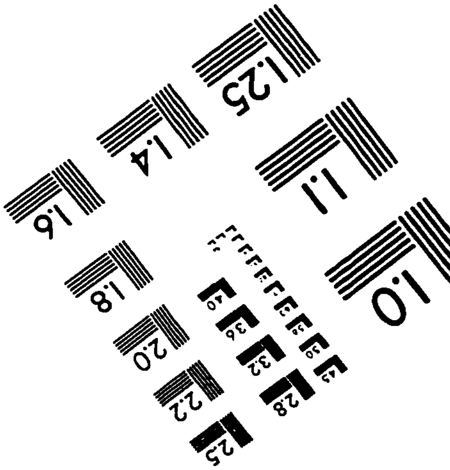

APPLIED IMAGE . Inc
1653 East Main Street
Rochester, NY 14609 USA
Phone: 716/482-0300
Fax: 716/288-5989